

**MECHANICAL CONSTRAINT AND CELL SHAPE
INTERACTION MODELING OF BACTERIAL GROWTH
IN MICROFLUIDIC DEVICES**

A Dissertation Presented to
the Faculty of the Department of Mathematics
University of Houston

In Partial Fulfillment
of the Requirements for the Degree
Doctor of Philosophy

By
James J. Winkle
August 2018

MECHANICAL CONSTRAINT AND CELL SHAPE
INTERACTION MODELING OF BACTERIAL GROWTH
IN MICROFLUIDIC DEVICES

James J. Winkle

APPROVED:

Prof. Krešmir Josić, Advisor
Dept. of Mathematics

Prof. William Ott
Dept. of Mathematics

Prof. Ilya Timofeyev
Dept. of Mathematics

Prof. Matthew R. Bennett
Rice University

Dean, College of Natural Sciences and Mathematics

Acknowledgements

I would like to kindly thank my advisor, Dr. Krešmir Josić, who first connected me with the field of mathematical biology and invited me into his research group. I sincerely thank Dr. William Ott for the many hours spent discussing the present material and for providing a sounding-board in my exploration of these and other directions therewith. I would like to thank Dr. Matthew R. Bennett at Rice University for serving on my committee and for providing such a rich collaboration with an experimental group at The Biodesign Lab. I would also like to thank Dr. Ilya Timofeyev for serving on my committee and also for serving as the Graduate advisor in the Department of Mathematics. I would like to thank Dr. Daniel Onofrei, who first encouraged me to consider graduate study in Applied Mathematics at The University of Houston.

I have had the pleasure of working with Dr. Ronald W. Hoppe with a Research Assistantship during my stay at The University of Houston and I would like to sincerely thank him for his time and collaboration during this period.

I would like to also thank the members of the Josic and Bennett labs for their collaboration and discussions. In particular I would like to thank Razan Alnahhas and David Zong from the Bennett lab for providing the experimental data that is used in this dissertation. From the Josic lab I would like to also thank Dr. Bhargav Karamched for the many discussions. I look forward to future collaborations with everyone I have worked with.

I would also like to thank Emily Berman for her support during the long hours of preparation for this dissertation.

This dissertation is dedicated to my longtime friend in
music, math and life: William Brett Youens.

**MECHANICAL CONSTRAINT AND CELL SHAPE
INTERACTION MODELING OF BACTERIAL GROWTH
IN MICROFLUIDIC DEVICES**

An Abstract of a Dissertation
Presented to
the Faculty of the Department of Mathematics
University of Houston

In Partial Fulfillment
of the Requirements for the Degree
Doctor of Philosophy

By
James J. Winkle
August 2018

Abstract

Modeling mechanical interactions of bacteria is integral to capturing their dynamics in close-knit populations, because mechanical signals can be a primary means of inter-cellular communication in these environments. Agent-based models are used to study such mechanical interactions; however, conventional frameworks usually neglect the role of mechanical constraint and its coupling to other cellular dynamics. Continuum models often neglect sufficient description of cellular ordering dynamics, which depend on the complex interactions of cell shape anisotropy and shear flow that can originate from cellular growth expansion.

In this dissertation, we present models for the study of mechanical interactions of bacterial consortia in microfluidic traps. We include in our study an agent-based model that directly incorporates mechanical growth inhibition into the dynamics of the model and we show how emergent dynamics can be shaped by differences in model parameters. We also study a continuum model that considers growth through the evolution of the cell pressure and the resulting spatially-mapped velocity gradients. Our continuum model borrows ordering dynamics equations from liquid crystal theory in a two-dimensional setting and we use our model to predict how both persistent order and disorder can exist among close-packed bacterial cells in a microfluidic trap .

Further, we explore the impact of dynamic aspect ratio control on bacterial consortia and show how it can be used as a population control modality. We conclude with a conjecture and model for the modulation of a protein production rate by mechanical constraint that helps explain anomalous experiments.

Contents

1	Introduction	1
1.1	Bacterial microorganisms and their role in synthetic biology	1
1.2	Consortia in synthetic biology	4
1.3	Microfluidic devices and experimental imaging of bacterial consortia .	5
1.4	Mathematical modeling in synthetic biology	6
1.4.1	Computational resources	6
1.4.2	Modeling complexity	8
1.4.3	Modeling approaches	8
1.5	Outline of the dissertation	9
2	Agent-Based Modeling of Mechanical Interactions in Bacterial Populations	12
2.1	Introduction	12
2.2	Modeling framework	16
2.2.1	Cell construction	18
2.2.2	Growth model	19
2.2.3	Equations of motion for an isolated cell	21
2.3	Behavior of cells in a mother-machine	23
2.4	Two-dimensional microfluidic trap geometries: results and predictions	25
2.4.1	Two-strain consortium growing in an open trap	26

2.4.2	Varying the rest length extension program	27
2.5	Discussion	33
3	Competition of Bacterial Strains through Changes of Cell Aspect Ratio	36
3.1	Introduction	37
3.2	Simulation results	39
3.2.1	Simulation model	39
3.2.2	Aspect ratio change leads to lateral invasion	41
3.2.3	Discussion	42
3.2.4	Strain ratio dynamics vs. aspect ratio change	43
3.2.5	Aspect ratio control via cell-cell signaling	47
3.3	Discussion	49
4	Continuum Modeling of Bacterial Growth	51
4.1	Introduction	51
4.2	Mathematical model	54
4.2.1	Cell fluid model of Volfson et al.	54
4.2.2	Re-derivation of the cell fluid model	58
4.2.3	Liquid crystals and Q-tensor structure	64
4.2.4	Discussion	77
4.3	Results	80
4.3.1	Cell pressure and velocity fields	80
4.3.2	Q-tensor scalar order parameter and director	82
4.4	Discussion	87
5	A Model for Protein Expression Modulated by Mechanical Constraint	91
5.1	Motivation and experimental evidence	91

5.2	Experimental data	95
5.2.1	Overview	95
5.2.2	Example 2 μM calibration experiment	95
5.2.3	A second experiment	101
5.2.4	Spatial heterogeneity of the FP expression	102
5.3	Mathematical model	108
5.3.1	Protein expression	108
5.3.2	Pressure-modulated production rate	109
5.3.3	Spatial transport	111
5.3.4	Degradation added to model	113
5.4	Results	114
5.5	Discussion and conclusions	117
5.5.1	Bacterial stress response	117
5.5.2	Synthetic biology context	119
5.5.3	Conclusions	119
6	Conclusions	121
A	Agent based model simulation framework	125
A.1	Non-inertial dynamics assumption	125
A.2	Time discretization requirements	127
A.3	Coupled mass-spring matrix equations	128
A.3.1	3-cell mother-machine	128
A.3.2	No spring damping	131
A.3.3	Large spring damping	132
A.4	Simulation details	134
A.4.1	Chipmunk 2D simulation environment	134

A.4.2	Cell division algorithm	136
A.5	Ratchet algorithm for cell back-filling	137
A.6	Table of parameter values	139
B	Diffusion Signalling Model	141
B.1	Mathematical model	141
B.1.1	HSL ODE	141
B.1.2	Time-stepping algorithm	143
B.1.3	Calculation for an explicit scheme	144
B.2	Numerical simulations	145
	Bibliography	146

Chapter 1

Introduction

This dissertation is a study of mathematical modeling of bacteria in the context of synthetic biology and we begin with a brief background to set the context of the work.

1.1 Bacterial microorganisms and their role in synthetic biology

The study of bacteria encompasses a large array of scientific fields. For example, we benefit in public health from myriad advances in this sphere: from the study of the generation, evolution, and transfer of microbial pathogens [89], to the production of food supplements [103], proteins [163], and antibiotics in medical applications [21, 127]. Industrial applications of bacteria give economic advantages to production of

food and pharmaceuticals [9], chemical biosynthesis [85], bioremediation [26, 88, 31] and pest elimination [134], and can even be harnessed for the microbial production of high-energy fuels [149, 138].

Synthetic biology is a rapidly expanding, interdisciplinary field that harnesses engineering principles, mathematical modeling, and standardized parts and tools to design biological systems with specific functionality [7, 15]. Microbes are prominent in this effort due to their relative simplicity [101], wide application, and general ease of use [22], and due to their abundance in, on, and around our corpus [53, 80, 158, 173]. Further, many microorganisms are well-characterized with advanced techniques available for their genetic manipulation [92].

Advances in synthetic biology have widened the scope and refined the processes of all of the above industrial microbial applications [9, 25, 115, 120, 129, 144, 150, 174], and there is wide-ranging research in many other areas, from drug discovery [169], toxic chemical detection [87], antimalarial therapies [119, 106], environmental management [96] and synthetic ecology [83], gastrointestinal health [108], tissue self-organization [84], designer probiotics [35] and biomedical devices [68], to detection of explosives [86] and potential use for resource utilization on space missions [107].

Besides advancing applications in the industrial sphere, synthetic biology also comprises many areas of fundamental research that produce biological insights into form and function of biological systems at all levels [155]. From the seminal publications of a synthetic oscillator [46] and switch [58], synthetic biology advances knowledge in the areas of (among others): synthetic orthogonal transcription factors [22, 95], gene regulatory parts [100], timing of transcriptional regulation [33], and

intercellular communication systems [13].

Research with applications for non-regulatory (structural) genetic control spans: digital logic gates [112] and switches [24], genetic oscillators [32, 148], genomically encoded memory [51, 124, 162, 154] and population-based computing [11], genetic circuit [71] and bio-production breadboard models [176], repurposing of the translation system for novel functions [41], metabolic engineering [36, 76, 121] and division of labor [160], molecular, intercellular communication systems [13, 50, 53] and chemical control of organisms [55], and rational engineering of synthetic microbial consortia [22, 59, 73, 147].

The accelerating expanse of synthetic biology techniques has been met with attempts to standardize certain tools across systems and exchange of information between institutions [128, 18]. We further comment that this vast array of biological research does not come without certain risks, potentially to humans or to the environment, and addressing pathogenic, social, ethical and legal issues is also of increasing concern [65, 125, 139, 150, 156, 37, 90].

The study of bacteria and their use in synthetic biology furthers the promise for rational design of organisms for all of public health, medicine, industrial and pure scientific applications. The field of synthetic biology is wide-ranging, ongoing, and perhaps one of the most exciting cross-disciplinary fields in current existence. This dissertation attempts to further this study with mathematical models that aid in predicting and explaining experiments.

1.2 Consortia in synthetic biology

The promise of synthetic biology relies not only on the rational design of *single* cell dynamics, structure and function, but also on the design of assemblies of *interacting* cells and organisms. Cooperating cells can specialize and assume different responsibilities within a collective [172] and this allows such bacterial consortia to outperform monocultures [105, 130, 114, 54]. Both in terms of efficiency and range of functionality, cell collectives can perform computations and make decisions that are far more sophisticated than those of a single bacterium [126]. Advances in synthetic biology allow us to design multiple, interacting bacterial strains, and observe them over many generations [32]. The dynamics of such microbial consortia are strongly affected by spatial and temporal changes in the densities of the interacting strains, and their resulting spatial distribution determines the concentrations of the corresponding intercellular signals in their environment, which, in turn, determines the coupling among strains. To effectively design and control such consortia, it is necessary to understand the mechanisms that govern the spatiotemporal dynamics of bacterial collectives.

This dissertation presents different strategies to achieve this goal, with a particular emphasis on the role of mechanical interactions of bacteria in a collective. Mathematical and computer models help in this effort by allowing the researcher to explore potentially large parameter spaces using reduced-order models or large-scale parallelism to sweep the parameter space, which can be costly and time-prohibitive in an experimental setting. Agent-based models are particularly well suited to study

consortial dynamics, as they allow the programming of independent rules to interacting strains, whose spatiotemporal dynamics are neither easily predicted nor analytically tractable. Chapter 2 will explore an agent-based model that focuses on emergent behaviors of bacterial collectives and allows the exploration of parameter spaces that include *mechanical constraint* with respect to cell growth and protein expression, for example. We argue that mechanical effects, alongside cell signaling and genetic transformations, are important to the study of bacterial collectives, and this dissertation will attempt to further this study by including mechanical interactions directly into the modeling framework.

1.3 Microfluidic devices and experimental imaging of bacterial consortia

Observing the growth of bacteria in a scientific context presents several challenges. Bacterial growth in natural environments is dominated by the formation of biofilms [114, 54, 105, 130], whereby bacterial cells can communicate as an emergent unit under conditions of limited resources to gain advantages of social cooperation, metabolic resource acquisition and resistance to antimicrobial exposure [54]. In a laboratory environment, cells are typically observed via flow cytometry [141] and in microfluidic traps [20, 91, 123, 147]. In this dissertation, we consider only models of bacterial growth in microfluidic devices. However, many of the models' components are general enough to be applicable in other environments. In the next section, we will review different mathematical modeling approaches to bacterial growth in the contexts of

biofilms and microfluidics primarily.

1.4 Mathematical modeling in synthetic biology

1.4.1 Computational resources

The rapid expansion of genetic techniques for transformation and control of microorganisms in the context of systems and synthetic biology has been accompanied by continued growth in software and computing resources [27], including those available both on a researcher’s laptop computer, and on large-scale computing clusters at the institutional, governmental and commercial levels. A 2010 government report (“The opportunities and challenges of exascale computing”) sets the motivation for computing in the sciences [12]:

The great frontier of computational physics and engineering is in the challenge posed by high-fidelity simulations of real-world systems, that is, in truly transforming computational science into a fully predictive science.

This report cites, alongside climate and weather, aerospace, materials science, nuclear engineering and national security, *biological and medical systems* as a field where such transformation has taken place. The report gets to the heart of the matter for mathematical modeling in biology and a call for the increase in computation scale [12]:

In biology, the challenges of modeling at multiple scales—from atomic, through

genomic and cellular, to ecosystems—are already pushing beyond the petascale class of computing systems coming online. For example, a computational approach to understanding cellular systems and their related genes and biochemical pathways, referred to as systems biology, aims to develop validated capabilities for simulating cells as spatially extended mechanical and chemical systems in a way that accurately represents processes such as cell growth, metabolism, locomotion, and sensing. Modeling and simulation provide only a local view of each process, without interactions between modalities and scales. Exascale computing and new simulation management tools are needed to represent the various macroscopic subsystems and to enable a multiscale approach to biological modeling.

This dissertation deals directly with many of the components mentioned in the above quotation. For example, modeling of consortia leads to *spatially separated* strains and interactions (signaling distance is limited), local spatial scales are important in agent-based models (where consortial scales are emergent), and protein production (genetic expression) is typically modeled by stochastic simulation of reaction kinetics, but may also include metabolic cost, cell transport, and sensory input.

An increase of availability, size, and complexity of computational resources translates to both increased speed and increased parallelism in simulations of mathematical models, both of which can combine to increase model precision and realism. However, judicious choices of model parameters and understanding the extent of a model’s detail will always be part of any modeling effort.

1.4.2 Modeling complexity

Mathematical models, generally speaking, are meant to bridge the gap between experiment and theory [177], whereby model *iterations* allow one to converge on good models, and perhaps more importantly, dismiss bad ones as quickly as possible. Often, the complexity of the model is of central importance, and the appropriate choice of number and range of parameters is critical for model tractability and appropriate description of quantitative features, and for use in extracting general principles [60]. If we think of the level of detail of quantitative features as the model *scope*, we can describe any particular model as being relatively placed along an axis between two extremes of *focused* (a small number of equations) and *broad* (a large number of highly coupled equations), and the modeling space can be described as being spanned by two orthogonal axes characterizing model scope and level of realism [111], with the usefulness of the model perhaps governing the exact placement of a model within this space.

The key questions to address in selecting modeling complexity are then: What is the level of detail required and what is the computational cost? The tradeoff between these components requires an appropriate model *approach*, which can selectively emphasize quantitative and qualitative features in appropriate detail.

1.4.3 Modeling approaches

Modeling strategy can further be considered to be of two kinds: forward and reverse modeling [66]. In forward modeling one starts by assembling known or assumed rules,

and asserts (known or simulated) causality to inform predictions, whereas in reverse modeling one begins with experimental data and attempts to explain its causality through an inspired mathematical model [66]. We will present both types of models in this dissertation.

We will consider in Chapter 2 an *agent-based model* (ABM), which we consider to be of the *forward* type in the above definition: rules are established for individual agents and emergent behavior is predicted (namely, by computer simulation). In Chapter 4, we will present a continuum model for cell growth that relies on a partial differential equation (PDE) formulation that we consider to be of the *reverse* type (per above), where observed cell growth and ordering is observed in experimental data and governing equations are asserted as an explanation of this data. We will also present a reverse model to attempt to explain anomalous protein expression using a mechanical-constraint sensory model in Chapter 5.

Mathematical models are able to aid in biological investigations, but also, biology can inform mathematical investigations [94]. In the modeling of microbial communities, there are calls to the importance of close collaboration between theory and experiment in designing, categorizing, and improving these models [175]. We hope to present in this dissertation models that will further the collaboration.

1.5 Outline of the dissertation

The dissertation is organized into a sequence of chapters that present modeling frameworks and their application to the study of mechanical interactions of bacteria in the

context of synthetic biology experiments. In Chapter 2, we present an agent-based model (ABM) of bacterial growth and division for study of bacterial consortia in microfluidic traps. Our model differentiates itself from other published models by the direct incorporation of mechanical constraint measurement into the ABM. We find that tying various cellular dynamics to constraint-driven growth inhibition can direct emergent properties of bacterial consortia in a microfluidic environment, and we argue for the continued exploration and awareness of the role mechanical interactions can play in close-knit bacterial communities.

In Chapter 3, we explore how a decrease in cell aspect ratio can confer a competitive advantage to a bacterial strain by increasing its stochastic, lateral invasion rate in the columnar structures that exist in open-walled microfluidic traps. We suggest that the ability to dynamically control aspect ratio can help optimize synthetic biology experiments by effecting changes in cell *strain ratio*, and that cell-cell signaling via quorum-sensing (QS) communication can be used with aspect ratio changes to manifest a self-regulating population via negative-feedback control.

In Chapter 4 we present an alternative approach to bacterial growth modeling: We develop a continuum model using a system of partial differential equations (PDE) that govern cell growth pressure, the resulting volume-exclusion velocity field, and ordering dynamics. We develop a Poisson's equation for the cell pressure and an advection-reaction equation for the ordering dynamics, where the latter borrows from theory of liquid crystal nematogens under shear flow. We find that our continuum model can predict spatiotemporal ordering of bacterial cells grown in an open-walled microfluidic trap, and that regions of persistent order and disorder can be identified

under the assumptions of the model.

Lastly, in Chapter 5, we explore a mechanical-interaction model that attempts to explain experimental data with anomalous bacterial protein expression. We find our model is consistent, under minimal assumptions, with reproducible anomalies that occur over a large and varied array of experimental conditions. Using the model, we conjecture that a mechano-biosensory response of the cells to mechanical growth inhibition leads to an increased production rate of protein. We suggest that further study of this anomaly is warranted, since such a behavior could be captured as a modular, biosensory component, among the toolkits for synthetic biology research.

Chapter 2

Agent-Based Modeling of Mechanical Interactions in Bacterial Populations

The material for this chapter stems from previously published content by Winkle et al. in the journal *Physical Biology* [171].

2.1 Introduction

Agent-based modeling is a technique whereby individual cells, or agents, interact spatially using predefined rules for each agent, with the goal to discover emergent behavior that is not easily predicted by analysis of the rules *per se*. This type of modeling allows one to explore a larger parameter space by modulating various levels

of interactive or environmental complexity [47], for example. Although in some cases ordinary or partial differential equations (ODE or PDE, respectively) can be used to model cell behavior, these models often fail to capture dynamics due to the large numbers of discrete particles (or agents) and inherent heterogeneity of cell behavior due to stochastic effects [61].

As mentioned briefly in the Introduction, bacterial collectives' spatiotemporal dynamics are determined by complex interaction mechanisms that involve both individual and consortial behaviors. Agent-based modeling provides an attractive approach for uncovering these mechanisms: such models can capture behaviors and interactions at the single-cell level while remaining computationally tractable. The cost and time required for experiments make it difficult to explore the impact of inhomogeneous population distributions and gene activity under a variety of conditions. Agent-based models are far easier to run and modify and they thus provide a powerful method to generate and test hypotheses about gene circuits and bacterial consortia that can lead to novel designs [171].

Importantly, we believe agent-based models of microbial collectives growing in confined environments, such as microfluidic traps, should capture the effect of mechanical interactions between cells in the population. Forces acting on the constituent cells play a critical role in the complex dynamics of cellular growth and emergent collective behavior [44, 142, 143, 152, 38, 146, 48, 14], and biological evolution [49]. We argue that agent-based models, therefore, should be able to model the force exerted by growing cells, as well as the mechanical interactions induced by cell-cell contacts or contact with environmental boundaries. Further, it

has been shown that the environment of an individual cell can influence its growth, which in turn influences the cell collective's behavior through mechanical communication [34, 40, 52, 135, 153]. In particular, mechanical confinement can cause cells within the collective to grow at different rates [34, 40]. Current agent-based models of microbial collectives (e.g. [74, 79, 132, 67, 93]) typically do not allow cells to alter their growth rates in direct response to mechanical sensory input. Adding such capability is challenging, due to the complex relationship between cell growth and the extracellular environment.

As mentioned in the Introduction, the appropriate number and range of parameters in a model affect analytical and computational tractability. We must consider, therefore, the different challenges introduced by modeling mechanical interactions in bacterial colonies. One inherent difficulty is accurately capturing effects that stem from a large number of cell-cell interactions over successive periods of time: Local and global interactions can combine in a highly non-linear way, and the effects of these interactions may not be captured realistically in models of reduced complexity. In particular, growth effects (for example, a modulation of growth rate) in bacterial cells can stem from both competitive and cooperative forces in multicellular communities [133]. Ultimately, the success of a model depends largely on its ability to predict and explain experiments, and adjustments to an agent-based model's complexity must be made to manage the compromise between realism and tractability. Our knowledge of complex systems, however, can remain incomplete while still benefiting from incremental knowledge in reduced-order models of complex, interacting systems.

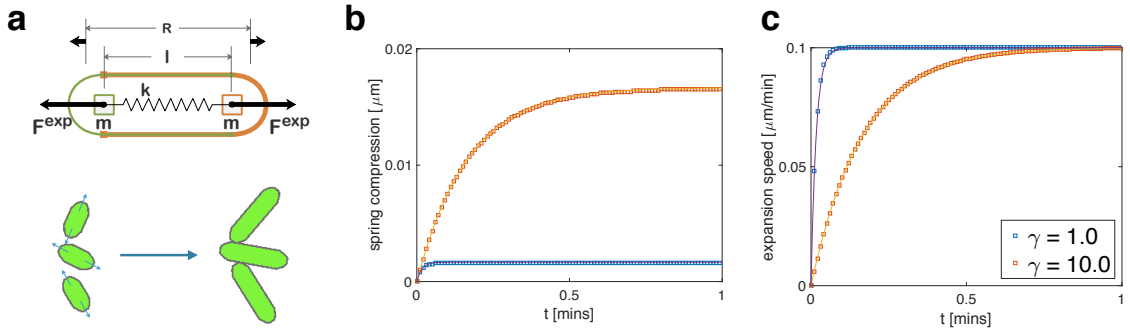


Figure 2.1: **Single-cell construction and dynamics.** (a) A schematic depiction of the components of a single cell in our model. Two symmetric cell halves with semicircular poles and long edges are constrained to align using a ball-and-groove type connection. Each cell half has mass m (assumed to remain constant during cell growth) and center of mass located at the center of its semicircular pole. Growth expansion forces are generated by connecting the two cell halves to a virtual linear spring (with spring constant k) along the cell's long axis, and then extending the rest length, R , of the virtual spring. (bc) Expansion speed (magnitude of the difference between the velocities of the two cell halves) and spring compression (difference between rest length R and cell length ℓ) for a single cell with $\dot{R} = 0.1 \mu\text{m}/\text{minute}$ and a 10-fold increase in normalized resistive damping parameter γ (see Appendix A.4 for normalization details). Simulation data (boxes) match analytical solutions (curves). Increasing γ (orange traces) lengthens the time required for expansion speed and spring compression to reach steady state ($\tau = \frac{\gamma}{2k}$ is the time constant for the first-order system). Larger steady-state spring compression monitors the increased mechanical load felt by the growing cell when the damping coefficient is higher.

Here, we describe an agent-based cell model [171] that focuses on a specific aspect of bacterial growth: the ability to detect and respond to the mechanical environment that emerges in a growing population of bacteria. We show that our model can be used to make predictions about the spatiotemporal dynamics of consortia growing in two-dimensional microfluidic traps. Further, we demonstrate that emergent collective behavior can depend on how individual cells respond to mechanical interactions.

2.2 Modeling framework

To understand the behavior of growing bacterial collectives, we must develop numerical tools that can capture the mechanisms that shape their spatiotemporal dynamics. Here, we propose an agent-based model of bacterial assemblies, using a framework that takes into account mechanical constraints that can impact cell growth and influence other aspects of cell behavior. Taking these constraints into account is essential for an understanding of colony formation, cell distribution and signaling, and other emergent behaviors in cell assemblies growing in confined or crowded environments.

Our framework differs from other published models in an important way: We assume that each cell comprises *two axially independent cell halves* that attach through a compressible, stiff spring, whose rest length increases to induce cell growth (Figure 2.1(a)). The expansion rate of spring rest length sets the target growth rate for the cell. However, in our model the target growth rate will not be achieved due to mechanical constraints, such as resistive damping, cell-cell contact, and contact with trap boundaries. Differences in rest length expansion and actual cell growth result in sustained spring compression, whose energy can be thought of as a *stored growth potential* for the cell. As we will show, *spring compression* serves as a measurement of mechanical constraint in our model, and we remark that it will normally increase even while the cell continuously expands (see e.g., Figure 2.1(bc)). Spring rest length expansion is meant to serve as an imperfect model for cell expansion via turgor pressure, and not as a direct model of peptidoglycan cell wall stiffness [161, 78, 77, 34].

Most published models require that cells grow exactly at *a priori* prescribed rates. An exception is a model introduced to study the organization of crowded bacterial colonies growing in confined niches [34]. As a result, most models do not capture mechanical constraint detection and resultant growth modulation. Our approach introduces greater flexibility than, for example, assuming that growth rate is determined by the position of a cell in a trap [23]. We illustrate the impact of mechanical interactions by starting with simple one-dimensional configurations and then moving to more complex, two-dimensional geometries. In addition to serving an illustrative purpose, one-dimensional configurations allow us to validate our numerical implementation. Our model is explicitly solvable when cells are constrained to grow in one dimension, which allows us to validate our simulation environment by comparing numerical and analytical solutions in this case. Further, our 1D results provide a benchmark for the interpolation of 2D dynamics.

When constructing our simulations and diagrams, we took advantage of two open-source software resources: the physics engine `Chipmunk 2D` [3] for cell dynamics, and the cell simulation platform `gro` [79] (which itself uses `Chipmunk 2D`). We initially modified `gro` to implement our new cell model within the physics engine, while taking advantage of the `gro` visualization environment and image capture capability (Figs 1–4 in our manuscript each contain images generated using this feature). We then developed and used an independent command line version (run on server computing resources) for larger parameter sweeps, as well as to generate data for statistical analysis.

2.2.1 Cell construction

We model each bacterium as an assembly of two independent cell halves. To model cell growth, we assume that these two halves expand symmetrically along the long axis of the bacterium (Figure 2.1(a)). Each cell half consists of a mass m at the center of a semi-circular pole, which connects to straight, long-body edges (as shown by different colors in Figure 2.1(a)). The two masses connect through a virtual spring with linear spring constant k . Importantly, the rest length of the spring increases in time. In confined environments, extension of the rest length induces forces on neighboring cells, microfluidic trap boundaries, and any other obstacles the cell may encounter.

In order to ensure the cell halves act as a single, well-defined cellular unit (for example, upon collision with other cells or fixed barriers), we use a pair of symmetric ball-and-groove type connections so that the cell halves remain aligned and resist bending [77]. This also ensures that any off-axis or rotational impulses are transmitted equally to both halves of the cell. Thus, cell growth forces are designed to act independently in the axial direction, whereas off-axis, cell-external forces act on the cell as a whole. We remark, however, on a caveat of our model: Sufficiently large *on-axis* components of external forces could result in a cell-length compression, but we mediate this using a rigid-body, back-filling “ratchet” algorithm (details about the implementation are provided in Appendix A.5). Thus, although *spring compression* is an integral component of our cell model, we intervene separately to prevent *cell compression* by using a nonlinear technique.

2.2.2 Growth model

We induce axial cellular growth by extending the rest length, R , of the virtual spring that connects the cell halves (Figure 2.1(a), top panel). Induced expansion force can be felt by all neighboring objects (see Figure 2.1(a), bottom panel). Cho et al. [34, Figure 4] used a related model to study how mechanical constraints lead to self-organization in bacterial colonies grown in confined environments.

Crucially, rest length extension is an adjustable component of our model that captures the growth *tendency* of each cell. As we will see, altering how rest length extension dynamics respond to constraint can impact global dynamics of collectives. To start, however, in Sections 2.2 and 2.3 we assume that the rest length grows at a constant rate, $\dot{R} = a$. In this case, mechanical constraints can result in unphysiologically large potential energy stored in a highly compressed spring, an issue we address in subsequent sections.

We assume cells grow in an extracellular fluid with a resistive damping parameter, γ , and that our system is in the non-inertial dynamics regime (see Appendix A.1). Fluid damping resists cell growth via a damping force $\gamma\dot{x}$, where \dot{x} is the lab-frame speed of a cell half through the extracellular fluid. We explicitly model this parameter to explore the effects that fluid damping variations have on cell dynamics. Although γ defines non-inertial dynamics over a broad range of values, we will see that it directly governs response dynamics under the assumptions of our growth model. We make the simplifying assumption that γ captures all sources of resistive damping, including extracellular fluid damping and dissipative (non-Hamiltonian) damping forces within

the cell itself. In particular, γ serves as an imperfect but computationally manageable proxy for cell-internal spring damping.

Many published agent-based models treat bacterial cells as unitary rigid bodies under non-inertial dynamics that achieve cell growth by a process we will call the *Expansion, Overlap, Relaxation* (EOR) method. In these models, forward Euler integration of the growth rate a expands (E) a cell by increasing its length by $a \cdot dt$, where dt is the time discretization step. If a cell is sufficiently near, or in contact with, another object (for example another cell or a trap wall) just before this time step, expansion will result in overlap (O). A relaxation algorithm (R) is then asserted that resolves (or prevents) overlaps of all cells and objects using repulsion forces [34], constraint [132], iteration [79], or a related algorithm [67, 93]. EOR methods have thus been used in a wide variety of contexts. However, these methods handle mechanical interaction in an opaque way, whereas our framework allows us to model a measured cell response to mechanical constraint in an explicit, transparent way.

In our model, we prevent cell overlap by using *collision dynamics* to resolve competing growth expansion under the constraint of cell-cell or cell-barrier contact (see Appendix A.4). Importantly, by constructing a cell with two axially independent halves, we do not have to assume that each cell reaches a predetermined size, determined by the growth rate, at the end of each time step. In contrast to the EOR method, this allows us to determine the impact of mechanical constraints on the growth of a cell by comparing the achieved cell length ℓ to spring rest length R at each time step. We can then link this measurement (which is made by the cell agents themselves), to other aspects of the cell model. As we will see in a later section in

this Chapter, emergent assembly behavior can depend on how cells modulate growth in response to constraints.

2.2.3 Equations of motion for an isolated cell

We develop an analytical description of our cell growth model in order to study the behavior of interacting cells in confined environments. We first derive the equations of motion for an isolated cell in an extracellular fluid with resistive damping parameter γ . Cell growth results from a linear spring force computed from the difference between ℓ and the rest length R of our virtual spring ($R - \ell$ is thus spring *compression*) and applied equally to each cell half. Using linear spring constant k , we have the inertial equation of motion for an isolated cell,

$$\frac{m\ddot{\ell}}{2} = k(R - \ell) - \frac{\gamma\dot{\ell}}{2}. \quad (2.1)$$

Assuming non-inertial dynamics (see Appendix A.1), Eq. (2.1) yields a differential equation for expansion velocity,

$$\dot{\ell} = \frac{2k}{\gamma}(R - \ell). \quad (2.2)$$

In order to close Eq. (2.2), we must describe the dynamics of the rest length, R . Bacteria grow approximately exponentially (see [10] and references contained therein). However, for simplicity we let R extend linearly at rate a , independent of cell length. This assumption can be relaxed, and does not affect the main points below. In Section 2.4, we will introduce *mechanical feedback* by modulating \dot{R} in response to mechanical constraint.

Setting $R(0) = 0$, we have $R(t) = at$, so Eq. (2.2) becomes

$$\dot{\ell} + \frac{2k}{\gamma}\ell = \frac{2k}{\gamma}at. \quad (2.3)$$

Defining $\tau = \frac{\gamma}{2k}$, setting initial cell length, ℓ , to zero, and solving Eq. (2.3) gives the length of an isolated cell, and the rate of its expansion,

$$\ell(t) = a(t - \tau + \tau e^{-\frac{t}{\tau}}), \quad \dot{\ell}(t) = a(1 - e^{-\frac{t}{\tau}}). \quad (2.4)$$

The parameter τ acts as a time constant for growth dynamics. Eq. (2.4) shows that $\dot{\ell} \rightarrow a$, and that τ governs the time required to reach steady state. Because τ is proportional to resistive damping γ for fixed k , resistive damping therefore governs this lag. Using Eq. (2.4), the compression of the spring that drives the growth of the isolated cell is given by

$$R(t) - \ell(t) = at - a(t - \tau + \tau e^{-\frac{t}{\tau}}) = a\tau(1 - e^{-\frac{t}{\tau}}). \quad (2.5)$$

Notice that Eq. (2.5) implies that $(R - \ell) \rightarrow a\tau$, a measure of the sustained mechanical constraint felt by an isolated growing cell at steady state due to resistive damping.

As described in Appendix A.4, we have implemented this model using the **Chipmunk** 2D environment. To validate our implementation, we first compared the growth of an isolated cell to that given by Eq. (2.4). We varied resistive damping γ by an order of magnitude, while using units such that $k = 1$, and γ was changed from 1 to 10. Figure 2.1(bc) shows close agreement between theory and simulation for spring compression and expansion speed. The timescale at which both approach their equilibrium values increases with γ .

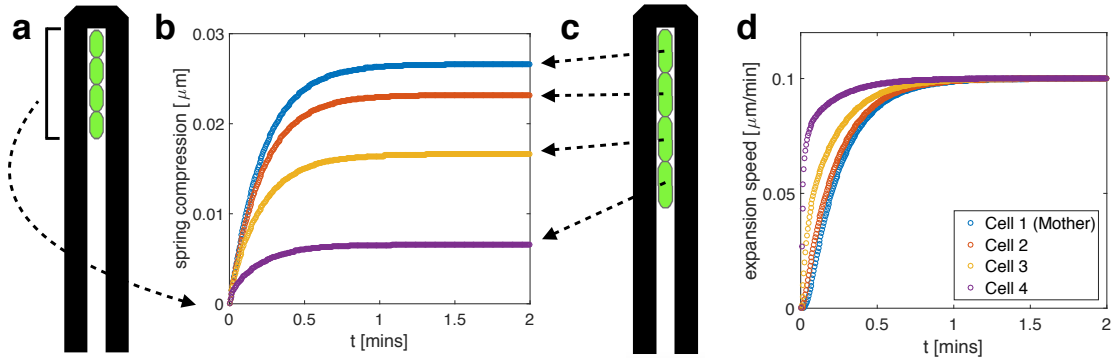


Figure 2.2: **1D mother machine trap simulation.** (a) A schematic depiction of the mother machine trap setup. Four cells were placed back-to-back from the closed top of the trap and grew toward the open end (c). (b) Spring compression depends on cell position. In equilibrium, compression is lowest for the lead cell and highest for the mother cell. Higher equilibrium spring compressions near the back of the trap reflect the higher mechanical inhibition detected by cells close to the mother cell. Equilibrium spring compression is a quadratic function of position in the trap (see Figure A.1). (d) Expansion speed depends on cell position. Although all four cells eventually reach the same steady-state expansion speed, cells near the back of the trap take longer to do so. Rest length expansion rate was set to $\dot{R} = 0.1\mu\text{m}/\text{minute}$ and initial cell length was $2\mu\text{m}$. Spring constant k and damping parameter γ were set to 1.0, as in Figure 2.1.

2.3 Behavior of cells in a mother-machine

To bridge the divide between a single, isolated cell and collectives growing in general two-dimensional geometries, we now study a one-dimensional ‘mother machine’ configuration, where cells are constrained to grow in long, narrow traps. Mother machines are microfluidic devices developed to study bacterial cell growth and division over hundreds of generations (see [1, 167]). They consist of an array of impermeable, three-walled narrow channels, each just wide enough to hold a line of cells. The open end of each channel is perpendicular to a ‘trench’ through which fresh nutrient

medium flows. Cells exiting the narrow channels are carried away by this flow.

We simulated a mother machine using a single three-walled barrier that allowed cells to grow in a single file. We initialized cells in the channel by placing them pole-to-pole, with the ‘mother cell’ placed against the back wall (Figure 2.2(a)). As cells grew, they were constrained to move toward the open end of the narrow channel. Using the model of cell growth described in Section 2.2, we simulated an array of four cells with constant rest length extension rate, $\dot{R} = a$, and recorded their resulting spring compressions (Figure 2.2(b)) and cell-frame expansion speeds (Figure 2.2(d)).

We see that cell growth rates and spring compressions equilibrate after a transient time determined by the spring constant, resistive damping parameter, and cell position in the mother machine. This model predicts that the growth rate of the lead cell (the cell closest to the open end of the trap) equilibrates most quickly, and is the least compressed. This is intuitive, since cells deeper in the trap must overcome the cumulative resistive drag of those nearer the open end. A similar point is raised in [62] for cells exhibiting frictional forces in a chain, where the first cell in the chain is shown to experience the maximal horizontal stress. Analytically, we describe the growing line of cells as a coupled mass-spring system (see Appendix A.4), whose dynamics match the simulations illustrated in Figure 2.2. Solving our analytical model shows that steady-state spring compression in a 1D line of cells is a quadratic function of cell position, as Figure 2.2(b) suggests.

These simulations illustrate cell behavior resulting from competing growth and resistive forces of neighboring cells in a simple geometry. We note that steady-state compressions are relatively small in this example, due to the small number of

interacting cells. Compressions can grow substantially, however, in larger traps due to increased cell confinement and resulting interaction forces, as we will see in the next section. Local constraint detection can significantly influence the global dynamics of growing collectives in two-dimensional geometries, as we now demonstrate.

2.4 Two-dimensional microfluidic trap geometries: results and predictions

We next study bacterial assemblies in two-dimensional geometries. We start with a two-strain microbial consortium growing in a long, narrow trap with open sides. Our model predicts that, after a transient period, strains grow in vertically-oriented, curvilinear stripes perpendicular to the longer edge of the trap. Each stripe behaves as a collection of quasi-mother machines. Defects in the stripes form close to the shorter edges of the trap. While boundary geometry is known to direct the collective orientation of bacterial colonies growing in traps with hard walls [34, 165], our prediction of emergent spatiotemporal patterning in open traps is perhaps surprising. In a final study (Section 2.4.2) of an assembly growing in a trap with three walls, we examine how allowing target growth rate to depend on spring compression affects both the global dynamics of cell alignment and a generic protein expression model. Our model predicts that both protein expression and the nematic (angular) ordering of the cells depend on how rest length extension rate \dot{R} varies with spring compression.

2.4.1 Two-strain consortium growing in an open trap

Agent-based models of cellular growth have provided insights into the spatiotemporal dynamics of collectives [14, 79, 23, 131, 93, 146, 48, 49]. Here, we use our agent-based model to examine the evolving distribution of two non-interacting strains in a microfluidic trap open on all sides (see Figure 2.3(a)). Once a cell reaches the boundary of the trap, we assume that it is rapidly carried away by the flow of the media through a channel surrounding the trap. We simulated this by removing such cells from the simulation. We initialized the simulation by randomly placing several seed cells of each type into the empty trap. Cell growth forces in this example were induced by a constant rest length extension rate, $\dot{R} = a$.

Figure 2.3(a) illustrates a typical spatiotemporal pattern that emerges after cell growth and resultant colony expansion of the initial seed cells. Cells organize into vertically-oriented, curvilinear stripes, each composed of a single strain (except for cells near the left and right boundaries, which tend to flow horizontally toward their nearest exits). Each curvilinear column of cells operates as a quasi-mother machine: Cells at the center of the column act as ‘mother cells,’ while descendants form outer components that flow vertically toward the trap boundary.

Our simulations predict that strain ratio is relatively stable once these stripes emerge. What determines this stable ratio and the width of the stripes remains unclear, since the transient dynamics that precede this quasi-steady state are complex. The strain type of the central cell in a given curvilinear cell column determines the strain type of all of the cells in the column. To predict the stable strain ratio, it

is therefore sufficient to predict how the distribution of central cells emerges. However, this depends sensitively on the initial distribution of cells, the relative growth rate of the two strains, and other factors [122]. Stability of the strain ratio in our simulations emerges from the stability of the quasi-mother machines and their columnar flow, which inhibits cells from lateral motion; notably, only lateral displacement at the *mother cell position* by a different strain can influence the strain ratio non-transiently.

Figure 2.3(b) illustrates the empirical distribution of normalized cell compression over the duration of a simulation. Each horizontal cross-section of this heat map represents the empirical probability density for compression at a given trap depth. As expected, the empirical compression data is consistent with the behavior of a one-dimensional mother machine. In particular, mean compression is highest in the center of the trap, and tapers quadratically as one moves to either of the horizontal trap boundaries (we will see that deviations from this quadratic behavior emerge in three-walled traps). Relatively sharp peaks of the distribution at the long edges of the trap indicate the low variability of spring compression for cells at the boundary of the columnar flow.

2.4.2 Varying the rest length extension program

Thus far we have assumed that rest length extension rate is constant. We now explore the global implications of allowing rest length extension rate to vary with spring compression in our model. This study is motivated by experimental evidence

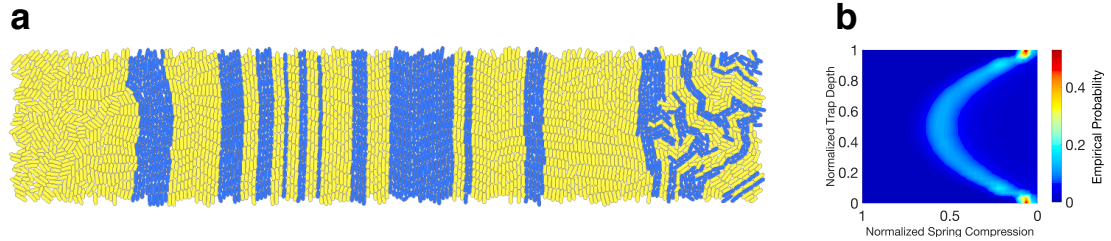


Figure 2.3: **Emergent behavior in a long, narrow microfluidic trap.** We simulated a two-strain consortium growing in a two-dimensional trap open on all sides. Cells were removed from the simulation once center of mass crossed a trap boundary. We initialized the simulation by randomly placing several seed cells from each strain into the trap. Strains are non-interacting, with yellow and blue colors representing strain type (yellow and blue colors chosen arbitrarily to elucidate emergent striping patterns). **(a)** After the trap filled, the strains organized themselves into vertically-oriented curvilinear stripes consisting of curvilinear columns of cells. Each such column functioned as a quasi-mother machine. **(b)** Empirical distribution of normalized cell compression over the length of the simulation. Each horizontal slice represents the empirical probability density for compression at a given trap depth. Heat map coloring reflects normalized probability for each horizontal slice. Mean compression is highest in the center of the trap and tapers quadratically, as our theoretical analysis of a mother machine predicts. The dimensions of the trap were $40\mu m \times 200\mu m$. All other parameters were set as in Figure 2.2. Spring compression is normalized to set the quadratic peak near 0.5.

supporting the thesis that mechanical forces shape the dynamics of collectives [159, 135, 52, 48, 49, 146]. In particular, it has been shown that mechanical forces can become sufficiently large to slow cell growth [40]. How to best model the impact of such mechanical constraints on cell growth remains unclear. Here, we therefore consider a simple model of how cells modulate their target growth rates in response to mechanical forces, and explore the impact of such growth modulation on the emergent properties of the collective.

We introduce a simple growth rate dependence by setting \dot{R} to a constant value for low values of spring compression $C = R - \ell$, while decreasing it linearly to zero after compression crosses a threshold, T . More precisely, we set

$$\dot{R}(C) = \begin{cases} a, & \text{if } C \leq T; \\ a(2 - \frac{C}{T}), & \text{if } T < C < 2T; \\ 0, & \text{if } C \geq 2T. \end{cases}$$

We simulated a three-walled trap geometry, as illustrated in the left column of Figure 2.4. The first row of Figure 2.4 shows simulation results for a high threshold T_h of spring compression, the second for a low threshold T_l .

The center column (panels (c) and (d)) shows normalized spring compression distributions over the lifespans of the simulations. The spring compression is normalized (independently in each case) such that $T_{h,l} = 0.5$. As before, a horizontal slice represents the empirical probability density for cell compression at a given trap depth. Three regimes emerge: In the bottom section of the trap, the compression profiles are quadratic, suggesting behavior akin to the quasi-mother machine dynamics we

examined previously; mean compression levels off beyond the bottom section of the trap before spiking in the back. The sharply increased spring compression at the back wall emerges from the horizontal alignment tendency of cells in this area. Cells parallel to the back of the trap have no open trap boundary in their axial growth direction, which results in marked mechanical confinement as evidenced using both thresholds in our simulations.

Implications for protein accumulation

Spring compression in our model can thus cause cells within the population to grow at different rates. This heterogeneity has implications for protein accumulation in growing collectives. Although the mechanisms of coupling are largely unknown, mechanical deformations are known to influence protein enzymatic activity [152]. We considered a simple case in which the amount, x , of some protein in each cell obeys the differential equation

$$\dot{x} = \alpha\ell - \beta x,$$

where α denotes basal production rate and β is the rate of chemical degradation. When a cell divides, protein is distributed to the daughter cells in proportion to their lengths. The left column of Figure 2.4 contains snapshots with cells shaded according to x/ℓ , *i.e.* protein per length of cell. As we assumed volume is proportional to length, the shading represents protein concentration within the cells, with brighter cells having a higher concentration of protein.

Protein concentration is highest in the back of the trap, consistent with the fact

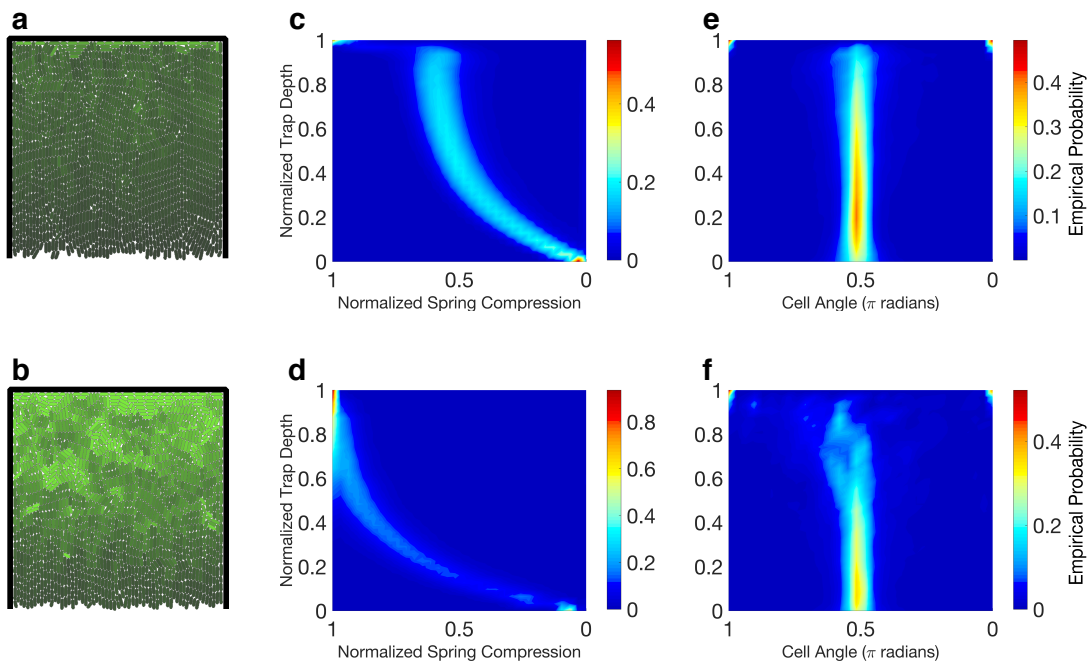


Figure 2.4: **Emergent dynamics as a function of rest length extension rate versus spring compression profile.** Single-strain collective growing in a three-walled trap. Rest length extension rate \bar{R} is constant when spring compression is small, but decreases linearly after compression crosses a threshold. First row: high threshold; second row: low threshold. **(ab)** Concentration of a constitutively-produced protein (brighter color indicates greater concentration.) Protein concentration is highest in the back of the trap because typical cell division time is longest there. Lowering the compression threshold leads to a significant increase in protein accumulation. **(cd)** Distribution of normalized compression over the lifespans of the simulations. Each horizontal slice represents the empirical probability density function for compression at a given trap depth. Heat map coloring reflects normalized probability for each horizontal slice. **(ef)** As in (cd), but for cell angle instead of compression. Notice that nematic disorder in the back half of the trap is greater with lower compression threshold. Trap dimensions: $65\mu m \times 65\mu m$.

that spring compression is highest there. Significantly more protein accumulation occurs when the threshold T is low (bottom snapshot). We remark that compression dynamics can be ‘faster’ than protein dynamics in the following sense: When a cell under significant constraint and expressing a large amount of protein suddenly becomes dislodged (unconstrained), it may take several generations for protein concentrations in descendant cells to return to levels consistent with equilibrium in unconstrained cells.

Implications for nematic order

We finish by examining how nematic order is affected by altering the rest length extension rate vs. spring compression profile. The right column of Figure 2.4 shows cell angle distributions over the lifespans of the simulations. An angle of $\pi/2$ corresponds to a vertically oriented cell. Each horizontal slice in the figure represents the empirical probability density function for cell angle at the given trap depth. When the threshold T is high, as in Figure 2.4(e), cells show strong vertical alignment throughout the trap. We observe significantly more nematic disorder with a lower threshold (Figure 2.4(f)).

Boyer et al. [23] have shown that nematic disorder in three-walled trap geometries can be caused by a buckling instability. Under the assumption that cells in the back of the trap both slow their growth and are smaller due to nutrient depletion, they further show that nematic disorder will be more prevalent there since small cells are more likely to buckle (Figure 5 of [23]). By reducing T in our simulations, we

observe that reduction of cell growth rate alone leads to strong nematic disorder in the back of a three-walled trap geometry. Consequently, we have recapitulated the Boyer result. However, in our case the mechanisms are different: Nematic disorder emerges solely from slowing cell growth rate, which follows directly from detection and response to mechanical interactions, and not from postulated nutrient depletion.

2.5 Discussion

The growth of cells, both in natural environments and experimental conditions, is modulated by a number of factors. These include mutations, nutrient depletion, extracellular forces, and environmental signals. Cells actively respond to mechanical forces, which implies they are capable of sensing and transducing these signals to a biological response [72]. Here, we have described a simple model of how bacteria can effect changes in their growth in response to mechanical interactions. We have shown that such changes can impact the spatiotemporal dynamics of bacterial collectives growing in microfluidic traps.

However, our model is certainly an oversimplification. We do not address the biological accuracy of our spring constant k with respect to bacterial cell wall models that also use springs (for example [161, 78, 34, 77, 152]). Our spring model generates expansion forces using a simple, linear dynamical equation, but model parameters are constrained by computational cost (see Appendix A.4). We attempt to strike a balance between physical realism and simulation time, while arguing for inclusion of a mechanical constraint measurement in a simple, agent-based model.

Further, we did not attempt to describe the other factors that modulate cell growth and can lead to emergent dynamical phenomena. For instance, assume that the growth rates of two co-repressing strains in a consortium depend on their transcriptional states, so that the strain that has the higher level of expression grows more slowly. This type of interaction between cell growth, strain competition, and protein expression can lead to relaxation oscillations in both transcriptional and growth rates [136]. We expect that a variety of mechanisms that affect growth rates of single cells, directly or indirectly, can lead to emergent phenomena at the level of the bacterial population.

Our agent-based model stands in contrast to most previously developed models: We allow cells to follow first-order dynamics rather than assuming cells achieve their target growth rates in each time step. Thus, cells can monitor the environment and respond to mechanical interactions by modulating growth and, potentially, other aspects of their interior dynamics. It is unclear whether a cell that is prevented from growing stores this potential. However, mechanical interactions certainly impact cell growth even when nutrient supply is adequate. This is confirmed by experiments performed in osmotic shock, where not only do cells no longer grow, they also return to the cell length they would have achieved, had shock not occurred [77].

Although our model is an oversimplification, it shows that mechanical interactions can play an important role in the organization and dynamics of growing bacterial collectives. We have described a flexible platform for understanding these effects. But much work remains: The predictions of these models, such as the organization of colonies in microfluidic traps and the impact of crowding on gene expression, will

need to be validated experimentally. A deeper understanding of the emergence of order and disorder in these bacterial populations will require the development of effective continuum models of collective cell dynamics [165]. Agent-based models of the type we describe can serve as a starting point for these further developments.

Chapter 3

Competition of Bacterial Strains through Changes of Cell Aspect Ratio

We now study how bacterial cell aspect ratio can affect cell-cell interaction dynamics between two strains of *different* aspect ratio in a microfluidic trap. We investigated these dynamics by designing and observing simulations using the ABM and simulation environment presented in Chapter 2. We conclude that a smaller aspect ratio strain has a competitive advantage in a microfluidic trap: Given an ability to *change* aspect ratio under induction within a single experiment of two strains, a smaller aspect ratio strain can out-compete the other purely through mechanical interactions, leading to total extinction of the wild-type strain from an initially stable and well-mixed population.

3.1 Introduction

Bacterial cells maintain precision and accuracy in their cell shape through multitudes of generations of growth [57]. The exact mechanisms and machinery to this constancy are widely unknown, but cooperation of hydrolase and synthase enzymes acting on a cross-linked biopolymer known as peptidoglycan is known to play a role [75]. One bacterial protein known as MreB participates in the control of cell shape and can determine whether, for example, a cell takes on a more “coccal” (spherical) or a more rod-like shape [81, 82, 145]. Another bacterial protein known as FtsZ is a tubulin homolog, which is required for daughter-cell separation (cytokinesis) in most species of bacteria [140, 152].

Mechanical interactions of bacteria have been widely studied in the context of biofilm development [19, 26, 43, 102, 118, 105] and specifically, cell shape has received increasing attention for studying consortial dynamics in biofilms [131, 146, 4, 49]. In Rudge et al., fractal patterns were studied with respect to the anisotropic, axial growth forces of bacteria. They demonstrated that changes in cell aspect ratio can change a self-similarity measure of resulting colony growth, with a reduced aspect ratio leading to reduced fractal dimension [131]. In Smith et al., cell strains of different morphologies were competed to study how cell shape affects patterning and evolutionary fitness in growing colonies. In 2-D and 3-D simulations, they showed that rounder, more “coccal-shaped” cells could travel to the front of growing colonies, which gives them a selective advantage in some environments [146]. Similarly, Farrell

et al. showed that cells of smaller length have a higher probability for “surfing mutations” at the front of a growing colony to form a macroscopic, surviving sector [49]. Acamel et al. showed that clusters of cells in a model of growing biofilms showed different degrees of ordering as a function of cell aspect ratio in what they refer to as a “Brownian Dynamics” environment [4].

In each of the studies described above, computer models were used alongside experiments to reinforce and help explain behavior of two strains interacting mechanically. Also in each case, the strains were what we shall call *aspect ratio static*, where each strain was, up to variation due to cellular noise, fixed in aspect ratio throughout a single experiment. We aim to extend the above studies by introducing *dynamic aspect ratio control*: We will explore consortial behaviors when one cell strain *changes* its aspect ratio. For example, we can change a strain’s aspect ratio from being equal to that of another strain to being smaller, which we will see provides a competitive advantage in a microfluidic trap.

Our model has been realized neither in experiment nor in simulation, as far as we know from the published literature. The bacterial cell transformations necessary to effect a cell aspect ratio change dynamically, however, have no known limitation to their realization as an experimental design. We omit in our presentation any detailed discussion of the laboratory procedures or genetic transformation techniques necessary to achieve the dynamic aspect ratio control we are proposing in this Chapter. Instead, we limit our model to the expression of a single protein (which may be MreB or FtsZ, for example), whose expression in a bacterial cell strain leads to a decrease in the average cell aspect ratio of that strain.

Of particular note in our study as compared to the aspect ratio static studies cited above is the *timescale* at which we can observe dynamics in a simulation of a microfluidic trap experiment: We attempt to explore these dynamics through mechanisms of temporal and spatial control (i.e., epigenetically) rather than through fixed changes in the bacterial genome. This allows us to observe interaction dynamics on a much faster time scale than that of iterative experiments themselves. We will show that — in the experimental environment of microfluidic traps — dynamic modulation of cell aspect ratio leads to radical changes of cell *strain ratio*, and that these population dynamics stem from a purely mechanical competition between strains that manifests directly from differences in their cell shape.

3.2 Simulation results

3.2.1 Simulation model

To explore predictions of consortial behaviors of bacterial strains in microfluidic traps with dynamic changes of aspect ratio, we again turned to our agent-based model (ABM) presented in Chapter 2. Our simulation model is exactly as presented in Chapter 2, except for the following:

1. At a fixed time in the simulation, we changed the division length for one strain in a two-strain microfluidic trap experiment simulation to be smaller by a fixed ratio that we shall call Γ , where $\Gamma \leq 1$.
2. We replaced our uniform growth rate with an exponential growth rate such

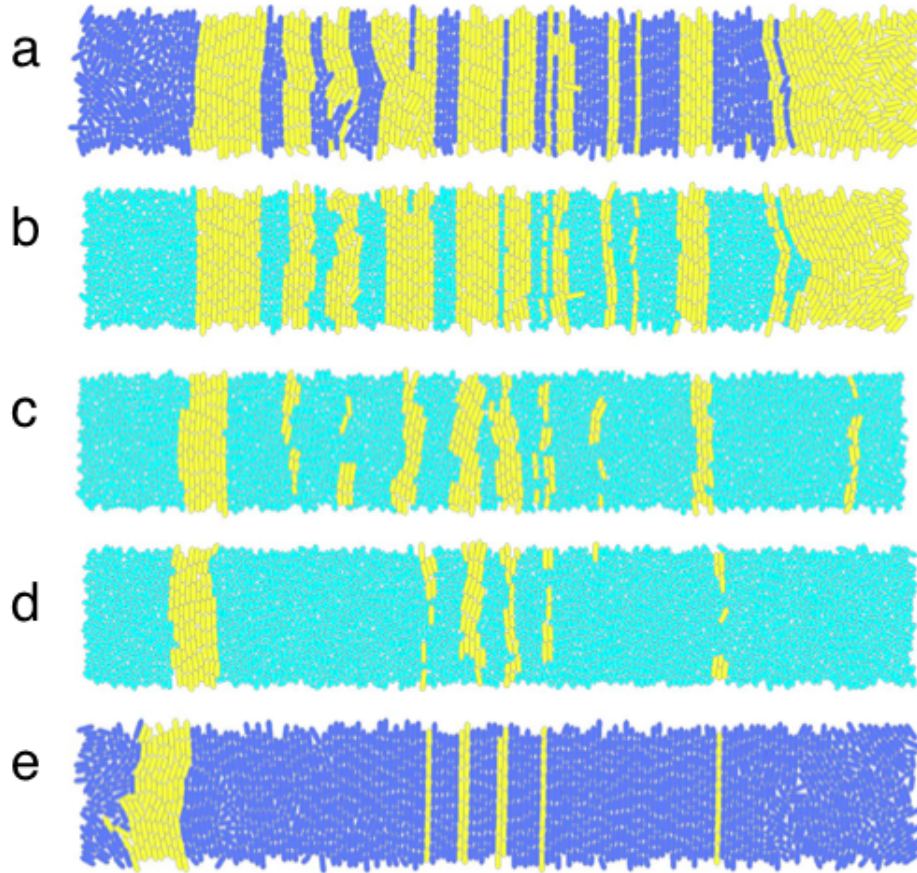


Figure 3.1: **Lateral invasion by a strain with altered aspect ratio** A 2-strain simulation in an open-walled, $20 \times 100 \mu\text{m}$ trap shows dynamical effects from a change of aspect ratio in one of the strains, with all other parameters identical in the strains. **(a)** Cell striping that nearly stabilized from an initial random seeding of cells. **(b)** Shortly after the blue strain (now colored cyan) was modulated to grow and divide at approx. $2/3$ its original length, cyan cells began to laterally pierce vertical stripes of yellow cells at random locations (cell *growth rate* did not change in the cyan strain). **(c)** Cyan cells eventually dislocated mother-cell positions of yellow cells, which ejected the yellow stripe from the trap under symmetric volume-exclusion cell flow. **(d)** The cyan strain had nearly taken over the middle section of the trap before the aspect ratio switch was turned off. **(e)** Blue color indicates the return to identical length parameters for the 2 strains. A few isolated, non-ejected yellow mother cells re-extended to vertical stripes.

that the doubling time of a cell was 20 minutes, irrespective of its length.

3. We omitted any growth-rate dependence on the cell growth pressure (see Chapter 2, section 2.4.2).

3.2.2 Aspect ratio change leads to lateral invasion

In Figure 3.1, we show the results of a simulation experiment in an open-walled microfluidic trap. The simulation was seeded (as in Chapter 2) by randomly placing an equal number of each of the two types of strains in the trap. The two strains are colored yellow and blue, where yellow is the wild-type (WT) strain that remained at a constant aspect ratio, and blue is the “invading” strain, whose aspect ratio decreased at a predetermined time in the simulation. When the invading strain was “induced” to change aspect ratio, we indicate this change in the figure by changing its color to cyan. In this simulation experiment, the aspect ratio was changed by a factor $\Gamma = 0.7$.

As seen in the figure, as soon as the invading strain changed aspect ratio, it aggressively invaded the WT strain by “clipping” it laterally. We explain this behavior in the following way: If the invading strain rotates into an adjoining column and successfully invades the all-important positions in the middle of the columnar structures of cells, it establishes itself as a mother cell locally (see the discussion in section 2.4.1). The invading strain can also invade laterally at other positions in the columns, but these will be transient and not directly result in an invasion of the entire column since, due to the columnar expansion flow of cells in vertical alignment

in this trap geometry, the invasions will be flushed by the cell flow.

This phenomenon is caused by an apparent increased rotational mobility of the smaller aspect ratio strain, which allows it to align its growth axis *perpendicularly* to the adjacent columns of cells to effect the lateral invasion. Close inspection of the image sequences revealed that this behavior is stochastic. The large number of cell-cell mechanical interactions that exist among the $\approx 10^3$ cells in close-packing in the trap is consistent with this observation.

Subsequent panels in the figure show the continued decimation of the WT strain until, in this simulation experiment, the invading strain was “switched off” by returning it to its original aspect ratio such that both strains were again identical in phenotype. The last panel in Figure 3.1 shows that stabilization of columns returned after the equilibration of the aspect ratio.

3.2.3 Discussion

Bacterial cells typically grow and divide with a 20-30 minute division period: a cell extends from $\approx 2 \rightarrow 4 \mu\text{m}$ in this time, divides, and continues the process with the daughter cells in an exponential growth phase (as long as nutrients are available to the growing colony) [69]. In microfluidic trap experiments, this colony size (by design) stabilizes by ejecting cells out of the trap at the same average rate that they double within it. Sufficient nutrients are then provided to a relatively constant population of cells, which allows the experimentalist to observe a continuously regenerating colony and perform experiments with a stabilized population number. However, one issue

in the study of *consortial* behaviors in microfluidic traps is the stability of strains with respect to strain-width distribution and overall strain ratio. Studies with two or more strains require the cells to be within a maximum strain-to-strain signaling distance and to be sufficiently well-mixed (so that one strain does not dominate the study or fix the population, for example).

Looking again at Figure 3.1, we see that initially (in panel a) strains were fairly well-mixed and the average stripe width was relatively small (compared to the width of the trap). After the decimation, however, we see that the blue strain had a significantly larger average stripe width (panel e) and the yellow strain remained in only a few, isolated stripes. We can now, however, think of this process in reverse: given panel e in Figure 3.1 as an *initial condition*, could the yellow strain invade the blue strain through dynamic aspect ratio control to recover a well-mixed population in the trap?

We consider this compelling idea in the final discussion section of this Chapter. We first continue, however, with a more systematic study of the dynamics of bacterial consortia

3.2.4 Strain ratio dynamics vs. aspect ratio change

In another simulation experiment, we systematically changed the aspect ratio over a range of values to observe the differences in invasion rate of the smaller strain into the columns of the WT strain. In order to isolate these differences and eliminate effects from variations of initial seeding or strain striping width distribution that

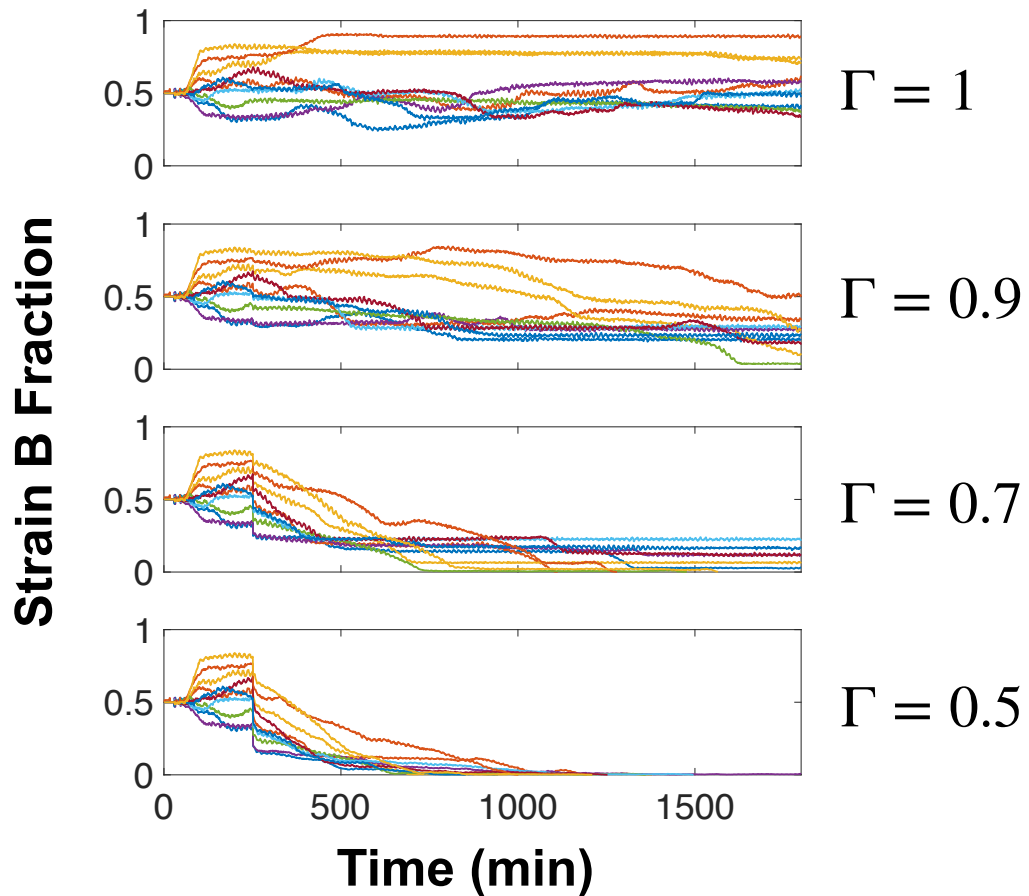


Figure 3.2: **Strain ratio dynamics vs. aspect ratio of the invading strain.** A 2-strain simulation using the ABM framework from Chapter 2. Four examples of an open-walled, $20 \times 100 \mu\text{m}$ trap show dynamical effects from a change of aspect ratio at time $t = 250$ min. in one of the strains (all other parameters being equal). In contrast to Fig. 3.1, the aspect ratio change is persistent after initiation. Γ represents the scaling of aspect ratio in the invading strain as compared to the wild-type (WT) strain ($\Gamma = 1$ represents identical strains). The WT strain divides at length $\ell \approx 4.5$ microns and division is stochastic per our ABM framework from Chapter 2. Variant strains in the three other examples divide at length $\Gamma\ell$. Each plot shows 10 iterations of 32 randomly-seeded initial cells randomly chosen of each strain, with each of the 10 iterations using identical seeding for each value of Γ . The control simulation with $\Gamma = 1$ shows stabilization of strain ratio after an initial transient, which is typical of our open-walled trap simulations and in experiments. Decreasing Γ shows marked increase of the rate of decimation of the WT strain. The sharp decreases at time $t = 250$ mins. are due to the rapid change of cell number after initiation of the dynamic aspect ratio change. Y-axis of each plot represents WT fraction of cells.

would result, we initialized our pseudo-random number generator to an identical value for each aspect ratio value simulated. For each aspect ratio we simulated multiple realizations; however, each enumerated realization was then identical in initialization and random-number generation to that of the corresponding realization for each aspect ratio. This uniformity across realizations allowed direct comparison and isolation of the effect of aspect ratio on strain ratio dynamics.

In Figure 3.2, we show results of 10 simulation realizations across 4 changes of aspect ratio in an open-walled microfluidic trap. We asserted the change in aspect ratio to the invading strain at time $t = 250$ min., which allowed sufficient time for strain ratio and columnar organization of the strains to stabilize. As can be seen in the figure, each of the 10 initializations were identical in behavior up to the initiation of aspect ratio change of the invading strain.

In the control simulation ($\Gamma = 1$), strain ratio was consistently stable: mechanical interactions among WT strains of identical aspect ratio did not favor rotation and lateral invasion. However, a decrease in aspect ratio corresponded to an increase in the invasion rate, as evidenced by the increased rate of decay of the WT strain fraction in each of the realizations. These results clearly show that aspect ratio can dynamically control strain ratio.

In order to compare these results with differences in aspect ratio at the *beginning* of an experiment, we also simulated two-strains that grew at a *fixed* aspect ratio throughout the experiment. We have referred to this framework as “aspect ratio static” and our simulations are similar to those presented by Smith et al. [146]. In Figure 3.3 we show results from an initial seeding of cells where the aspect ratio

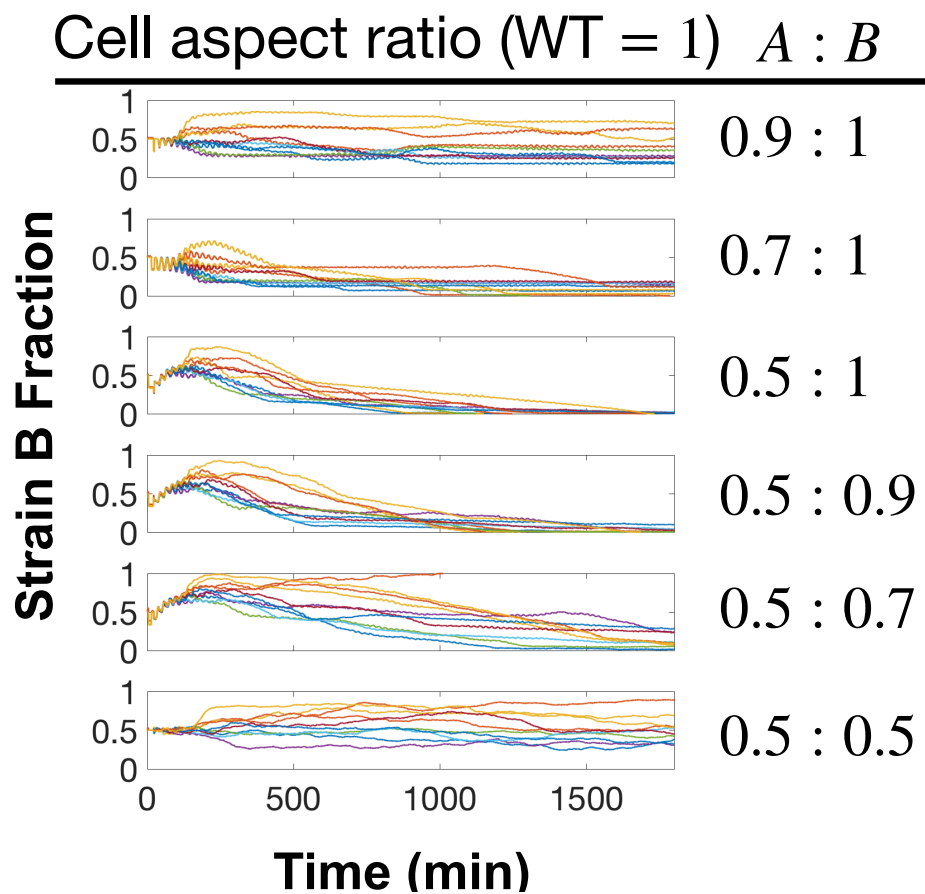


Figure 3.3: **Strain ratio dynamics vs. aspect ratio of both strains.** A 2-strain simulation using the ABM framework from Chapter 2. Five examples of an open-walled, $20 \times 100 \mu\text{m}$ trap show dynamical effects from an initial aspect ratio difference between the two strains. In contrast to Fig. 3.2, the aspect ratio change was present from initiation of the simulation. Each plot shows 10 iterations of 32 randomly-seeded initial cells randomly chosen of each strain. Decreasing aspect ratio showed marked increase of the rate of decimation of the larger strain. Y-axis of each plot represents fraction of strain B cells.

was fixed throughout the experiment. As can be seen from Figure 3.3, the larger the difference in aspect ratios between the strains, the higher the probability of extinction of the larger strain. Of the six simulations shown in Figure 3.3, the middle two (0.5 : 1 and 0.5 : 0.9) showed either complete extinction or a significant decimation of the smaller strain (strain ‘B’). Interestingly, in these simulations the initial strain B fraction increased from 0.5 at the beginning of the simulation. Because the traps are seeded with only a small number of cells (16 of each strain), the initial *trap-filling* phase evidently has different dynamics than those of a close-packed, full trap, as in Figure 3.2. We conjecture this is due to the *initial* establishment of columns, where on trap filling and establishment of full expansion flow, large patches of the smaller strain that are not centrally located will be flushed out by the cell flow. This is, however, at least partially due to our strain fraction being computed by *number* of cells and not by their *volume*: for the same amount of volume ejected from the trap, a smaller aspect ratio cell will have a larger ejected cell count, which can affect the strain fraction more strongly.

3.2.5 Aspect ratio control via cell-cell signaling

In this section, we present a simulation that demonstrated one strain *signaling* the other to change aspect ratio. We model our signaling architecture after quorum-sensing (QS) circuits that are used extensively in bacterial communication in synthetic biology [168, 13, 166]. For this purpose, we extended our simulation environment described in Chapter 2 to include a diffusion solver so that we could model production, diffusion, and reception of a QS molecule within our agent-based model.

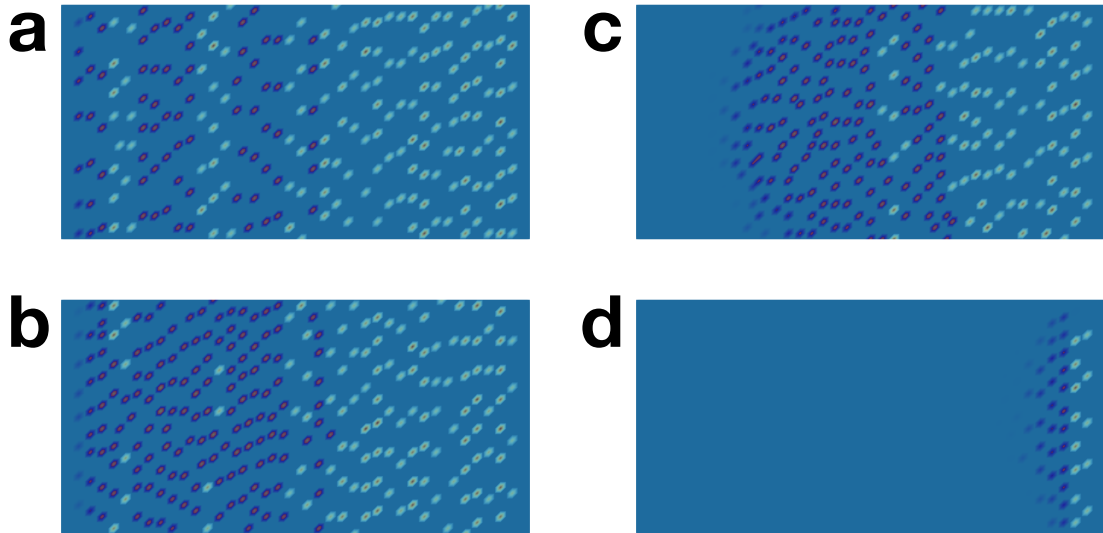


Figure 3.4: **Aspect ratio dynamic control via cell-cell signalling.** A sender-receiver simulation experiment demonstrated dynamic aspect ratio control. Two strains were grown in a $20 \times 40 \mu\text{m}$, two-walled microfluidic trap: The WT strain (the “sender,” white outline) produced an HSL that diffused out of the cell, through the trap and into the invading strain (the “receiver,” blue outline). Image “dots” recorded cell centers (cell outline not shown) and intra-cell HSL concentration of each strain. Upon induction, sufficient HSL signal in the invading strain activated transcription of a protein whose expression resulted in a decreased aspect ratio in the simulation model. Strength of the received HSL signal was indicated by amount of blue coloring in the invading strain. **(a)** Simulation time point where vertical stripes had stabilized and cell flow was vertically symmetric from the center of the trap. The strains were well-mixed and sufficient HSL signal reached all of the invading strain population. **(b)** Time point after induction. The invading strain with sufficient HSL concentration changed its aspect ratio dynamically and began stochastic invasion of the WT strain. On the left-hand side of the panel, mother-cell positions of the WT strain became occupied by the invading strain. Due to the ejection of the WT strain, HSL signal strength diminished (indicated by fading blue coloring) in the invading strain on the trailing-edge of the invasion. **(cd)** Invasion continued into the rightmost columns of WT strain. Invading cells’ HSL concentration was now diminished on the trailing edge: the dynamic aspect ratio change was switched off for these cells due to insufficient HSL signal to activate transcription of protein. Areas of background color only are occupied by “receiver” strain with aspect ratio the same as WT, (cells not shown).

We base our model on that presented by Chen et al. in [32] (Supplementary Information). We used a finite-element software known as *Fenics* to implement our diffusion solver (see also the use of this software in Chapter 4 for further details).

As mentioned at the beginning of the present Chapter, we shall omit details of the genetic construction of our model circuit and limit our model to that of a single protein, whose expression is proportional to the concentration of *received* QS signal from another strain (see also the sender-receiver architecture in Chapter 5 and [16]). In our simulation, we constructed a two-strain consortia where a wild-type (WT) strain remained at a constant aspect ratio but produced a signal that diffused to a receiver strain (that we will call the “invading strain”) whose aspect ratio was changed upon sufficient concentration of received signal from the WT strain. We outline the simulation experiment in Figure 3.4.

3.3 Discussion

Our results in Figure 3.2 are perhaps not surprising. A smaller aspect ratio cell has a higher percentage of its surface area composed of the cell *poles*, which are hemispherically shaped [29]; hence, these cells are able to rotate more freely and stochastically invade adjacent columns in a microfluidic trap experiment. However unsurprising its mechanism, the ability to alter strain ratio in experiments is of significant interest when one considers the difficulties of studying bacterial consortia as outlined above (see section 3.2.3). The ability to modulate strain ratio dynamically could allow an experimentalist, for example, to observe an initial strain ratio or strain

width distribution and make an adjustment to one (or both) of the populations by inducing a change in aspect ratio. As evidenced from the results of Figure 3.2 and the images of Figure 3.1, a bacterial cell strain population in a microfluidic trap can be readily decimated by a strain of reduced aspect ratio. Such a change in the population balance via dynamic gene expression can facilitate synthetic control over the composition of synthetic consortia and add to the expanding set of engineering tools necessary for further advancements in synthetic biology [22].

We have also shown that such dynamic control can be asserted *among* competing strains by illustrating a simulation experiment where one strain signaled another to induce a change of aspect ratio, which led to the eventual extinction of that strain. In the simulation of Figure 3.4, we also witnessed the creation of a negative-feedback loop in which the resulting decrease in strain population directly decreased the signal that induced the population change itself. This suggests that populations could be self-regulating, and extends the ideas of population control by strategies that use, for example, orthogonal quorum-sensing systems [22].

Population control should play an ever increasing role in synthetic biology contexts and we believe that mechanical interactions will continue to be a rich source of experimental investigation to further its advance.

Chapter 4

Continuum Modeling of Bacterial Growth

4.1 Introduction

Agent-based models provide many advantages in simulations of dynamical biological systems; however, there are also times when granular resolution of agents is simply not necessary or desired. A principal challenge to an ABM is the computation time required for tracking a large number of interacting agents. Although we have presented evidence of the continued expansion of both computing power and software for the simulation of biological systems (see Chapter 1), choosing the appropriate model and scale of simulation is always of concern, since any increase in simulation efficiency directly translates to the availability of extended parameter sweeps and more realistic simulations.

In this chapter, we present a different approach to modeling cell growth. Rather than modeling cells as individual *agents*, we will treat cells as a continuum of points using a partial differential equation (PDE). The growth model we present derives directly from that presented by Volfson et al. [165]. In their paper, they present a continuum approach for the growth of bacterial cells that uses modified fluid dynamics equations with cell ordering governed by liquid-crystal dynamics theory. They present experimental data and both a continuum and agent-based model to describe emergent cell ordering in a confined, growing 2D population of bacteria. In their continuum model, however, the dynamical equations are reduced to a 1D system and several ad-hoc assumptions are made for further simplification. Their model was used in subsequent publications (Boyer et al. [23], and Mather et al. [104]), but no significant extensions to the theory were presented in these papers.

The stated purpose for their study is “to elucidate the mechanism of cell ordering and quantify the relationship between the dynamics of cell proliferation and the spatial structure of the population” [165]. In their paper, Volfson et al. compare experimental evidence of this ordering with the results of their agent-based model (ABM) and continuum model. The principal conclusion of the paper is that “...ordering of cells is mediated by the expansion flow generated by cellular growth” [165]. That is, the phenomena of *nematic ordering*, (meaning here the 2D alignment of rod-shaped bacteria in a microfluidic trap) is driven by the volume expansion of cell growth. In the conclusion of [165], Volfson et al. note that nematic ordering of growing bacterial cells is in contrast to that of liquid crystals, polymers, and vibrated granular rods, where the latter are ordered primarily by the combination of steric

and thermodynamic effects [165].

We have found the dynamical equations presented by Volfson et al. to be very valuable to begin a study of a continuous (PDE-based) bacterial cell growth model. Specifically, the model introduces PDE for:

- the treatment of a 2D colony of growing bacterial cells as an expanding *cell fluid*, and
- ordering dynamics based on dynamical equations of liquid crystal theory.

Although these PDE are presented by Volfson et al. (in the Supporting Information of [165]) in full 3D generality, the equations are reduced in the main text to a one-dimensional system that, although appropriate for the two-walled microfluidic traps in their study, does not elucidate more complicated behaviors of cells in more general microfluidic trap geometries.

In this chapter, we will consider the cell growth PDE model presented by Volfson et al. with some re-derivations of the equations for use in two dimensions. We will also perform simulations that use the full 2D system. We consider our presentation in this chapter to be a significant extension to the model as presented in [165].

Specifically, in this chapter, we present extensions to the Volfson et al. PDE that comprise:

1. restructuring the *cell fluid* equation into a Poisson's equation PDE for the "cell pressure,"

2. use of the liquid crystal theory for full 2D dynamics, and
3. simulations of the 2D system using an open-source finite element solver.

We will begin by summarizing the continuum model as presented by Volfson et al. in [165]. We will then introduce the model extensions and present 2D simulation results of the extended model.

4.2 Mathematical model

4.2.1 Cell fluid model of Volfson et al.

4.2.1.1 Overview

Volfson et al. [165] present a continuum “cell fluid” model that is derived from a mass conservation equation, Newton’s second law, and theory borrowed from liquid crystal dynamics. They establish a core set of vector equations to model cell growth and nematic ordering in a microfluidic trap. Specifically, the PDE are a model for the spatiotemporal evolution of:

ρ : a normalized, coarse-grained cell density that represents the degree of close-packing of cells in a microfluidic trap (with $\rho \in [0, 1]$),

\mathbf{Q} : a tensor order parameter that measures both a local average cell angle (a unit vector known as the *director*, \mathbf{n}) and a degree of uniformity (distribution)

of cell angles locally about this average (which we will notate q or q -scalar, with $q \in [0, 1]$), and

\mathbf{v} : the cell velocity measured in the laboratory frame.

The PDE are presented by Volfson et al. in [165] in a one-dimensional reduction, which we detail in the following section.

4.2.1.2 1D dynamical equations

We now describe the 1D dynamical equations of motion and ordering as presented by Volfson et al. in [165]. The definitions of the 1D equations' scalar parameters and variables are:

ρ : cell density

v : cell velocity

α : cell growth rate

q : q -scalar order parameter

B : a kinetic constant for cell ordering

p : the cell pressure, where $p \propto \exp[s(\rho - \rho_c)]$, s is a scalar rate, and ρ_c is a critical packing density

μ : velocity-based damping parameter

In the 1D equations, spatial derivatives are taken with respect to the z-axis, which in their presentation is the long axis of a two-walled, 2D microfluidic trap (i.e., the long walls are oriented parallel to the z axis). Thus, their equations are a reduced 1D system that uses the z-axis as the single dimension.

The reduced equations are [165]:

$$\partial_t \rho + \partial_z(\rho v) = \alpha \rho, \quad (4.1)$$

$$\partial_t q + v \partial_z q = B(1 - q^2) \partial_z v, \quad (4.2)$$

$$\partial_t(\rho v) + v \partial_z(\rho v) = -\partial_z p - \mu \rho v. \quad (4.3)$$

Eq. 4.1 is a continuity equation for mass with exponential growth of cell mass at rate α (the growth rate of the cell). Eq. 4.2 is the evolution equation for the q-order parameter (here a scalar), where B is a kinetic constant and the factor $(1 - q^2)$ is a heuristic to uphold the condition that $q \leq 1$. Eq. 4.3 is the equation for momentum balance (derived from Newton's second law) whose right-hand side consists of a term for the spatial derivative of the pressure, and a term for velocity-based friction force (damping constant μ , scaled by the cell density ρ).

The equations 4.1 – 4.3 are further reduced in [165] to a set of three ordinary differential equations (ODE) for the amplitudes of ρ , q , and the velocity gradient $\partial_z v$, where ρ and q are assumed spatially invariant. The equations are simulated in 1D and compared with data from an agent-based model, with which, they claim, their continuum model shows suitable agreement. This is the extent of the continuum results in their paper.

4.2.1.3 Discussion

Although Eqs. 4.1 – 4.3 have provided valuable insights into modeling the dynamics of bacterial populations, they have certain shortcomings. Specifically:

1. The pressure p is modeled by an additional, ad hoc equation that is an exponential function of the difference between the density ρ , and a critical packing density ρ_c :

$$p \propto \exp[s(\rho - \rho_c)].$$

If the rate s is “large” (as they claim for this equation), then the pressure is exponentially small (large) when $\rho < \rho_c$ ($\rho > \rho_c$), respectively. We find that this ad hoc equation is too simplified: it fails to capture pressure dynamics from the equation 4.3 and results in unrealistically large pressures if $\rho > \rho_c$. Further, a pressure gradient can (and does) exist even if cell density is spatially uniform, and this effect cannot be captured by this equation.

2. The scaling of the order parameter q by the term ad hoc term $(1 - q^2)$ keeps $q \leq 1$, but we find this term unnecessary if the simulations include a noise term.

In our simulations, we will show that a phenomenological noise term added to the cell director \mathbf{n} keeps q bounded without adding a heuristic penalty term to the rate equation. In our model, pressure will be a fundamental variable in our PDE formulation of continuum cell dynamics. Further, we will show that cell density is not the primary driver of ordering dynamics in a 2D microfluidic trap. Rather, it is

the spatial velocity gradient of cells that drives nematic ordering. Cell velocity, as we will show, is itself driven by a pressure gradient, and we believe that modeling pressure directly through the PDE formulation provides the necessary coupling of cell growth, cell pressure, and cell ordering to properly explain and predict the dynamics of bacterial cells in a microfluidic trap. We now derive our extension of the Volfson et al. 1D model to a system of coupled 2D vector equations.

4.2.2 Re-derivation of the cell fluid model

4.2.2.1 Overview

We begin by re-deriving the equations of motion for cell growth and ordering from first principles. For simplification, we will not consider the spatiotemporal evolution of the cell density ρ . We justify this for the following reasons:

1. Considering transport of a spatially expanding colony of cells complicates the equations without elucidating the complicated behavior that can occur at a growth front [48, 49]. In particular, advecting growth fronts would require advection of the resulting spatially discontinuous fields of density, pressure and velocity, which is numerically challenging.
2. Ordering dynamics due to trap-filling are transient, and although cell seeding distribution can affect initial strain ratios (see Chapter 3), experimental data with respect to cell ordering and transport is dominated by full-trap dynamics.

3. This simplification allows a firm foundation from which to build more complicated models.

Also, as was done in Chapter 2, we will ignore inertial effects in the momentum balance equations. This simplification is justified by the large separation of time scales between inertial acceleration and cell growth rate, as detailed in Appendix A.1.

4.2.2.2 Momentum balance

The following is the initial vector equation for momentum balance (the vector form of Eq. 4.3, as presented in [165]):

$$\partial_t(\rho\mathbf{v}) + \mathbf{v} \cdot \nabla(\rho\mathbf{v}) = -\nabla p - \mu\rho\mathbf{v}. \quad (4.4)$$

This equation is Newton's second law, where the left-hand side is the total derivative of momentum density, and the right-hand side is a sum of two force density terms: the pressure gradient and the damping force. By zeroing the inertial terms, we eliminate the left-hand side and then have:

$$\nabla p = -\mu\rho\mathbf{v}. \quad (4.5)$$

We recall $\rho \in [0, 1]$ is a quantity reflecting the normalized density of the cell fluid. As mentioned above, we will ignore the evolution of cell density and set $\rho = 1$ throughout. This differs from the model presented by Volfson et al. [165], where ρ evolves temporally (but is set uniform spatially). We find that a spatial evolution of ρ would be prohibitive, and that temporal evolution is only transient and

uninformative, as mentioned above. By setting $\rho = 1$, Eq. 4.5, upon rearrangement, then becomes:

$$\mathbf{v} = -\mu^{-1}\nabla p. \quad (4.6)$$

This equation provides, upon generation of a pressure solution p , the direct computation of the resulting velocity field and will be referred to in the sequel.

4.2.2.3 Cell density continuity equation

We next consider the vector equation for Eq. 4.1, which is a continuity equation for cell density [165]:

$$\partial_t \rho + \nabla \cdot (\rho \mathbf{v}) = \alpha \rho. \quad (4.7)$$

Under our assumption that cell density is spatiotemporally invariant (with $\rho = 1$), this equation reduces to a “modified incompressibility condition” given by:

$$\nabla \cdot \mathbf{v} = \alpha. \quad (4.8)$$

(The quotation marks above are used since this equation accounts for the exponential *growth* of cell mass and is not a term for the *compressibility* of cells). Under an assumption of uniform cell density, cell velocity must diverge at the growth rate since the continuous creation of cell mass due to growth requires continuous transport of the mass outward from every point and at a rate equal to that at which it is created. We note that Eq. 4.8 is also presented in Mather et al. [104] and Boyer et al. [23].

With the simplification that $\rho = 1$, we differ from the model presented in [165] by forcing 4.8 from the onset of all dynamics. We justify this simplification by assuming

a “full trap” scenario and that cell growth rate is uniform spatially. In fact, by re-introducing ρ into our equations, we can recover cell density evolution if desired, but this does not affect the results presented here. Because we are assuming spatially homogeneous density, temporal changes in ρ will uniformly affect dynamics, which will only affect quantitative (rate) behavior and not qualitative behavior.

Now, under the assumptions noted, and by rearranging 4.6 and using 4.8, we generate the key equation for cell growth with our continuum model:

$$\nabla \cdot \nabla p = -\mu\alpha, \tag{4.9}$$

which is Poisson’s equation for the cell pressure. Further, if we have a solution for the pressure p with this equation, we then readily compute the vector velocity field using 4.6.

These equations are extremely simple to formulate; however, they lead to immediate results to describe steady-state pressure and velocity fields when considering an open-walled microfluidic trap, for example, as we will see in the results section below. We note, importantly, that cell growth in these equations is *isotropic*: there is no concept of cell angle or directed axial growth along this angle. The only requirement with respect to growth, namely, Eq. 4.8, is that the divergence of the velocity equals α , irrespective of the direction of \mathbf{v} . Thus, the 2D spatial solution of this equation will be governed primarily by the boundary conditions. However, we will see in the next section that we can still describe the dynamics of cell *ordering*, which implicitly measures the angle of a local region of cells.

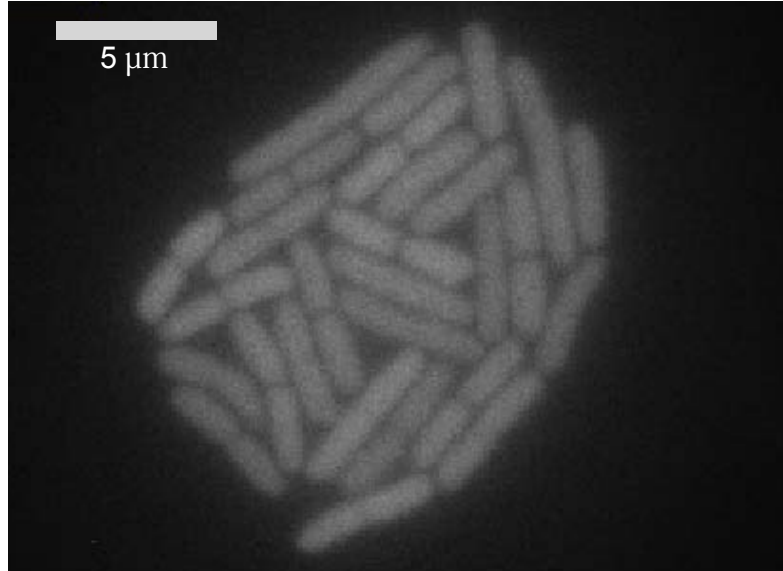


Figure 4.1: **A small bacterial cell colony.** A mesoscopic scale of cells in our model is ≈ 10 's of cells. Unpublished image courtesy of the Bennett Lab, Rice University.

4.2.2.4 Discussion

The continuum model we present in this Chapter relies on a *mesoscopic scale* suitable for a cell dynamics description that is neither too fine nor too coarse. Specifically, we do not consider a resolution of our continuum model at the *individual* cell level; rather, we consider a mesoscopic scale, which can be thought of as on the order of 10's of cells (see Figure 4.1). Likewise, we do not zoom-out so far that we lose the description of behavior on the scale of the geometry of the microfluidic traps used in experiments ($\approx 10^3 - 10^4$ cells). At our intermediate, mesoscopic scale, we let growth be isotropic while still considering the director \mathbf{n} to evolve using Q-tensor theory, as we will show below.

In this sense, our model is partially incomplete, as it does not address an axial

growth direction. Yet, it models the spatiotemporal evolution of an angle order parameter (q-scalar) and director \mathbf{n} . We can (perhaps, in a more advanced theory) consider anisotropic growth using a growth tensor that helps direct “anisotropic pressure diffusion” in a favored direction. Anisotropic diffusion is a technique used in such fields as image processing [109] and MRI analysis [116]. Although we have considered such complexity in our model, we reserve this advanced development for future work.

The Poisson’s equation for the pressure (Eq. 4.9) can easily be solved using readily available PDE software. We have implemented this equation and system using the finite-element PDE software toolkit *Fenics* [8, 97, 98, 99]. Results from simulations of these equations are given in section 4.3, below. To close our system of equations, however, we must present the third dynamical equation: that of Q-tensor dynamics theory.

In the next section, we will give an overview of liquid crystals, and detail the structure and use of the Q-tensor for the special case of a 2D geometry. We will then describe the equations of “nemato-hydrodynamics” that we use with the Q-tensor theory to describe ordering of close-packed colonies of bacterial cells in a microfluidic trap.

4.2.3 Liquid crystals and Q-tensor structure

4.2.3.1 Overview of liquid crystals

Q-tensor theory is used to describe what are known as liquid crystal *nematogens*, which are a phase of liquid crystals typically characterized by the alignment of elongated, anisotropic entities [39]. Liquid crystals are an intermediate phase of matter (a ‘mesomorphic phase’) where order exists not in the center-of-gravity of the constituents (as in a solid lattice), but rather, only in their *orientation*. In order for orientation of an entity in a liquid crystal to be well-defined, it must have a non-isotropic geometry, and examples include polymer molecules, organic cholesterol esters, the tobacco mosaic virus, and bacteria [39, 170] .

The transition from a disordered to ordered state of the liquid crystal is a phase transition that is a function of the temperature in *thermotropic* liquid crystals, or the concentration in *lyotropic* liquid crystals. The spatial scale of the constituents of the liquid crystal are typically on the order of nanometers (molecular scale), and thermal energy is a significant contributor to the motion and alignment of a liquid crystal composed of these entities. In our study, we consider motion and alignment of bacterial cells on the spatial scale of microns; hence, thermodynamic effects will be ignored. This simplification is also done in the model presented by Volfson et al. [165], although the equations are there initially presented in their full generality, as given in Olmsted and Goldbart [117].

4.2.3.2 Q-tensor description

The Q-tensor is a symmetric, traceless tensor by definition and is meant to capture both an average *direction* and *distribution* of cell angles of liquid crystal nematogens on a mesoscopic scale (mesoscopic scale is of course, context dependent). The average direction is specified by a unit vector \mathbf{n} , which is known as the *director*, and the degree of ordering is specified by a scalar parameter that we will notate as q , or for clarity, ‘ q -scalar’ (to distinguish from the tensor \mathbf{Q} and from Q , the principal eigenvalue of \mathbf{Q} , as defined below).

As the notation can be confusing, we gather the conventions we use in our presentation with a short description of each variable:

1. \mathbf{Q} : in boldface, \mathbf{Q} refers to Q-tensor, which is a rank-two tensor in two dimensions in our usage. The use of boldface \mathbf{Q} marks this variable as a tensor without qualification, whereas in non-boldface, we qualify this variable as ‘Q-tensor.’ \mathbf{Q} is a symmetric, traceless tensor, which constrains its structure such that (in two dimensions) it has only two degrees of freedom: the unit vector director \mathbf{n} , and the scalar order parameter q . However, the entries of \mathbf{Q} are not these quantities explicitly. We will show, below, how to extract these parameters given \mathbf{Q} , and also how to construct \mathbf{Q} from them. In both cases, the transformations are unique.
2. Q : in plain-text font (and without qualification), Q refers to the *principal eigenvalue* of \mathbf{Q} .

3. q : lower-case and non-boldface, q is ‘ q -scalar’ and we will use both terms interchangeably. For our usage, this term represents a local degree of nematic ordering of bacterial cells. We note that $q \in [0, 1]$: $q = 0$ represents an isotropic state (complete disorder of orientation), and $q = 1$ represents perfect ordering of cells (all cells point in the direction \mathbf{n}). We will also show below that $q = 2Q$.

The traceless structure of the \mathbf{Q} -tensor ensures that $q = 0$ in an isotropic state, as we will also show below. Because we are studying bacterial cells growing in quasi two-dimensional traps, we will only describe the structure of the \mathbf{Q} -tensor in two dimensions, although the theory is presented most generally in three dimensions [28, 39, 117].

We note that, under the assumption that nematogens are symmetric along their long axis (which we assume true for bacterial cells as in our ABM in Chapter 2), the \mathbf{Q} -tensor must be of even symmetry with respect to \mathbf{n} [5]. That is,

$$\mathbf{Q}(\mathbf{n}, q) = \mathbf{Q}(-\mathbf{n}, q) \quad \forall q \in [0, 1].$$

This in fact motivates the use of a second-rank tensor order parameter, because a vector order parameter is insufficient to capture this required property [28].

4.2.3.3 \mathbf{Q} -tensor definition

In two dimensions, let us consider a mesoscopic scale of bacterial cells and notate an individual cell’s axial direction by a two-component unit vector with components (u_x, u_y) . We will then notate the mesoscopic average direction by $\mathbf{n} = \langle u_x, u_y \rangle$. The

component definition Q_{ij} (with $i, j \in \{x, y\}$) of the Q-tensor is then:

$$\mathbf{Q} = Q_{ij} := \langle u_i u_j - \frac{1}{2} \delta_{ij} \rangle, \quad (4.10)$$

where δ_{ij} is the Kroneker delta with $\delta_{ij} = 1$ iff $i = j$ and 0 otherwise, and $\langle \cdot \rangle$ represents spatial averaging on a mesoscopic scale [165, 28, 117, 42].

Example 4.2.1. As a simple example, consider perfect ordering of cells ($q = 1$) in the direction $\mathbf{n} = (1, 0)$. The Q-tensor is then:

$$\mathbf{Q} = \begin{pmatrix} \frac{1}{2} & 0 \\ 0 & -\frac{1}{2} \end{pmatrix} = \frac{q}{2} \begin{pmatrix} 1 & 0 \\ 0 & -1 \end{pmatrix} = \frac{q}{2} \begin{pmatrix} \cos(2\theta) & \sin(2\theta) \\ \sin(2\theta) & -\cos(2\theta) \end{pmatrix}, \quad (4.11)$$

where we have shown in the right two equalities alternate structures of \mathbf{Q} (see Proposition 4.2.3, below), and where $\theta_{\mathbf{n}} = 0$ is the angle argument of $\mathbf{n} = (1, 0)$. \square

Example 4.2.2. Consider an equal distribution of director angles $\theta_{\mathbf{n}} \in [0, \pi]$, which represents a purely isotropic state of the director \mathbf{n} . We compute Q-tensor using Eq. 4.10 and set $(u_i, u_j) = (\cos(\theta_{\mathbf{n}}), \sin(\theta_{\mathbf{n}}))$. By even symmetry of $\cos(\theta)$ across $\theta = \frac{\pi}{2}$, we have $\langle u_x u_y \rangle = \langle u_y u_x \rangle = 0$. Computing $\langle u_x u_x \rangle$,

$$\langle u_x u_x \rangle = \frac{1}{\pi} \int_0^\pi \cos^2(\theta) d\theta = \frac{1}{\pi} \cdot \left(\frac{\pi}{2} \right) = \frac{1}{2}.$$

Similarly, $\langle u_y u_y \rangle = \frac{1}{2}$. From Eq. 4.10 the result $\mathbf{Q} = 0$ follows. Thus, $q = 0$ in an isotropic distribution of the director \mathbf{n} , which represents complete disorder of orientation. \square

In order to work with the tensor \mathbf{Q} , we must specify how to *generate* \mathbf{Q} given \mathbf{n} and q-scalar. If one were given the positions and angles of an ensemble of nematogens, one could readily compute \mathbf{Q} from 4.10 (one must also define the spatial region

over which to average and a suitable probability measure). Similarly, one could compute these quantities from a probability distribution of the cell angles in the spatial region of interest. However, we require a means to directly assemble \mathbf{Q} and also extract \mathbf{n} and q -scalar if given \mathbf{Q} . Volfson et al. give a second definition for \mathbf{Q} that clarifies this construction:

$$\mathbf{Q} = Q_{ij} := 2Q(n_i n_j - \frac{1}{2}\delta_{ij}), \quad (4.12)$$

where $n_{i,j}$ are the components of \mathbf{n} and Q is the principal eigenvalue of \mathbf{Q} [165]. We note that, in the Volfson et al. paper (Supporting Information), they confusingly call Q the scalar order parameter; in fact, it is one-half this quantity, as we will show below.

Proposition 4.2.3. *The following results hold:*

a) \mathbf{Q} is traceless and symmetric for all $q \in [0, 1]$ and all directors \mathbf{n} in the circle group \mathbf{T} .

b) \mathbf{Q} can be diagonalized by a rotation matrix R_ϕ , where ϕ is the angle of rotation. More precisely, $\exists \phi \in [0, \pi]$ s.t. $R_\phi \mathbf{Q} = \mathbf{D}$, where \mathbf{D} is a diagonal matrix.

c) The structure of \mathbf{Q} is equivalent to: $Q \begin{pmatrix} \cos(2\theta) & \sin(2\theta) \\ \sin(2\theta) & -\cos(2\theta) \end{pmatrix}$, where $Q \in [0, \frac{1}{2}]$ is the principal eigenvalue of \mathbf{Q} , $2Q = q$ -scalar, and θ is the angle of the director \mathbf{n} .

d) The principal eigenvector of \mathbf{Q} is \mathbf{n} , and the principal eigenvalue is:

$$Q = \sqrt{Q_{xx}^2 + Q_{xy}^2} = \sqrt{Q_{yy}^2 + Q_{yx}^2}$$

. The two eigenvalues of \mathbf{Q} are equal and opposite.

Proof.

a) From Eq. 4.12, we have:

$$\text{trace}(\mathbf{Q}) = 2Q(n_x^2 + n_y^2 - 1).$$

Because \mathbf{n} is a unit vector, $\text{trace}(\mathbf{Q}) = 0$ for all $q = 2Q$ (see item *c*) below). Because $n_x n_y = n_y n_x$, \mathbf{Q} is symmetric, and the claim follows.

b) Consider the product of a rotation matrix (with rotation angle ϕ) with \mathbf{Q} , using the structure for \mathbf{Q} proved in *c*), below:

$$R_\phi \mathbf{Q} = Q \begin{pmatrix} \cos(\phi) & -\sin(\phi) \\ \sin(\phi) & \cos(\phi) \end{pmatrix} \begin{pmatrix} \cos(2\theta) & \sin(2\theta) \\ \sin(2\theta) & -\cos(2\theta) \end{pmatrix}.$$

Then, in order to have the off-diagonal entries of this matrix product be zero, we require:

i) $Q(\cos(\phi) \sin(2\theta) + \sin(\phi) \cos(2\theta)) = 0$, and

ii) $Q(\sin(\phi) \cos(2\theta) + \cos(\phi) \sin(2\theta)) = 0$

for the upper-right and lower-left off-diagonal entries, respectively. These two conditions are equivalent, and employing the double-angle identity

$$\sin(x + y) = \sin(x) \cos(y) + \cos(x) \sin(y)$$

with *ii*), we reduce the requirement to:

$$\sin(\phi + 2\theta) = 0,$$

which is satisfied by $\phi = n\pi - 2\theta$, $n = 0, 1, 2, \dots$. We choose the smallest n such that ϕ is positive, which then gives $\phi \in [0, \pi]$. Thus, \mathbf{Q} can be diagonalized by rotation, as claimed.

c) From the definition of \mathbf{Q} in 4.10, let $q = 1$, $\mathbf{n} = \langle u_x, u_y \rangle = (\cos(\theta), \sin(\theta))$, where θ is the angle-direction of \mathbf{n} , and brackets represent the same mesoscopic-scale averaging as in the definition. Then:

$$\mathbf{Q} = \begin{pmatrix} \cos^2(\theta) - \frac{1}{2} & \cos(\theta) \sin(\theta) \\ \cos(\theta) \sin(\theta) & \sin^2(\theta) - \frac{1}{2} \end{pmatrix}.$$

By using the identities:

$$\sin(2\theta) = 2 \sin(\theta) \cos(\theta),$$

$$\cos(2\theta) = 2 \cos^2(\theta) - 1, \text{ and}$$

$$-\cos(2\theta) = 2 \sin^2(\theta) - 1,$$

we then have:

$$\mathbf{Q} = \frac{1}{2} \begin{pmatrix} \cos(2\theta) & \sin(2\theta) \\ \sin(2\theta) & -\cos(2\theta) \end{pmatrix}.$$

Because q -scalar was set to one, and by the definition of \mathbf{Q} in 4.12, we see that $q = 2Q$. The general case for $q \in [0, 1]$ follows by linearity and the definition in Eq. 4.12. Thus:

$$\mathbf{Q} = \frac{q}{2} \begin{pmatrix} \cos(2\theta) & \sin(2\theta) \\ \sin(2\theta) & -\cos(2\theta) \end{pmatrix}. \quad (4.13)$$

d) Consider the product of \mathbf{Q} (using 4.12) and \mathbf{n} :

$$\begin{aligned}
\mathbf{Q}\mathbf{n} &= 2Q \begin{pmatrix} n_x^2 - \frac{1}{2} & n_x n_y \\ n_x n_y & n_y^2 - \frac{1}{2} \end{pmatrix} \begin{pmatrix} n_x \\ n_y \end{pmatrix} \\
&= 2Q \begin{pmatrix} n_x^3 - \frac{n_x}{2} + n_x n_y^2 \\ n_x^2 n_y + n_y^3 - \frac{n_y}{2} \end{pmatrix} \\
&= 2Q \left(n_x^2 + n_y^2 - \frac{1}{2} \right) \begin{pmatrix} n_x \\ n_y \end{pmatrix} \\
&= Q \begin{pmatrix} n_x \\ n_y \end{pmatrix}.
\end{aligned}$$

The last equality follows since \mathbf{n} is a unit vector. As per the definition in Eq. 4.12, Q is the principal eigenvalue of \mathbf{Q} ; thus, \mathbf{n} is the principal eigenvector. Now, again using Eq. 4.12, we have

$$\begin{aligned}
\sqrt{Q_{xx}^2 + Q_{xy}^2} &= 2Q \left[\left(n_x^2 - \frac{1}{2} \right)^2 + (n_x n_y)^2 \right]^{\frac{1}{2}} \\
&= 2Q \left[n_x^4 - n_x^2 + \frac{1}{4} + n_x^2 n_y^2 \right]^{\frac{1}{2}} \\
&= 2Q \left[n^2 (n_x^2 + n_y^2 - 1) + \frac{1}{4} \right]^{\frac{1}{2}} \\
&= Q,
\end{aligned}$$

where the last equality follows again since \mathbf{n} is a unit vector. Substituting Q_{yy}^2 for Q_{xx}^2 , we obtain the same result. Now, from a), \mathbf{Q} is symmetric; thus, its eigenvectors

are orthogonal. Computing the matrix-vector product $\mathbf{Q}\mathbf{n}_\perp$, we have

$$\begin{aligned}
\mathbf{Q}\mathbf{n}_\perp &= 2Q \begin{pmatrix} n_x^2 - \frac{1}{2} & n_x n_y \\ n_x n_y & n_y^2 - \frac{1}{2} \end{pmatrix} \begin{pmatrix} -n_y \\ n_x \end{pmatrix} \\
&= 2Q \begin{pmatrix} -n_x^2 n_y + \frac{n_y}{2} + n_x^2 n_y \\ -n_x n_y^2 + n_x n_y^2 - \frac{n_x}{2} \end{pmatrix} \\
&= 2Q \left(\frac{1}{2}\right) \begin{pmatrix} n_y \\ -n_x \end{pmatrix} \\
&= -Q \begin{pmatrix} -n_y \\ n_x \end{pmatrix}.
\end{aligned}$$

The two eigenvalues of \mathbf{Q} are then equal and opposite, as claimed.

□

We consider Eq. 4.13 to be an intuitive definition of \mathbf{Q} that directly extracts both \mathbf{n} and q , and clearly shows the π -symmetry of the director with respect to \mathbf{Q} , i.e., that $\mathbf{Q}(\mathbf{n}, q) = \mathbf{Q}(-\mathbf{n}, q)$.

4.2.3.4 \mathbf{Q} -Tensor nematodynamics

We now describe the dynamical equation of \mathbf{Q} , the tensor order parameter of liquid crystal theory, which is used to describe ordering of bacterial cell “nematogens.” The equation of nematodynamics presented by Volfson et al. is derived from Olmsted & Goldbart in [117]. The vector form of the reduced (neglecting thermodynamic effects), governing equation for \mathbf{Q} is given in component form [165] as:

$$\partial_t Q_{ij} + \mathbf{v} \cdot \nabla Q_{ij} = \beta \kappa_{ij}^{(s)}, \quad (4.16)$$

where β is a kinetic parameter, and $\kappa^{(s)}$ is the symmetric, traceless part of the strain-rate tensor $\nabla\mathbf{v}$. The left-hand side of Eq. 4.16 is the total derivative of the component Q_{ij} and the right-hand side is the forcing term that depends on the symmetric, deviatoric spatial gradient of the cell velocity. In our model, we use the velocity solution (computed from Poisson's equation for the pressure, i.e., Eq. 4.6 following 4.9) for the transport velocity \mathbf{v} on the left-hand side, and we compute the tensor $\nabla\mathbf{v}$ (which is then converted to a traceless, symmetric tensor) on the right-hand side of this transport equation.

This governing equation for \mathbf{Q} dictates that increased ordering results from the *non-isotropic* part of the strain-rate tensor. We recall that a symmetric tensor (or matrix) can be separated into an isotropic part, and a non-isotropic or *deviatoric* part. The isotropic part represents uniform expansion (or contraction) in all dimensions of the tensor; however, the deviatoric part represents an anisotropic shear. We find it intuitive that an isotropic expansion of the velocity gradient tensor should *not* influence ordering dynamics, since rotation of the director \mathbf{n} of a nematogen requires a shear-type force (i.e., a purely isotropic velocity gradient cannot rotate a cell). Indeed, Eq. 4.16 comes from [117], which is a study of shear flow effects of the isotropic-nematic transition of liquid crystals. Wegner et al. [170] also study the effects of shear on elongated cylinder dynamics.

We conclude this section with a necessary and sufficient condition for a locally spatially invariant q -scalar to increase with respect to the principal eigenvector direction of the symmetric, traceless strain-rate tensor $\kappa^{(s)}$. We also claim that the director \mathbf{n} will rotate towards this eigenvector direction unless these two vectors are

orthogonal or parallel.

Proposition 4.2.4. *Let $\nabla \mathbf{Q} = 0$ in Eq. 4.16 (i.e., let \mathbf{Q} be spatially uniform in a local region), and let \mathbf{e}_k be the principal eigenvector of $\kappa \neq 0$. Then:*

a) *q -scalar increases iff the director \mathbf{n} points within $\pm \frac{\pi}{4}$ of \mathbf{e}_k ,*

b) *if $\mathbf{n} \cdot \mathbf{e}_k \neq 0$ and $\mathbf{n} \neq \mathbf{e}_k$, \mathbf{n} rotates towards \mathbf{e}_k .*

Proof. Recall the total derivative of \mathbf{Q} , per Eq. 4.16, is proportional to $\kappa^{(s)}$, the symmetric, traceless strain-rate tensor. Let an initial state of \mathbf{Q} be $\mathbf{Q}^{(0)}$, and by assumption let $\mathbf{Q}^{(0)}$ be spatially invariant. Then Eq. 4.16 becomes:

$$\partial_t Q_{ij}^{(0)} + \mathbf{v} \cdot \mathbf{0} = \beta \kappa_{ij}^{(s)}.$$

From part b) of Proposition 4.2.3, we rotate our reference frame such that $\mathbf{Q}^{(0)}$ is diagonal, with a positive entry a in the (1, 1) position of the tensor. Then, without loss of generality, the director angle in our new frame of reference is 0 by Proposition 4.2.3 c), and $a = \frac{q}{2}$. We define $\mathbf{Q}_D^{(0)}$ to be the resulting diagonal tensor. That is,

$$\mathbf{Q}_D^{(0)} = \begin{pmatrix} a & 0 \\ 0 & -a \end{pmatrix},$$

where $a \leq \frac{1}{2}$ is equal to one-half q -scalar at this initial time.

Now, we consider the most general form of a 2D symmetric, traceless tensor (in our new, rotated frame of reference), and let κ be

$$\kappa = \begin{pmatrix} k_1 & k_2 \\ k_2 & -k_1 \end{pmatrix} = k \begin{pmatrix} \cos(2\phi) & \sin(2\phi) \\ \sin(2\phi) & -\cos(2\phi) \end{pmatrix},$$

where the latter equality follows trivially from Proposition 4.2.3 c), $k > 0$, and ϕ is the principal eigenvector direction of κ (i.e., $\phi = \arg_{\theta} \mathbf{e}_k$). By our frame of reference rotation (i.e., because $\arg_{\theta} \mathbf{n} = 0$), ϕ represents the difference in angle between \mathbf{n} and the principal eigenvector direction of $\kappa^{(s)}$; thus, the proposition holds iff $|\phi| < \frac{\pi}{4}$.

Now, let $\mathbf{Q}_{\mathbf{D}}^{(0)}$ evolve for an infinitesimal time dt under Eq. 4.16, and let the resulting Q-tensor be

$$\mathbf{Q}' = \begin{pmatrix} a' & b \\ b & -a' \end{pmatrix} = Q' \begin{pmatrix} \cos(2d\theta) & \sin(2d\theta) \\ \sin(2d\theta) & -\cos(2d\theta) \end{pmatrix},$$

where: $d\theta$ is the resulting angle of the director in \mathbf{Q}' , we have used Proposition 4.2.3 c) to form the second equality, and $Q' > 0$ is the resulting principal eigenvalue of \mathbf{Q}' .

We now consider the two independent components of \mathbf{Q}' . Under our assumption of a spatially invariant $\mathbf{Q}_{\mathbf{D}}^{(0)}$, and for an infinitesimal time dt , Eq. 4.16 gives:

$$a' - a = dt \cdot \beta k_1$$

$$b = dt \cdot \beta k_2.$$

Now, from part c) of Proposition 4.2.3, we have:

$$q \nearrow \iff Q \nearrow.$$

Let $Q_0 = a$ be the principal eigenvalue of $\mathbf{Q}_{\mathbf{D}}^{(0)}$, and $Q' = \sqrt{(a')^2 + b^2}$, the resulting eigenvalue after time dt (using Proposition 4.2.3 d)). Then

$$q \nearrow \iff Q' > Q \iff (Q')^2 > Q^2 \iff (Q')^2 - Q^2 > 0.$$

Now, from the definition of the eigenvalue Q' , the definition of \mathbf{Q}' , and the immediately preceding centered equalities above, we have:

$$\begin{aligned} (Q')^2 - Q^2 &= [(a')^2 + b^2] - a^2 \\ &= [(a + dt\beta k_1)^2 + (dt\beta k_2)^2] - a^2 \\ &= 2dta\beta k_1 + O(dt^2). \end{aligned}$$

Omitting terms of order dt^2 , and since all of $dt, a, \beta, k > 0$ by definition or assumption, we have:

$$q \nearrow \iff k_1 > 0 \iff k \cos(2\phi) > 0 \iff |\phi| < \frac{\pi}{4}.$$

This proves the first claim. Now, without loss of generality, and by using the same definition for ϕ as above, let us assume $0 < \phi < \frac{\pi}{2}$. Then, from the definition of $d\theta$ above, \mathbf{n} rotates towards \mathbf{e}_k iff $d\theta$ has rotated towards ϕ , i.e., iff $d\theta > 0$ by our assumption of ϕ . From the definition of \mathbf{Q}' above:

$$d\theta > 0 \iff 2d\theta > 0 \iff \tan(2d\theta) > 0 \iff \frac{b}{a'} > 0,$$

where we have required $2d\theta$ to be in the first quadrant. Now, from the definitions of a' , and b , above, we have:

$$\frac{b}{a'} = \frac{dt\beta k_2}{a + dt\beta k_1}.$$

By assumption, $a > 0$ and $0 < \phi < \frac{\pi}{2}$, where the latter implies $k_2 > 0$, by the expression for κ , above. Because both β and dt are positive, the result follows.

□

4.2.4 Discussion

This completes the derivation of our cell fluid model. We have extended the theory presented by Volfson et al. in [165] to form a full 2D PDE model for growth and ordering of bacterial cells in a microfluidic trap. The key extension in our model is the formation of a Poisson's equation PDE for the cell pressure, which, in contrast, is an ad hoc, spatially invariant scalar equation in the 1D model presented by Volfson et al.

In the statement of our model (and in our simulations), we have set the cell density to unity. We argue that this does not alter the conclusions of our model, since cell ordering is driven by the velocity gradient (per Eq. 4.16), which is negligible until a trap is at, or near, a close-packing density. We observe that, if cells are not in close contact, they mainly only fill available space; thus, they cannot collectively exclude cell mass to form velocity gradients. Further, although cell ordering dynamics are active during a trap-filling phase of a microfluidic experiment, the ordering is transient, since cells are continuously pushed towards the open boundaries once the trap fills. Thus, any initial defects in cell ordering, for example, will be rapidly flushed by the volume exclusion of cell growth once the trap reaches a close-packing density, and the resulting steady-state velocity gradient, from this time forward, will dominate cell ordering.

We have also included in our continuum model the full vector equation for the dynamics of \mathbf{Q} , as presented in the Supplementary Information of [165] (a reduced equation of that presented by Olmsted & Goldbart in [117]). In contrast to Volfson et

al. (in their 1D model), we do not include the penalty parameter $1 - q^2$ for the rate of \mathbf{Q} dynamics (a heuristic to ensure $q \leq 1$). Rather, as we will see in the results of our simulations, we introduce a phenomenological noise term to the director \mathbf{n} that keeps q bounded. We believe that this is more realistic physically, since it helps capture the random cell-cell, cell-wall and cell-flow (i.e., media flow) interactions that exist among the order of $10^3 - 10^5$ cells in an actual microfluidic trap experiment. This is, in our opinion, closer to the intent of the dynamical equation for \mathbf{Q} as presented in [117], since it captures stochastic interactions that, in the case of liquid crystals, are due to thermodynamic effects.

In the next section, we will present results of the continuum model in a study of bacterial cell growth and ordering in an open-walled microfluidic trap. We limit our simulations to this trap geometry; however, our model (in contrast to Volfson et al.) is generalizable to traps of other geometries with boundary configurations that include one, two or three-walled traps, for example. Some of our conclusions will serve to confirm results from our agent-based model (Chapter 2), while others will extend our understanding of the spatial inhomogeneity of the *rate* of ordering in an open-walled trap.

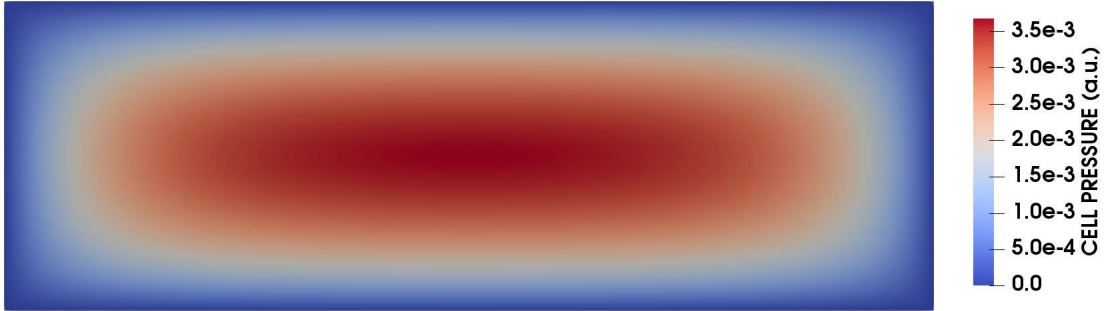


Figure 4.2: **Pressure field of the continuum model.** Scalar, cell-pressure field solution for an open-walled microfluidic trap simulation that used the continuum cell growth model. The parabolic pressure profile in the vertical center is expected by the theory. Aspect ratio of the trap 1:3. Boundary conditions were homogeneous Dirichlet for pressure: $p = 0$ at the four trap walls. Model parameters: $\alpha = 0.03 \text{ min}^{-1}$, $\gamma = 1, \rho = 1$. A spatially variant pressure field is not possible in the reduced 1D model presented by Volfson et al in [165].

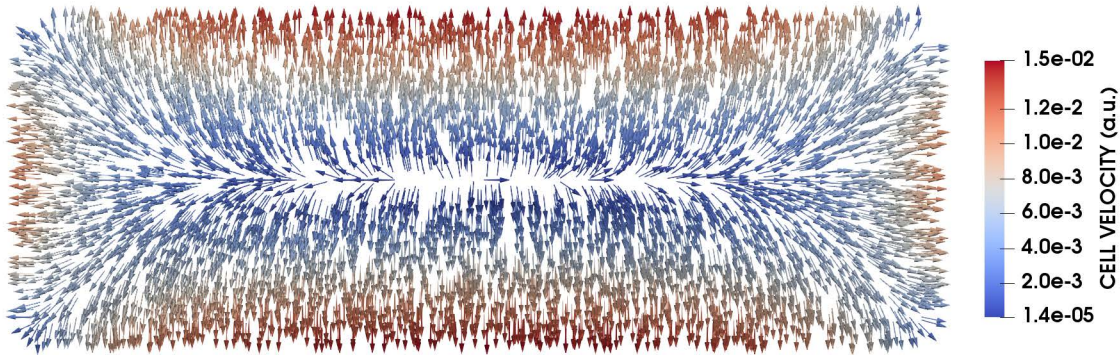


Figure 4.3: **Velocity field of the continuum model.** Velocity vector field of the continuum model for an open-walled, microfluidic trap. Boundary conditions were homogeneous Neumann: $\nabla \mathbf{v} \cdot \vec{\mathbf{n}} = 0$ (where $\vec{\mathbf{n}}$ here refers to the outward normal of the boundary). The velocity field was computed as: $\mathbf{v} = -\mu^{-1} \nabla p$, where p is the scalar pressure field from the previous figure, and μ is the velocity-based damping parameter. Velocity direction is indicated by arrows, velocity magnitude by arrow color. Velocity direction is straight up-down in the middle of the trap, as observed in experiments and ABM simulations in Chapter 2. Velocity direction rotates to the nearest open wall as one moves horizontally (center-out) in either direction.

4.3 Results

4.3.1 Cell pressure and velocity fields

We now present results of our continuum model dynamical equations to study growth and ordering in an open-walled microfluidic trap. We note our equations allows us to capture the cell *pressure* and resulting cell *velocity* field in the open-walled geometry using extremely simple assumptions:

- cell forces are a balance between cell growth expansion, and a velocity-based friction (Eq. 4.5).
- Cell growth is isotropic, and the velocity field diverges at the cell growth rate (Eq. 4.8).
- Boundary conditions at the edges of the trap are zero stress, $p = 0$, and zero normal velocity derivative, $\nabla \mathbf{v} \cdot \vec{\mathbf{n}} = 0$ (where $\vec{\mathbf{n}}$ here is the outward normal direction).

In Figure 4.2, we show a heat map of the cell pressure field in an open-walled trap simulation that used our continuum model (simulations were performed using the open-source finite-element software *Fenics* and are visualized using *Paraview*). Boundary conditions in this realization were set such that the pressure $p = 0$ on the boundary. Similarly to the cell spring compression field presented in Figure 2.3 in Chapter 2, the cell pressure result is parabolic in the middle of the trap in a vertical section.

In Figure 4.3 we show the resulting velocity field that was generated (using

Eq. 4.6) directly from the pressure solution to the cell growth PDE, Eq. 4.9. As observed in our ABM simulations of an open-walled trap (Chapter 2), we see vertical cell flux in the middle of the trap, and lateral expansion near the left/right ends. In the next section, we will see the implications for *cell ordering* of this velocity field solution in an open-walled trap. We recall that the Q-tensor component dynamics are directly proportional to the symmetric, traceless (i.e., non-isotropic) components of the strain-rate tensor $\nabla\mathbf{v}$.

Importantly, we can directly observe areas of the velocity field in Figure 4.3 where the strain-rate is in anisotropic shear. For example, where the horizontal and vertical centerlines of the trap meet (with the convention of positive direction upwards), the velocity gradient appears to be upwards only (the change in velocity moving left or right is, in contrast, vanishing). Also, we can deduce where the velocity appears to expand (in magnitude) *uniformly* in both the x and y directions, which indicates an *isotropic* expansion of the cell velocity. For example, as one moves from the middle of the trap outwards along the horizontal centerline, the velocity expansion direction transitions from an approximately purely vertical (at the trap center) regime, to an approximately purely horizontal one (at the left-center or right-center edge). Assuming this transition is continuous and monotonic, we expect the existence of a single location on the horizontal centerline where the ordering rate is *zero*, since the spatial velocity derivatives in the x and y directions must at some point be equal, under these assumptions.

Therefore, we expect (based on the ordering dynamics of Eq. 4.16) that cells in the middle and edge-regions of the trap will experience a relatively *strong* rate of

ordering, due to the observed anisotropic shear of the velocity in these locations. Likewise, we expect a region somewhere *near* the left and right boundaries (along the horizontal centerline) to experience a relatively *weak* ordering rate

These expectations will be confirmed in the next section, where we will show simulation results of the dynamics of q -scalar and \mathbf{n} that used the advection/reaction equation Eq. 4.16. We further comment on another region where we expect a high degree of ordering, according to Eq. 4.16: at the four corners of the trap, where the velocity field transitions sharply from vertical to horizontal (or vice-versa).

4.3.2 Q-tensor scalar order parameter and director

In this section, we will show results from the simulation of Eq. 4.16 We state here for reference the parameters used in this equation:

- Q_{ij} : the (i, j) component of the Q-tensor; in our 2D formulation, only two entries are independent. We computed both q -scalar and \mathbf{n} from these entries, according to Proposition 4.2.3.
- \mathbf{v} : the velocity field under which Q-tensor is advecting. We used the velocity solution from Figure 4.3. The velocity field was temporally constant in our simulation.
- β : a kinetic parameter that scales the rate of ordering. We set $\beta = 0.5$
- $\kappa_{ij}^{(s)}$: the (i, j) component of the symmetric, traceless strain-rate tensor. The strain rate was computed from the velocity solution from Figure 4.3, and was

converted manually (in the simulation code) to the traceless, symmetric form. Only two components of $\kappa_{ij}^{(s)}$ are independent.

4.3.2.1 Simulation without noise

For our simulations, we again turned to the finite-element solver *Fenics*. Our initial results for q -scalar do not include any phenomenological noise added to the system, and we will see that this leads q -scalar to become unbounded according to Eq. 4.16. In the following section, we will introduce a phenomenological noise to the director angle \mathbf{n} in our simulations, which we will see bounds q .

We initialized each of the two independent components of \mathbf{Q} to zero, and evolved these Q_{ij} according to 4.16. At each time step, we recorded the resulting order parameter q -scalar (computed according to Proposition 4.2.3) from the two independent components of \mathbf{Q} . In Figure 4.4, we show the resulting heat map for q -scalar after one timestep.

Because the velocity field was constant in our simulation, the forcing term for Eq. 4.16 was also constant; thus, this initial heat map reflects the relative rate of ordering of q -scalar (i.e., advection had not yet influenced the spatial mapping of q -scalar) in different regions of the trap. From the horizontal centerline section in the second panel of this figure, we see that indeed a cusp appears near the left and right boundaries, which indicates a region where the cell ordering in fact vanishes (referring to the left-axis scale of the figure). We expected the existence of this point from our discussion in the previous section, where we argued that, along the

horizontal centerline of the trap, the velocity expands in a purely vertical direction in the center, and in a purely horizontal direction at the left and right boundaries, and that (under continuity and monotonicity assumptions) this implies the existence of a point of purely isotropic velocity expansion; hence, the ordering rate vanishes, according to our model.

4.3.2.2 Simulations with noise added to the director angle \mathbf{n}

We recall that in the 1D reduced model presented by Volfson et al. in [165], a heuristic penalty term $1 - q^2$ was added to the q -scalar rate equation in order to keep $q \leq 1$. In our next simulation, we will explore adding a phenomenological noise to our system, which allows us to both capture stochastic effects in our model, and also, to avoid use of the heuristic penalty term for \mathbf{Q} dynamics. The results of a simulation with an added Gaussian noise to the director angle is shown in Figure 4.6. The Gaussian noise was mean-zero and variance $\approx \frac{\pi}{64} \text{ rad}^2$ (standard deviation $\approx 3 \text{ deg.}$), and was added every time step to the computed angle of the director \mathbf{n} (our time step in simulations was fixed). In the figure, we show a heat map of the q -scalar order parameter at a time when the dynamics had stabilized in the trap. A time series is shown for a central patch that shows that q -scalar remained bounded and stationary.

In the heat map of Figure 4.6a, we see that the cusp regions advected slightly towards the left and right edges, but the minimum of q -scalar in this region remained within the bounds of the trap in steady-state. This is in contrast to the no-noise simulation case, where the cusp was completely advected outside the boundary (not shown). Indeed, in the case of a no-noise simulation, q -scalar will increase without

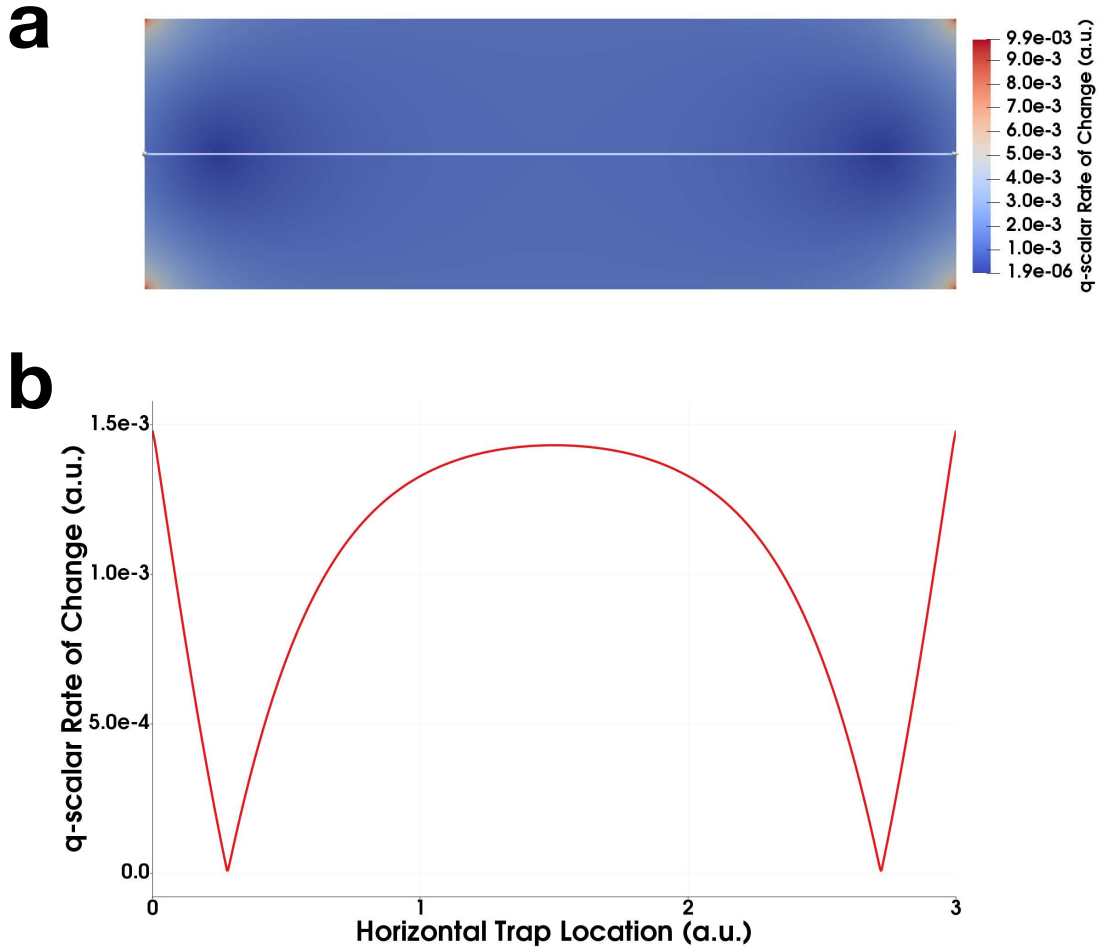


Figure 4.4: **Rate of ordering for q -scalar.** Heat map and horizontal cross-section result of the continuum model for the q -scalar order parameter in a simulation of an open-walled microfluidic trap. **a.** The heat map reflects the rate of q -scalar ordering as governed by the symmetric, traceless strain-rate tensor $\kappa^{(s)}$ in our model. A region of low ordering rate exists near the middle centerline and close to the left/right boundaries of the trap. A relatively high ordering rate exists at the four corners of the trap. This is due to the large off-diagonal terms of the strain-rate tensor: at the corners a small change in $x(y)$ gives a large change in velocity in the $y(x)$ directions, respectively. **b.** Horizontal cross-section represented by the white line in panel **a.** A cusp is evident near the left and right boundaries on the horizontal centerline and relatively strong ordering exists in the middle and edges of the trap along this line. The model predicts that perturbations to Q-tensor will recover slowly in the areas of low ordering rate, and that persistent disorder will therefore result with sufficient continuous perturbation strength. Trap aspect ratio is 3:1.

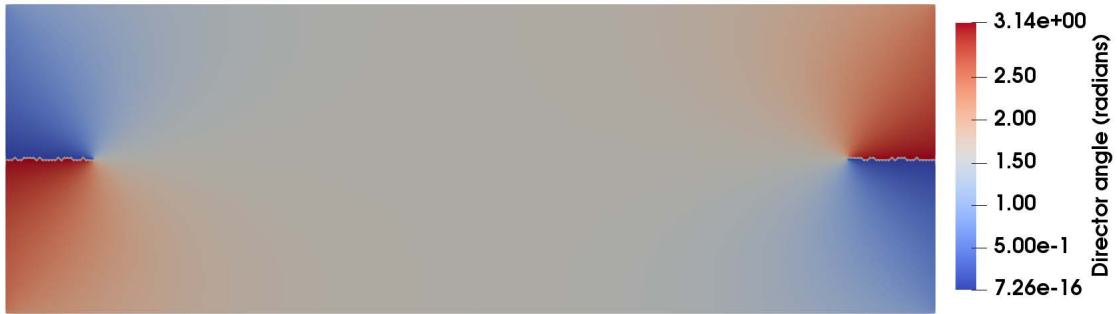


Figure 4.5: **Director angle field of Q.** Heat map of the continuum model for the director field \mathbf{n} in a simulation of an open-walled microfluidic trap. The heat map reflects the initial spatial mapping (at the first simulation step) of the director angle as governed by the symmetric, traceless strain-rate tensor $\kappa^{(s)}$ in our model. Because \mathbf{n} is π -symmetric by definition, the direction angles 0 and π are equivalent. Singularities exist in the heat map at the transition between these two values, but the director angle is continuous (the visualization discontinuity is an artifact of the π symmetry of \mathbf{n} and cannot be avoided). The model predicts that the director angle is horizontal at the center point of the left and right edges, and vertical at the middle of the upper and lower edges, as expected from the velocity field solution of the model and ABM simulations in Chapter 2. A cusp appears near the left/right edges along the horizontal centerline where the strain-rate tensor has no anisotropic shear (i.e., it is purely isotropic). Angle convention is increasing clockwise from angle zero ($= \pi$) oriented horizontally. Trap aspect ratio is 3:1.

bound at all regions in the trap (though at different rates, as indicated by Figure 4.4). It is for this reason that Volfson et al. (according to their paper) added the penalty term: to keep $q \leq 1$ heuristically.

We find that the addition of a phenomenological noise term to the cell angle helps capture the stochastic behavior — in a very simplified way — that such a large number of interacting agents in a biological system may exhibit. We have chosen parameters (both the variance and kinetic parameter β) ad hoc, but we believe, given experimental data, that these parameters could be fit to the data, and provide good agreement with the ordering dynamics in a trap.

4.4 Discussion

We have presented a continuum model for bacterial growth and ordering in microfluidic traps that uses equations from fluid dynamics, and the Q-tensor theory of liquid crystals. This model is in contrast to the ABM presented in Chapter 2: We relaxed the modeling of cells as individual *agents*, and studied the resulting pressure and velocity fields that emerge from an assumption of isotropic growth in a PDE formulation. We briefly review our development in this Chapter:

1. Under the assumption of a non-inertial dynamics regime, we established a Poisson's equation PDE for the cell growth pressure, with isotropic cell growth parameterized by the growth rate α , and a velocity damping factor μ .

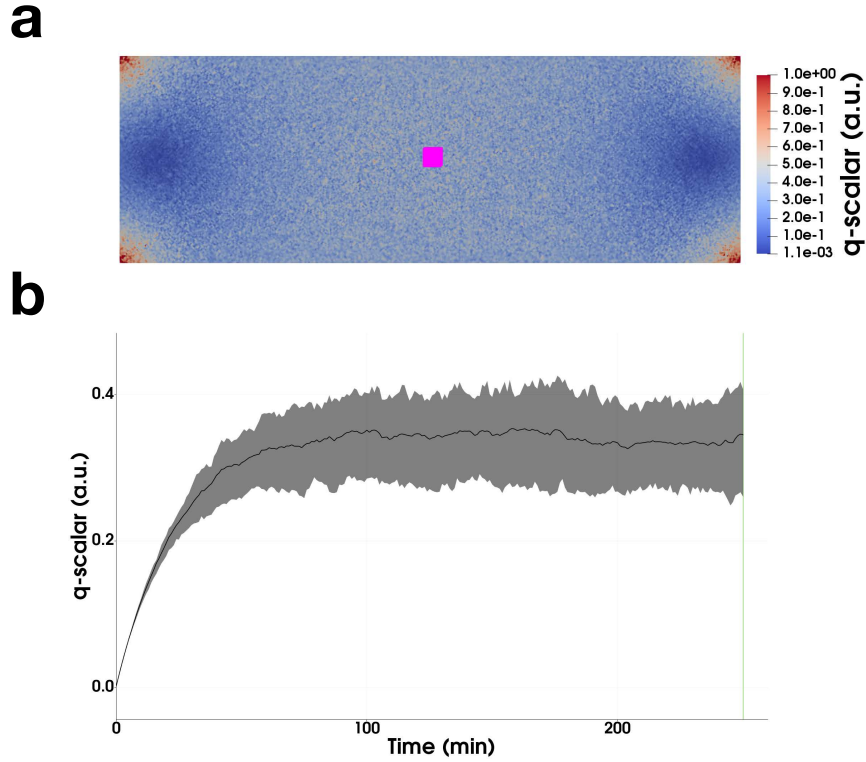


Figure 4.6: q -scalar order parameter and time series. Heat map and time series from a simulation of the continuum model for the q -scalar order parameter in an open-walled microfluidic trap with added noise to the director angle \mathbf{n} . **a**. The heat map reflects the value of q -scalar throughout the trap at a the final time point in panel **b**. The region of low ordering advected slightly along the middle centerline towards the left/right boundaries of the trap, but stabilized and was persistent. This is in contrast to the no-noise case where the cusps were completely advected out the side boundaries. High ordering remained persistent at the four corners of the trap due to the sharp transition of vertical-horizontal velocities in these regions. **b**. Time series of the q -scalar order parameter in a central region indicated by the magenta patch in panel **a**. The spatial average of the patch is indicated by the solid line, and quartiles by the shaded area. The simulation shows that q -scalar remained bounded and stationary in distribution in the selected region. Similar stationarity was seen in all regions of the trap. The simulation predicts that perturbations to Q-tensor director \mathbf{n} lead to stabilization of the order parameter. This result contrasts to the model presented by Volfson et al., where a heuristic penalty term $1 - q^2$ was added to keep q finite. Mean-zero Gaussian noise of standard deviation $\approx 3 \text{ deg.}$ was added to the director angle \mathbf{n} at each time step. Other simulation parameters were as in the previous figures.

2. We solved the PDE for the cell pressure using Eq. 4.9:

$$\nabla \cdot \nabla p = -\mu\alpha,$$

and using boundary conditions that depend on the trap geometry (where we have considered an open-walled microfluidic trap). We then computed the resulting vector velocity field using Eq. 4.6:

$$\mathbf{v} = -\mu^{-1}\nabla p$$

3. We then computed the strain-rate tensor $\nabla\mathbf{v}$ and converted it to a symmetric, traceless tensor $\kappa^{(s)}$ to serve as the forcing function for our advection/reaction equation for Q-tensor:

$$\partial_t Q_{ij} + \mathbf{v} \cdot \nabla Q_{ij} = \beta \kappa_{ij}^{(s)},$$

4. With the velocity field fixed, we then advected/reacted the Q-tensor components (with mean-zero Gaussian noise to the director angle) according to the above equation and recorded the results for the q -scalar order parameter and director \mathbf{n} .

Our choice to use an open-walled microfluidic trap for our simulations is based on our experience with this geometry from experimental data. However, our model is general, and we claim it can be used with any number of walls in a trap, as well as possibly non-rectangular traps. The extensibility of our model relies on its simplicity: We solve a well-known PDE under simple assumptions of cell growth, damping forces and boundary conditions.

Our theory and simulations lead us to a deeper understanding of the mechanisms of ordering and *persistent disorder* of bacterial cell nematogens in a microfluidic trap. We see that ordering dynamics can be directly inferred from the velocity solution of the model, and that a phenomenological noise is an essential ingredient to capture the bounded order and persistent disorder in the simulation. We believe that adding a phenomenological noise to our simulations is essential to capture the dynamics accurately. In ABM simulations we saw a persistent disorder of cell alignment near the left/right (in our convention) boundaries of the trap as well as a strong vertical ordering in the middle region of the trap. The disorder we observed would *not be captured* by the model presented by Volfson et al., since the heuristic penalty term $1 - q^2$ would only keep q -scalar bounded *uniformly* in the trap, and not show regions where disorder should persist. We believe this is a significant extension to the understanding of the dynamics of ordering in an open-walled microfluidic trap.

Whereas Volfson et al. presented a 1D model to describe the mechanism for *ordering* of cells in a two-walled microfluidic trap, we have presented a more general system of PDE that captures both the mechanism of ordering, and the persistent existence of *disorder* in an open-walled microfluidic trap. We conclude that the boundary conditions of the cell growth pressure play a significant role in the mechanism of ordering. In our model, the pressure field drives the velocity field and the resulting velocity gradient, whose anisotropic shear then drives cell ordering, according to Eq. 4.16.

Chapter 5

A Model for Protein Expression Modulated by Mechanical Constraint

5.1 Motivation and experimental evidence

In synthetic biology modeling, the creation of predictive mathematical models assists in testing and optimizing various experimental designs before making the time-consuming (and often, costly) efforts of performing experiments. Models are often the result of enhancements or extensions to other models: We have, for example, presented an extension to a continuum cell model in Chapter 4. Other models are created anew in an attempt to explain observed phenomena, and based on the accuracy and precision of these models, they can be used predictively to help design

experiments and further the scientific investigation at hand.

In this chapter, we will present a *de novo* bacterial protein expression model that modulates a protein production rate by mechanical constraint. This model attempts to explain anomalous experimental data examined from a collaboration with the Bennett Lab at Rice University. The experimental data are fluorescent-channel images of bacterial cells in microfluidic traps. The experiments were designed to measure bacterial cell fluorescent protein (FP) expression in response to various measured concentrations of an inducing protein known (generally) as a homoserine lactone, or HSL [17], that was present in the cell media. The cells were genetically modified to respond to HSL protein concentration by producing a fluorescent protein marker that could be measured using standard fluorescent microscopy techniques [45, 32]. Experiments were performed using a gradation of HSL concentrations in the media with the intent of generating a calibration curve that mapped the measured FP signal to the inducing concentration of HSL.

To clarify the setup for this experiment, we consider an analogy: Imagine a set of identically manufactured temperature sensors that emit light with an intensity that depends on the temperature. In order for the sensors to be used to measure temperature in experiments, their light intensity output must be *calibrated* by measuring their output under *known* temperature conditions. After acquiring a sufficient set of (temperature, intensity) points, a model is constructed to fit the measured intensities to the calibration temperatures, and one generates what is called a *calibration curve*. Assuming similar conditions and operation of the sensors, one uses them “in the field” by measuring their light intensity in *unknown* temperature conditions,

reading from the calibration curve, and inferring the temperature data point. Such a procedure is ubiquitous (and necessary) in a wide range of scientific instrumentation.

Problems can easily arise in a calibration procedure, and the following are examples of concern in a general calibration setting:

1. The instrument or technique used to establish the *known* measurement value (e.g., temperature, concentration, etc...) must itself be in calibration, i.e., it must be sufficiently accurate and precise.
2. The environment of the sensors during calibration should be *uniform* under the calibration value. For example, in a temperature bath, there should be no “hot spots” or other temperature gradients: all devices should be uniformly exposed to the calibration data point.
3. The device(s) used to measure the output of the sensors must also be considered for accuracy, and as a source of noise. Both random and systematic errors can occur in the measurement device(s).
4. A *distribution* of outputs from the sensors under (assumed) accurate and uniform conditions is expected. This is true both across sensors and across time in any single sensor device. Depending on the application, one calibration curve may be made for use in all sensors, or each device may be calibrated independently. The distribution of sensor outputs is usually taken into account in this decision.

With respect to the last point above, it is important when performing a calibration

procedure to have an *expectation* of the distribution of measured values. Measurements with significant deviations from expectations should be noted and investigated for sources of error or as anomalous (and potentially interesting) data. However, this is not possible without establishing the expectations before the calibration *per se*.

In this Chapter, we will investigate experimental calibration data whose measurements were bacterial cell FP expression, and whose calibration values were inducing HSL concentrations in the bacterial media. The expectation from this data is that FP expression should increase with increasing HSL concentration.

Both visually and quantitatively, these experiments showed increasing mean-field FP expression of the bacterial strain “devices” under study in response to increasing HSL concentration in the media. However, all calibration experiments also exhibited significant spatiotemporal variation in FP expression, such that the measured signal was up to 2x larger than an “expected” signal, as determined by sampling an early frame of cells from the experiment. The appearance of spatial variation in the FP expression is anomalous since cells were assumed to be in temporally constant and spatially homogeneous conditions of HSL inducer.

We conjecture that the anomalous data from these images contain *information* whose patterns cannot be attributed to experimental noise, systematic error, or intrinsic or extrinsic noise, within the context of biological variation. We aim to show that this signal can be well modeled by a pressure-induced increase of protein production rate. We are not aware of any published paper that observed the phenomena we shall present, nor any that introduces a model for an increase of protein expression under mechanical constraint.

As inspiration for this model, we quote from [64]:

Patterns are observations of any kind showing nonrandom structure and therefore containing information on the mechanisms from which they emerge.

5.2 Experimental data

5.2.1 Overview

Calibration experiments were performed where FP response was measured in a bacterial strain that we shall call the “receiver-strain.” The architecture of the genetic signaling circuit is shown in Figure 5.1, where in the calibration experiments a sender-strain was replaced by a constant C4HSL concentration (we omit details of this circuit and refer the reader to [32] for a similar architecture). Experiments with various concentrations of HSL were made with the intent of generating a calibration mapping from measured FP to received HSL in the receiver cells. Calibration runs were performed under concentrations of: 0, 1, 1.5, 2, 3, and 5 μM C4HSL.

5.2.2 Example 2 μM calibration experiment

An example calibration experiment (2 μM) is shown in Figures 5.2 – 5.5. Figure 5.2 shows a typical observed spatial variation of FP expression under constant (and assumed uniform) HSL in the media. The following were typical of all calibration experiments, and were exemplified in the 2 μM experiment of Figures 5.2 – 5.5:

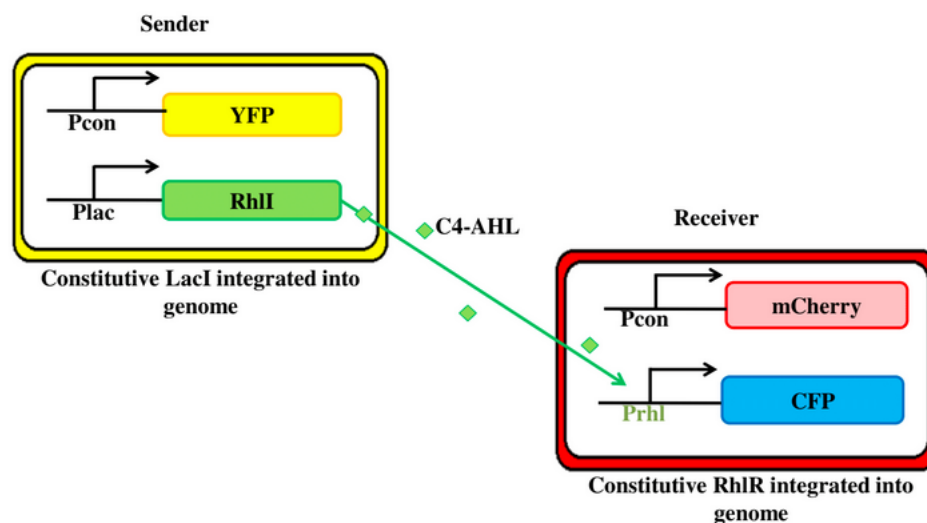


Figure 5.1: **Sender-Receiver cell signaling.** Example genetic circuit that uses HSL signaling between strains. In calibration experiments, the sender-strain was replaced by a measured HSL concentration in the aqueous growth media. The receiver strain responds to the local concentration of HSL, which is a diffusible molecule through the cell membrane. The HSL binds with a transcription factor, and the complex activates the promoter that drives FP expression (in the receiver strain, the FP is Cyan Fluorescent Protein). Details of a similar circuit can be found in [32]. Figure courtesy of R.Alnahhas, Rice University.

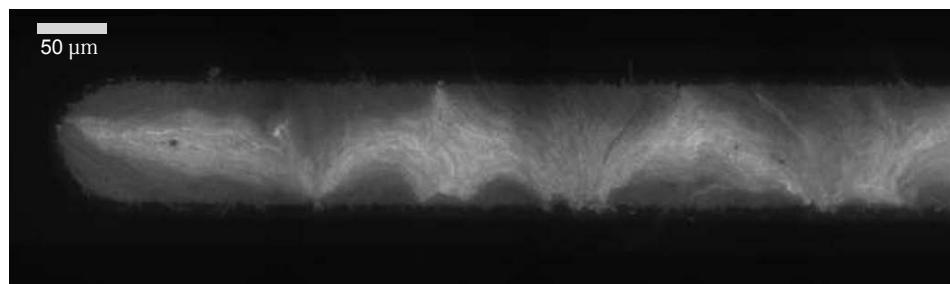


Figure 5.2: **FP Expression under constant HSL.** Image data showing FP response from a $2 \mu\text{M}$ C4HSL receiver-cell calibration experiment in a narrow extended trap (8-8-17, frame 33/161). Spatial heterogeneity was typical of all microfluidic trap experiments that were observed. Sharp spatial gradients in measured FP response occurred across and around regions of occluded cell flow. The spatial variation of FP expression in this image is anomalous: the cells were assumed to be under a uniform concentration of inducing HSL. Unpublished image courtesy of the Bennett Lab, Rice University.

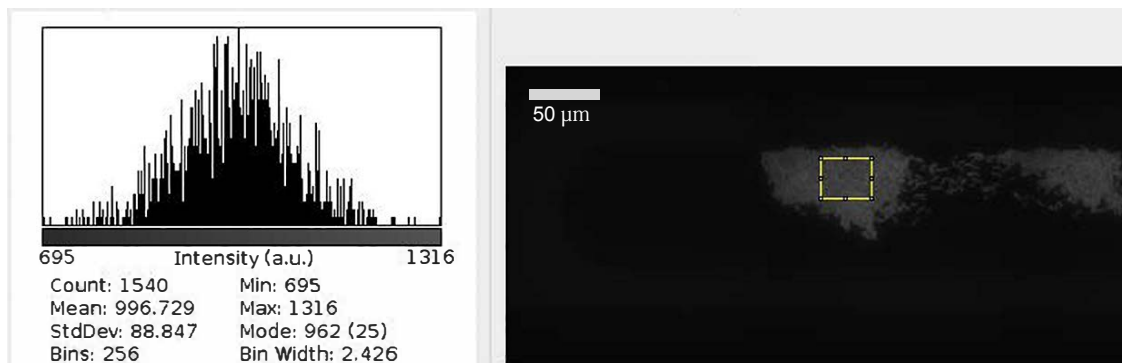


Figure 5.3: **Early-frame CFP Image and Histogram.** Image frame showing CFP response from the same experiment as in Figure 5.2. A histogram is shown (left image) from a small patch (yellow outline, right image) in an early frame from the experiment. Mean CFP expression in this area correlates with specific regions later in the experiment (see Figure 5.4). Before the trap filled, cells in small colonies did not show sharp spatial variation in expression of FP. Unpublished image courtesy of the Bennett Lab, Rice University.

5.2.2.1 Cell occlusions inhibit cell flow

Cell occlusions often appeared near a boundary of the trap. Cell exponential growth and division resulted in volume-exclusion cell flow that was inhibited by these occlusions and cells had to exit the trap by flowing around them. These formed canonical (inverted) “U-shapes” outlined by a sharp FP expression gradient that appeared across the occlusions. Occlusions appear to be the result of “sticky” cells, larger than average cell size, and/or a multi-layering of cells that resulted in increased cell-trap friction at these locations.

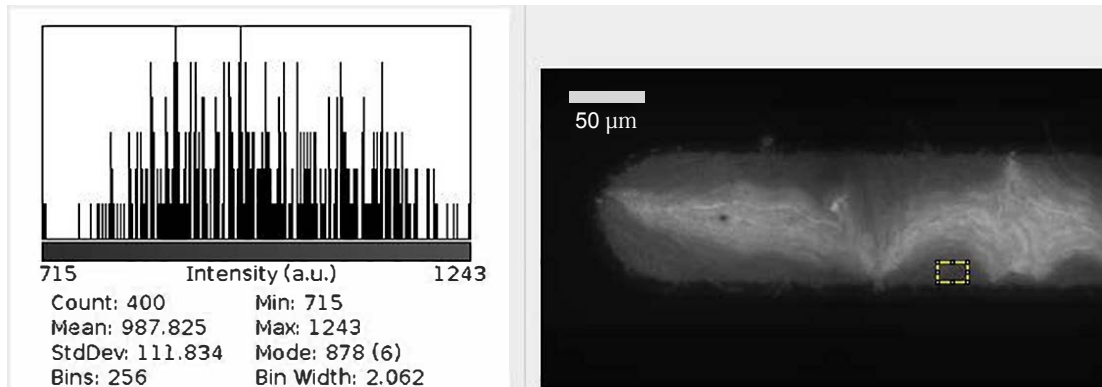


Figure 5.4: **CFP response underneath an occlusion.** Image frame showing CFP response from the same experiment as in Figures 5.2, 5.3. A histogram (left image) of CFP is shown in a small patch (yellow outline, right image) of the trap where cells were *underneath an occlusion of cell flow*. CFP histograms in these regions correlate with those of the early-experiment frames, as can be compared here with the histogram of Figure 5.3, which shows approximately the same mean CFP expression. This correlation was typical across all occlusions within all calibration experiments analyzed. Unpublished image courtesy of the Bennett Lab, Rice University.

5.2.2.2 Spatiotemporally heterogeneous FP expression

The cell blockages outlined above were easily visible because cell FP expression *outside of* a cell occlusion was grossly higher than that of cells *underneath* an occlusion (by *underneath* we mean on the trap-boundary side of the occlusion, whether the boundary is “up” or “down” in an image). The heterogeneous expression cannot be explained by optical effects since it is independent of any fixed location in the trap. This large variation in FP expression under assumed uniform HSL is a significant anomaly that appeared in all calibration experiments.

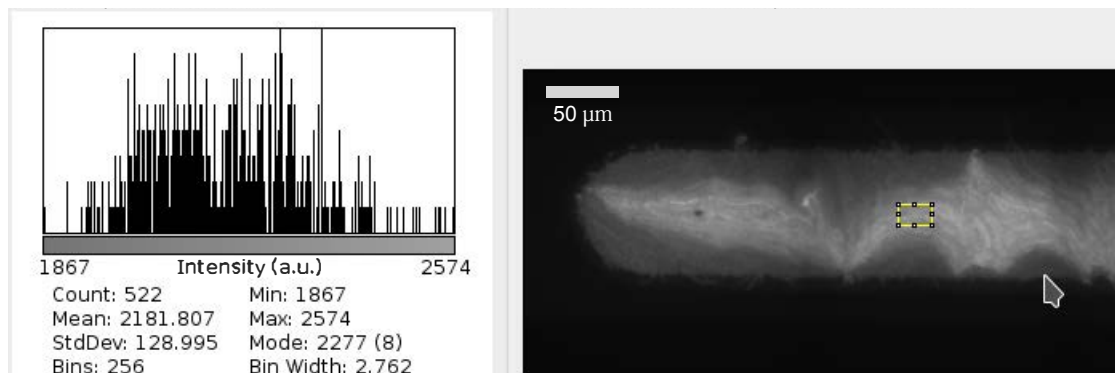


Figure 5.5: **CFP response outside of an occlusion.** Image frame showing CFP response from the same experiment as in Figures 5.2-5.4. A histogram (left image) of CFP is shown in a small patch (yellow outline, right image) of the trap where cells were *outside of an occlusion of cell flow*. CFP expression in these regions were sharply higher than areas *underneath* occlusions. These large, spatiotemporally variant CFP gradients were typical across all calibration and sender-receiver experiments analyzed. Unpublished image courtesy of the Bennett Lab, Rice University.

5.2.2.3 Spatiotemporal correlations of FP expression

Importantly, mean FP measurements taken *underneath* an occlusion consistently matched those taken at an early time-point of the same experiment, when cells had not yet filled the entire trap, and only small isolated colonies had formed from seed cells. Figure 5.3 shows such an early time-point ($2\mu\text{M}$, frame 6/161) FP image, where a histogram is shown of an early seed colony, well before the trap filled. Figure 5.4 shows a histogram of cells in an *underneath* area of an occlusion later in the same experiment. Mean FP expression in this boxed region matches closely that of the early-time frame (see histogram data in left parts of the images). This matching was typical across all calibration experiments and all occlusions therein. See Figure 5.5 for a comparison of FP expression *outside of* an occlusion, where mean expression was $\approx 2x$ higher. This scale factor was also typical across all occlusions

in all calibration experiments. We form a conjecture as to a possible cause of the observed over-expression later in this chapter.

5.2.2.4 Asymmetric cell expansion flow

Cell flow often runs top-to-bottom or bottom-to-top in various, apparently random regions of the trap. Our agent-based cell and trap modeling predicts that cells should exit the trap symmetrically, in a vertical striping pattern, in what we often call some variant of: “symmetric quasi-mother machines.” When watching time-series of the experimental images, cell flow could also be seen to change rapidly from one direction to another within the same region, and at a time-scale much faster than the growth rate of the cells. This spatiotemporal variation is, decidedly, not an expected result of any cell-growth or trap model that we have formed to date, and we conjecture that this variation is due to asymmetries in fluid pressure, and other hydrodynamic effects of media flow.

In Figure 5.2 cell flow is a mixture of top-bottom and bottom-top flows. Cells typically exited the trap in regions where FP appeared “funneled” at the boundary of the trap. In the right-most regions of the narrow-extended trap (not shown in the figures, but at the “bowtie”), cell flow could also often be seen funneled out the right-hand side from up to $\approx 250\mu\text{m}$ away, which implies the existence of a large pressure differential. The unidirectional cell flow was also seen to govern a repeatable, spatially variant FP expression, where cell FP becomes brighter as cells moved toward their exit boundary. We shall show that this spatial gradient of expression is consistent with a conjectured cause of FP expression gradients, and with the application of a

uniform velocity field that drives the cells to exit the trap unidirectionally with the field.

5.2.3 A second experiment

We now discuss analysis from a separate experiment: a three-strain (X-Y-Z) cascade that cycles an inducing signal in the media, which cycles on-off the X strain and subsequently, the entire X-Y-Z, three-strain circuit (we omit details of the experiment). Using the data of this experiment (file name: 161208-xyz-cascade-daw001), we originally attempted to fit a response curve of each strain with a simple protein production model.

However, after analyzing data from the calibration and sender-receiver experiments outlined above, we recalled that the XYZ experiment also showed significant and interesting spatial variation of FP under an assumption of uniform inducing signal (IPTG in the inducing molecule in this case, which de-represses the X strain, the first in the circuit, thus activating the cascade), which is a similar situation to that of the calibration experiments (where the inducer is a constant HSL). However, for a significant part of the XYZ experiment, and in more than one spatial region, the cells *did not* show the anomalies outlined in sections 5.2.2.1 and 5.2.2.4 (cell occlusions and asymmetric flow, respectively). Rather, cells in the X strain sustained expansion growth in “symmetric quasi-mother machines” that we expected from our simulation modeling of open-walled traps. An example image (frame 321/419) of the X-strain yellow fluorescent protein (YFP) channel is shown in Figure 5.6, which comes from

the left side of the trap.

This experiment gave us a valuable opportunity to study the anomalous protein expression in a different environment, and further, to validate the behavior of our model under different behaviors from the experiments. Importantly, the genetic circuit construction (plasmids), the experimental methods, and the measurement devices closely matched (or were identical to) those of the calibration experiments; hence, we were able to analyze additional experimental data under comparable experimental conditions.

5.2.4 Spatial heterogeneity of the FP expression

From Figure 5.6 we can see a clear spatial distribution of YFP that is brightest in the middle-region and tapers vertically to the horizontal boundaries of the trap. On taking a time and space average over several image frames of a cycle from this experiment, we can see that the spatial distribution is “bell-shaped” in nature. Figure 5.7 shows a plot of an average of a sequence of images from the experiment, where a rectangular region similar to the image shown in Figure 5.6 was divided into 30 horizontal slices, each of which was averaged for YFP for each frame (thus forming a numeric array of length 30 for each image frame, and the entries run top-to-bottom as the average of each horizontal slice). The rectangular region selected for this plot includes regions outside of the trap; thus, the sharp edges are visible (which decay to “black” and are low numbers numerically), and the trap proper is in the middle of the plot. This average is over 5 sequential frames of one of the cycles in the experiment

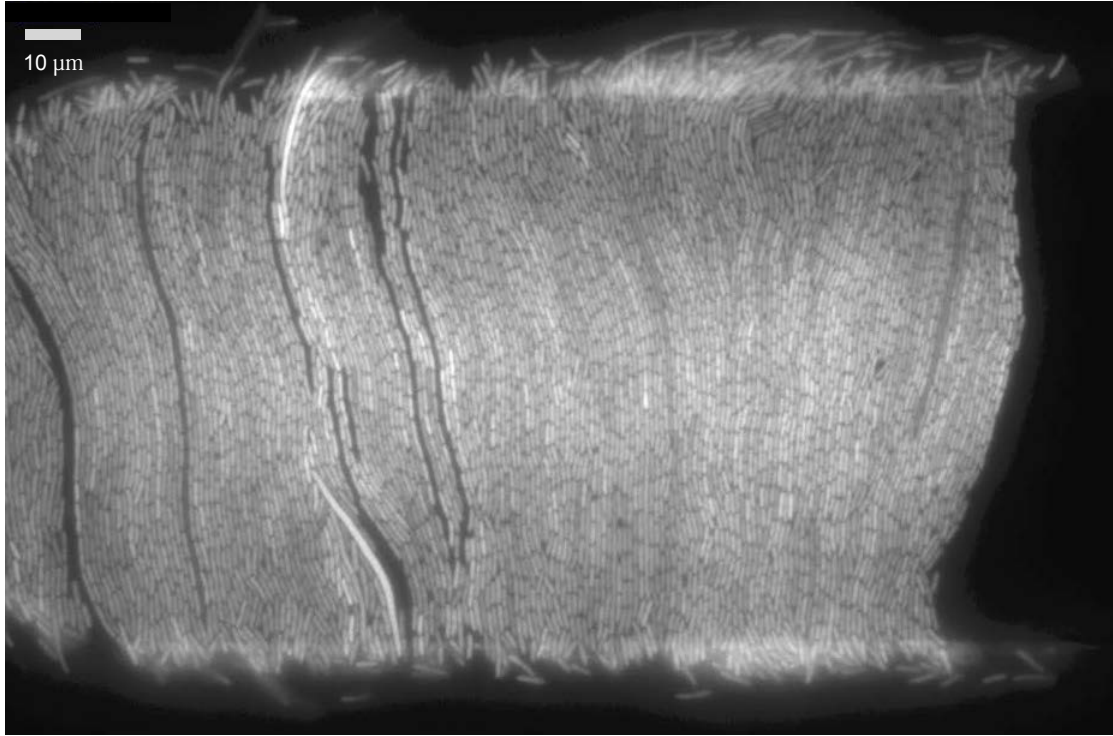


Figure 5.6: **Example XYZ cascade experiment frame A** A high-resolution images is shown of the YFP channel, which is the X strain marker (the same promoter for production of C14HSL) under de-inhibition of the lac promoter by the inducing IPTG in the media. A spatial gradient is clearly visible, where YFP is brighter in the middle of the trap and tapers vertically to the boundaries. Noticeably absent in this image is the appearance of cell occlusions and asymmetric cell flow. Cell flow for this strain in this experiment was primarily middle-out in a “symmetric mother-machine” structure. This symmetry isolates spatial variation, on average, to the vertical dimension. Also clearly visible is discrete cell-to-cell and lineage-to-lineage expression variation, which belies any conjecture that the average variation is due to optical effects. We analyzed the one-dimensional spatial variation by taking space and time averages (over one cycle of IPTG induction in the experiment) in Figure 5.8. Unpublished image courtesy of the Bennett Lab, Rice University.

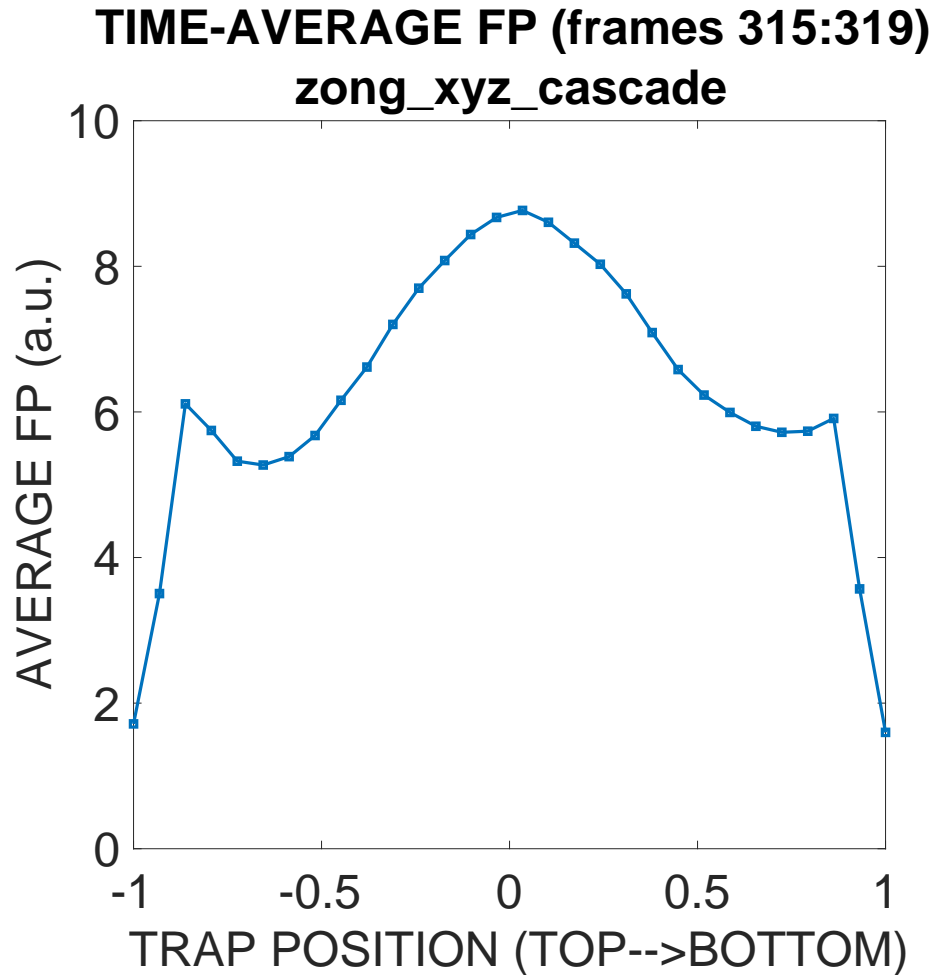


Figure 5.7: **Example space and time average of the XYZ cascade experiment during an IPTG cycle.** A plot of mean YFP expression from horizontal slices of an image segment similar to that of Figure 5.6. Each data point in the plot represents the spatial average of one of 30 horizontal slices in a fixed, rectangular image frame area that was further averaged over 5 sequential frames (image frames were taken 6 minutes apart; thus, this is a 30-minute average of YFP in each sliced spatial area). The 30 data points are numbered from top-to-bottom in the image, and the image segment selected includes regions outside the boundary of the trap (which appear dark as in Figure 5.6). The middle slices (approx. slices 7-25) show an average YFP expression that appears “bell-shaped” in distribution. YFP image data at the boundary of the trap is slightly brighter due to an optical change resulting from edge effects, which results in a curling-up of expression at the boundary. YFP then decays to noise levels as the top and bottom segment slices are well outside the trapping area of the cells as in Figure 5.6.

(frames 315:319) in the YFP channel (strain X). The “bell-shaped” nature to the expression of YFP in the trap is clearly visible. Edge effects lead to a brightness of FP and curling-up of measured value near the trap boundaries.

We claim that this spatial distribution is not due to optical effects, since on close inspection of the images, the variation is clearly seen as a discrete, fine-grained variation from cell-to-cell, and not as a coarser, region-to-region variation. However, *on average*, the cells show a distribution of FP that peaks in the middle region of the trap, and appears as a normal distribution as the distribution tapers to the edges.

We conjecture (in a following section) that the brightness distribution is due to increased protein expression that is caused by a stochastic event-chain that leads to an increase of protein production machinery. By protein production machinery, we mean anything that *increases* the production rate of FP (for example, increased transcription rates, increased plasmid copy number, decreased transcription/translation inhibition,...). We believe that the observed gradient of expression seen in Figures 5.6, 5.7 is due to an *increase* in protein production and not to a *decrease* in growth rate or degradation. The evidence to support this claim is presented in Figure 5.8.

In Figure 5.8 we show two plots of a single cycle of the XYZ experiment, where we outlined (not shown) a region near the inside-edge of the trap (blue color in Figure 5.8), and a second region centered in the middle of the trap (orange color). The time points are spatial averages over the rectangles selected for each image in the sequence (frames 311:360 are shown, which was one of six cycles of inducing IPTG being switched on/off, which switched on/off the X strain, shown in its YFP reporter channel). In the left image of the figure, we show each time series separately in its

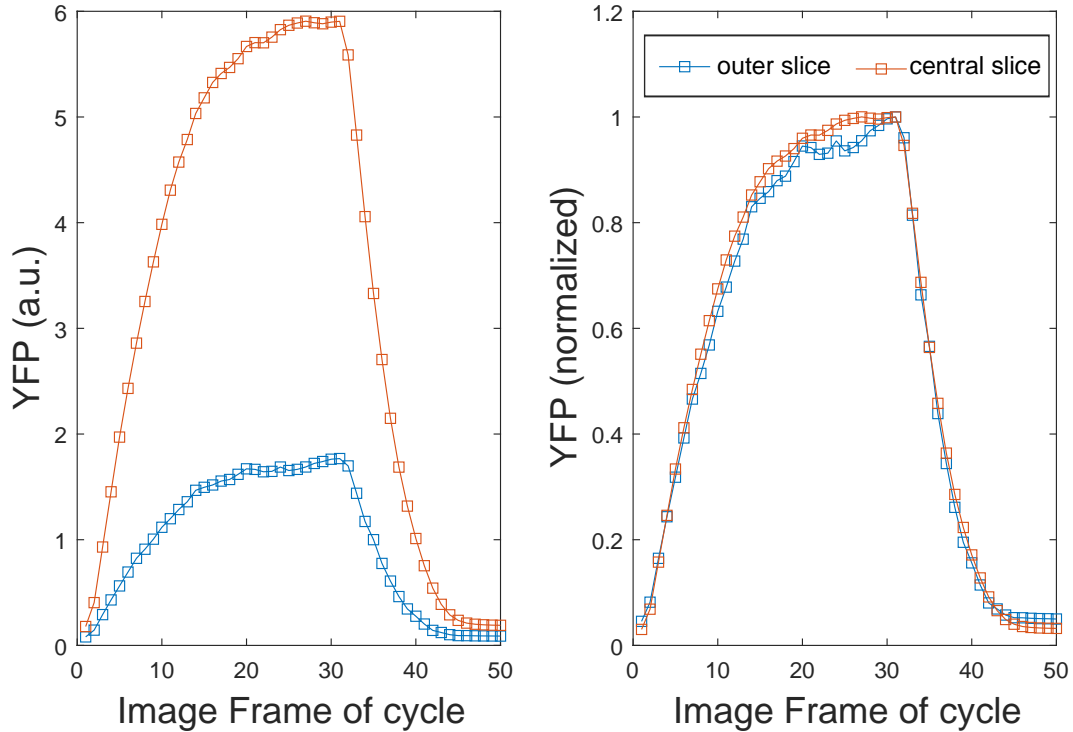


Figure 5.8: **Example XYZ cascade experiment time-series** Two data plots are shown of the same time-series of one IPTG cycle of the XYZ cascade experiment. The left plot shows the time-series displayed in its original relative scale, where the blue trace is a spatial average of a rectangular area just inside the boundary of the trap, and the orange trace is a central rectangular region of similar size. The left plot clearly shows that as cells responded to the step change of IPTG, production rate of protein of cells in the middle of the trap was, on average, sharply higher than that of cells closer to the trap boundary (this is indicated by the higher initial $dYFP/dt$ in the orange trace). The right plot shows the same time-series but now normalized to the peak expression of each trace in the cycle. This plot clearly shows that the normalized rates of expression (and subsequent decay) are nearly identical for cells in the two regions. This data is strong evidence to support the theory that spatial differences in expression stem from differences in protein production rate (as indicated by the difference in slope in the left figure) rather than differences in dilution/degradation rate (which would show a difference in the decay time constant in the right figure).

original relative scale (in arbitrary units of stacked YFP pixel data), whereas in the right image we show the two curves normalized to the peak point of the cycle. These two plots show strong evidence that the difference in expression in these two regions of the trap (the middle area and an outer area) is due to a production rate difference and not a dilution or degradation rate difference for the following reasons: in the left figure the *initial slopes* are different (which suggests different production rates when YFP concentration is small), and in the right figure the time-constants appear identical (the two curves approach their peak values, and decay to their final values at the same rate when normalized to the peak value). If dilution or degradation were to be all or part of the observed difference in expression, we would expect the time constant to be different in the two expression curves since these parameters govern its value. The right part of the figure shows this not to be the case. Further, if production rates were *not* different in the two regions, then the initial slopes in the left part of the figure *would be the same initially*, which also is clearly not seen to be the case.

Later in the document, we explore the causal relationship between observed spatiotemporal cell dynamics, and resulting cell FP expression. We conjecture this is due to a *growth constraint* that cells experience that is amplified by the sub-cell diameter height of the microfluidic device of these experiments (a low $0.9 \mu\text{m}$ gap exists in the “narrow-extended trap” from these experiments, where a bacterial cell diameter is $\approx 1 \mu\text{m}$). We suggest that, by some probabilistic event (or perhaps some chain of events), the production rate of protein markedly *increases* in the middle region of the trap (in the XYZ experiment), and that protein production *relaxes* as the cells

move toward the exiting boundary (after several division cycle time periods).

This theory is consistent with the observed, anomalous FP expression behavior that occurs in the previous experiments shown. For example, when cells are rapidly expanding (initially in the experiment as the trap fills), rapidly changing direction (due to the sudden appearance of an occlusion), or exhibiting top-bottom (or bottom-top) cell flow that also may involve an occlusion near the exiting boundary. Although we realize this is only a conjecture, and that verifying the hypotheses may be challenging, we emphasize that the observed behavior suggests an experimentally reproducible increase of protein expression via an apparent *mechano-biosensory* response of the cells. We suggest in the concluding section of this chapter that, if this behavior could be verified and captured, it could represent a compelling contribution—as a mechano-sensory *module*—to the synthetic biology toolkit.

5.3 Mathematical model

5.3.1 Protein expression

We begin by setting-up a simple ordinary differential equation (ODE) to model the cellular concentration of a protein vs. time (the protein here is non-specific). We use as a model the following common production/degradation ODE for protein expression P :

$$\dot{P} = \alpha - \beta P, \tag{5.1}$$

where α is the production rate, β is the dilution rate, and over-dot signifies derivative with respect to time. This is a simple first-order model with no spatial component, time-delays, stochastic component, or scaling of alpha with respect to any other cell parameter (for example, growth pressure). We assume that dilution dominates degradation of protein in this case; thus, β is equal to the growth rate of the cell. We will study more general models, which will include modulation of growth rate and active degradation of protein, below. The steady-state solution is:

$$\dot{P} = 0 \implies P = \frac{\alpha}{\beta}. \quad (5.2)$$

The steady-state solution for this first-order system is the ratio of production rate to dilution rate. It is easy to calculate also the time evolution of P :

$$P(t) = \frac{\alpha}{\beta}(1 - e^{-\beta t}). \quad (5.3)$$

5.3.2 Pressure-modulated production rate

To extend this model and to explain observed experimental protein expression variation (as mentioned above), we now incorporate a spatial pressure field under the conjecture that increased growth constraint on a cell will trigger an *increase* in protein production rate. From previous studies of cells in an open-walled microfluidic trap (see Chapter 2), we set the pressure field to be a quadratic function of position:

$$p(y) = 1 - y^2, \quad (5.4)$$

where p is the pressure, and where y is the vertical direction, which represents the dimension of interest — in 2D microfluidic traps — when cells tend to align in vertical

columns (see, for example, Fig. 2.3 in Chapter 2). We normalize the peak pressure to 1 in the middle of the trap. We set the middle position of the trap to $y = 0$, and the absorbing boundaries (for cells) at $y = \pm 1$ (top of the trap is $y = 0$). Boundary conditions for the pressure field are Dirichlet with zero stress; thus, the pressure field is continuous at the horizontal boundaries ($p = 0$) in this model.

We model the pressure effect on protein production by scaling the production rate α using a Hill function on the pressure [137]. We define the Hill function as a function of p :

$$H(p) = \frac{p^n}{p^n + K^n}, \quad (5.5)$$

where K is the pressure such that $H(K) = 1/2$, and n is the Hill exponent. We note that the Hill function in our model is implicitly a function of y by using Eq. 5.4.

We now define a modulated protein production rate:

$$\hat{\alpha} = \alpha[1 + aH(p)], \quad (5.6)$$

where a is a scaling parameter that models the intensity of the protein production rate increase (modulated by the pressure field via the Hill function, above). This first model extension is meant to represent a simple, spatially-mapped, and time-invariant link between pressure and protein production that, for simplicity, does not include stochastic effects, growth-rate modulation, or spatial transport of the cells. We can again solve for the steady-state and time evolution of protein expression levels as in Eqs. 5.2, 5.7, but now as a function of the spatial dimension y , by using Eqs. 5.4, 5.5 and by simply substituting Eq. 5.6 for α in Eqs. 5.2, 5.7. These two equations for

the pressure-modulated protein dynamics are thus:

$$P(t) = \frac{\hat{\alpha}}{\beta}(1 - e^{\beta t}), \quad \text{and} \quad \dot{P} = 0 \implies P = \frac{\hat{\alpha}}{\beta} \quad (5.7)$$

with $\hat{\alpha}$ given by Eq. 5.6.

5.3.3 Spatial transport

Because we are modeling cells that grow in idealized columns (in a quasi-mother machine fashion), cells will grow, divide, and be transported vertically from the center of the trap towards the open boundaries (see Chapter.2). Thus, as cells travel along their paths towards the trap exit, they experience different pressure profiles under the assumption of our quadratic pressure model. We now include in the model the advection of cells toward the open boundaries to account for cells integrating protein expression under a spatially varying production rate via the spatial pressure field model given above. To incorporate cell advection, we replace the left-hand side of Eq. 5.1 with the total derivative,

$$D/Dt = \partial_t + (\mathbf{v} \cdot \nabla),$$

to obtain the spatially-advecting protein PDE. Thus, on inclusion of advection and the pressure-modulated production rate $\hat{\alpha}$, Eq. 5.1 becomes:

$$\partial_t P + \mathbf{v} \cdot \nabla P = \hat{\alpha} - \beta P. \quad (5.8)$$

Now, our model from Chapter 2 (see also [165]) showed that we can set $\mathbf{v} = \beta y$, the 1D velocity solution for exponential-growth of expanding cells with exponential

growth rate β (the same value as the dilution rate in this case). This will greatly simplify the solution to this equation. In 1D, we have $\nabla P = \partial_y P$, which then gives:

$$\partial_t P + \beta y \cdot \partial_y P = \hat{\alpha} - \beta P. \quad (5.9)$$

We solve for the time-invariant spatial solution by setting $\partial_t P = 0$. After rearrangement, Eq. 5.9 becomes:

$$\partial_y(yP) = \frac{\hat{\alpha}}{\beta}, \quad (5.10)$$

To solve for the 1D steady-state solution, we assume each cell “point” is derived from a mother-cell at $y = 0$ (the center of the trap’s vertical column). Thus, we can solve Eq. 5.10 by integrating the right-hand side from 0 to y , which gives (for steady-state protein expression):

$$P(y) = \frac{\frac{1}{y} \int_0^y \hat{\alpha}(x) dx}{\beta}. \quad (5.11)$$

By incorporating cell mass transport into our pressure-modulated protein production model, we generated a closed-form solution for the time-invariant protein expression, as a function of the 1D spatial dimension y . This solution informs us to use an *average value* of $\hat{\alpha}$ over its course of travel from the center of the trap ($y = 0$) to the position of interest y , and to divide this value by the dilution rate β . Thus, this solution is identical in form to that presented in Eq. 5.2, with the numerator replaced by the spatial average (along the path of cell transport) of protein production rate (at each point on the path).

This equation is easily solvable numerically, and (more importantly) it is easy to see the *qualitative* behavior of the steady-state protein expression as we vary n or K , for example. For instance, in the limit for n large, the Hill function becomes

a step function at $p = K = 1 - \hat{y}^2$, where \hat{y} is the value of y at which the step function transitions $0 \rightarrow 1$. It is a simple matter to compute the average value of $H(y)$ depending on how far we are past the value of $\hat{y} = \sqrt{1 - K}$ for which $p = K$ (solved using Eq. 5.4) :

$$\bar{H}(y) = \begin{cases} 1, & \text{if } 0 \leq y \leq \sqrt{1 - K} \\ \frac{\sqrt{1 - K}}{y}, & \text{if } \sqrt{1 - K} \leq y \leq 1 \end{cases} \quad (5.12)$$

Then $P(y) = P(\bar{H}(y))$ upon substitution of Eq. 5.12 into Eq. 5.6, and upon using Eq. 5.11.

5.3.4 Degradation added to model

We now add to our model a more complicated framework that includes a possible *separate* rate of protein degradation. That is, we now assume that protein is degraded in addition to being diluted, and we introduce the term β_{deg} to represent this active degradation of protein. By including this new term, we update Eq. 5.9 to:

$$\partial_t P + \beta y \cdot \partial_y P = \hat{\alpha} - (\beta + \beta_{deg})P. \quad (5.13)$$

For notational simplicity, we introduce the term δ to represent the ratio of degradation to dilution:

$$\delta := \frac{\beta_{deg}}{\beta}.$$

This ratio thus represents the relative strength of active protein degradation to dilution alone (thus $\delta = 0$ is the case of vanishing degradation vs. dilution). We again

solve for the steady-state solution ($\dot{P} = 0$) using an integrating factor, which gives:

$$\partial_y(y^{\delta+1}P) = \frac{\hat{\alpha}}{\beta} \cdot y^\delta. \quad (5.14)$$

Again integrating both sides with respect to the spatial variable from the center of the trap to the position y of interest, we write the solution in the form:

$$P(y) = \frac{\frac{1}{y^{\delta+1}} \int_0^y x^\delta \hat{\alpha}(x) dx}{\beta}. \quad (5.15)$$

Note in the case $\delta = 0$, we recover Eq. 5.11.

5.4 Results

In Figure 5.9, plots of the steady-state solution of Eq. 5.16 are shown for two different cases: one for symmetric mother-machine expansion flow, and another with an added velocity flow-field on the cells such that the cells at the bottom of the trap (position $y = 1$) have zero net velocity, and all other cells move bottom-to-top. In the latter case, we alter the cell velocity field in Eq. 5.9 from βy to $\beta(y-1)$ (with the convention that cells flow in the negative y direction). This leads to the steady-state solution under unidirectional flow as a function of $y \in [-1, 1]$ as:

$$P(y) = \frac{\frac{1}{1-y} \int_1^y \hat{\alpha}(x) dx}{\beta}. \quad (5.16)$$

The latter case is observed frequently in the experimental data we have analyzed (i.e., this is not an isolated case). Importantly, in this case of unidirectional cell flow in our model, *the analytical solution recovers the experimentally observed rounding of steady-state protein expression that occurs before the upper trap boundary.* We

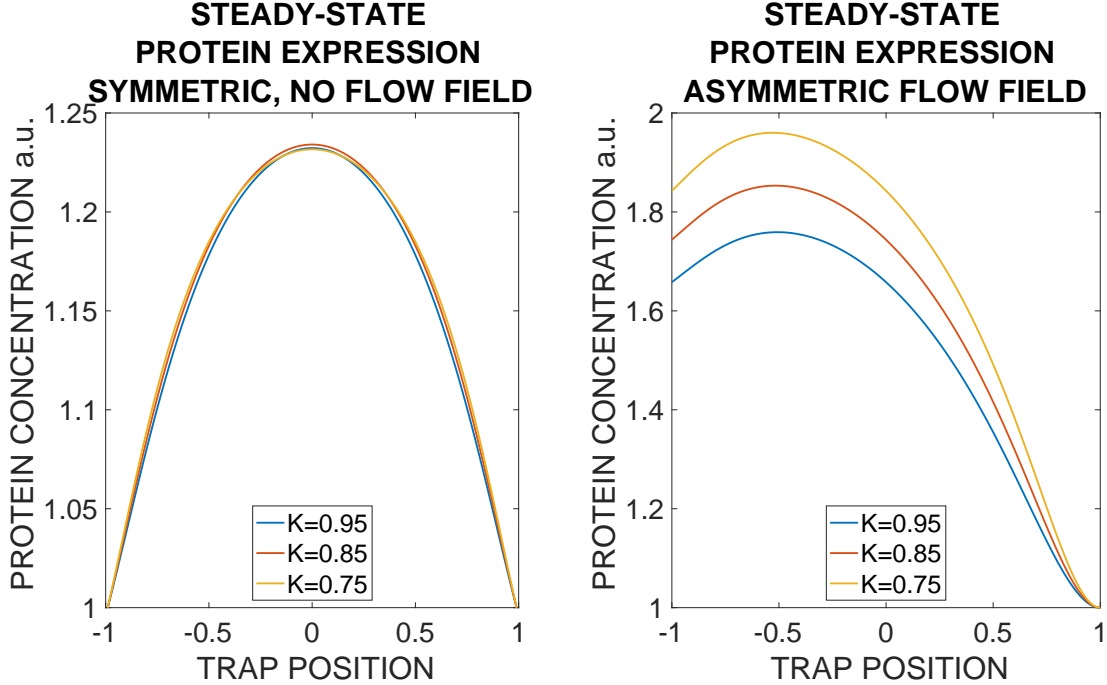


Figure 5.9: **Steady-state protein expression with and without flow fields.** Left sub-plot: normalized steady-state protein expression with no external velocity field and symmetric mother-machine expansion flow (trap center: $y = 0$). Right sub-plot: normalized steady-state protein expression with a bottom-to-top flow field such that the bottom of the trap cell has lab-frame velocity $v = 0$, and all other cells have net lab-frame velocity bottom-to-top (positive direction convention is downwards, and trap center is 0 in both plots). The pressure field p in both cases is $p = 1 - y^2$, where y is the vertical trap position and $y = 1$ is the bottom of the trap. Quadratic pressure field represents growth inhibition to cells in a one-dimensional, back-to-back alignment of cells as developed in Chapter 2. Different values for the K value of the Hill function are shown (K is the value of pressure for which the Hill function is one-half its peak value). In the symmetric flow case, different K values show little change in steady-state protein expression. In the asymmetric flow case, peak value scales inversely with K . The decrease of expression near the upper trap boundary (position $y = -1.0$) in the right sub-plot is observed in the experimental data with the anomalous, non-symmetric cell flow in the open-walled trap (see Figure 5.10). In both plots, $\alpha = 1$, $a = 2$, $n = 2$, $\delta = 0$.

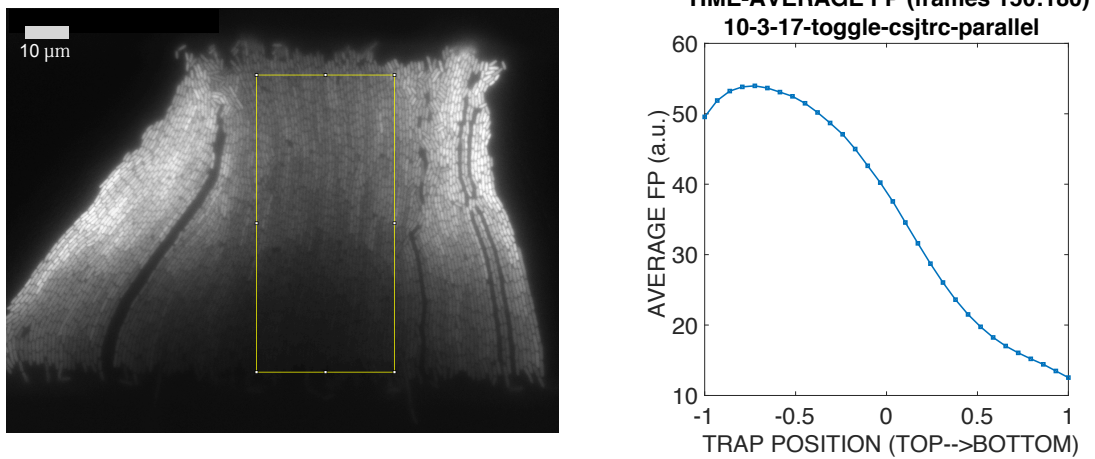


Figure 5.10: **Anomalous protein expression gradient with unidirectional cell flow.** Experimental image and time-average fluorescent protein (FP) expression for a bottom-to-top cell flow anomaly. Left sub-plot: high-resolution FP experimental image for a sender-receiver experiment. Right sub-plot: spatiotemporal average taken over horizontal slices as in Figure 5.7. Curvature in the expression at the top trap position matches the model prediction from Eq. 5.11 with the addition of a uniform velocity field, as seen in Figure 5.9. The unidirectional cell flow anomaly and protein expression profile shown were ubiquitous in experiments. Unpublished image courtesy of the Bennett Lab, Rice University.

believe that this gives substantial strength to this model as an explanation of the data and we comment further on this in the discussion.

5.5 Discussion and conclusions

In this chapter, we have presented a model that attempts to explain anomalous data from experiments. Our model comprises a counterintuitive *increased* protein production rate under *increased* mechanical constraint of bacterial cells growing in open-walled microfluidic traps. We have analyzed a significant volume of experimental data (available from an experimental lab collaboration with Rice University) and have observed, repeatedly, evidently reproducible patterns of anomalous spatiotemporal fluorescent protein (FP) expression under conditions where uniform expression is expected. We believe our model provides strong evidence for the hypothesis that the anomalous FP expression stems directly from an increased rate of production of protein, and we suggest that further experiments should be designed to test the conjecture that this increased rate follows from a mechanical constraint response from the cells.

5.5.1 Bacterial stress response

That bacterial systems can alter their protein expression under conditions of *stress* is well-studied. Environmental perturbations to bacteria that inhibit growth are known to lead to pronounced changes in gene expression [157]. Response pathways can be

induced by growth-inhibiting stresses that include nutritional deprivation, damage to DNA, temperature change and antibiotic exposure, all of which have mechanisms to increase genetic variability through, for example, up-regulation of error-prone DNA polymerases or down-regulation of error-correcting enzymes [56]. For example, a bacterial response pathway known as the “SOS response” is a DNA damage repair network that allows bacteria to withstand toxic DNA damage [110]. Induction of the SOS response can result in cell filamentation, increased levels of mutagenesis, or DNA rearrangements (see [6] and the references therein) .

We presented in this chapter a mathematical model of a conjecture as to the cause of anomalous experimental data. In the experiments we have analyzed, bacterial cells showed significant spatiotemporal variations of protein expression: we find that this is consistent with a “stress” response due to mechanical constraint, as detailed in our model.

Our model, however, is an oversimplification of the cell dynamics: We have omitted stochastic effects, shifts of symmetric center, distributions of transcription/translation delays, asymmetric protein/plasmid partitioning, and discretization of protein/plasmid copy number, for example. These should contribute to spatial smoothing of the response curves (when averaged over an ensemble), but the overall character of the solutions should remain the same.

5.5.2 Synthetic biology context

We find the suggestion that the reproducible, anomalous protein expression we have observed could be *controlled* to be intriguing. If indeed a mechanical inhibition is triggering an increase in protein production rate, one could envision experiments where the mechanical environment is varied so as to induce this response; hence, this could provide a front-end *mechano-biosensory* module that could be connected to other components of a cellular or consortial synthetic circuit. For example, as the result of the $\approx 2X$ increase in protein expression observed in Figure 5.5, a synthetic circuit could be tuned such that this level of expression is sufficient to throw a switch (for example, through an AND-gate topology), and then serve as an input to another part of the genetic or consortial network. This type of connection would then provide bacterial cells with the ability to *sense* their mechanical environment and produce actionable output. We believe this ability has the potential to vastly expand the toolkits available in synthetic biology.

5.5.3 Conclusions

We assert that the anomalous experimental data we have studied has *signal* and it is not *noise*. Further extensions of this model could couple, for example, growth rate variations to mechanical constraint or intra-cell metabolic cost coupled to the pressure field. The parameter δ (the ratio of protein degradation to that of dilution) could have biological significance if, for example, an increased production rate is accompanied by an increased degradation rate. Our model could perhaps be partially

verified (experimentally) by introducing an increased protein degradation rate [63] to see any change of character in the steady-state behavior, and to compare this behavior to that predicted by the model. Our understanding of this phenomena is incomplete; however, we present a quasi-framework from which to study this problem and suggest that further experimental investigations should be designed to further uncover the nature of the anomalies.

Chapter 6

Conclusions

Cellular systems rely on the physical separation of intracellular and extracellular environments, yet cells often exist in close mechanical contact, which gives form and function to cellular organization at several levels of description. Bacterial cells in nature, for example, organize into close-contact communities known as biofilms, a mode of growth that enhances survival in hostile environments, and that allows them to colonize new environments [70]. The prevalence of bacterial biofilms lies in the advantage that bacteria gain from their communal self-organization, and some experiments show that mechanical properties are a key factor in their degree of resistance and protection [43]. The organization, extent, and complexity of mechanical interactions of bacterial systems is largely unknown; however, even at the initiation of biofilm formation, bacteria require mechanical contact with the surface on which the biofilm community is formed [118].

That bacterial communities rely on mechanical interactions in natural environments should be an inspiration for their study in the context of synthetic biology. Indeed, synthetic biology concerns — among many different approaches — the engineering of synthetic circuits designed as simplified testing grounds to help discover how similarly structured natural networks function [113]. In this dissertation, we present models for mechanical interactions of bacteria in the experimental environment of microfluidic traps. We believe that mechanical effects are a rich area of exploration in the context of synthetic biology, and that research should continue to uncover more of their function in biological systems.

In Chapter 2 of this dissertation, we presented an agent-based model (ABM) of a bacterial cell that measures mechanical growth inhibition directly in the model. Our model relies on a mass-spring construction of a cell, whose growth is induced by extending the spring’s *rest-length*; hence, we assert a cell’s *tendency* to grow and not its growth via direct overlap at a predetermined growth rate. This allows us to capture a cell’s resistance to growth in the complex interaction environment typical of bacterial cells in close-packed environments and is in contrast to most published bacterial cell models where cells grow not only irrespectively of their mechanical environment, but also without even measuring it.

In Chapter 3 we presented how a bacterial cell can be conferred a fitness advantage by dynamically changing a purely mechanical property: its aspect ratio. According to our simulation model results, a smaller aspect ratio cell in a columnar structure in a microfluidic trap will have a higher rotational mobility, which will lead to an increased, stochastic, lateral invasion tendency that can eject a neighboring strain

from a mother-cell position (and thus eject it from the column). Continuous assertion of the smaller aspect ratio can lead to a radical change in *strain ratio* in a consortia of cells in a microfluidic trap experiment. This assertion can be induced via cell-cell signaling and can be designed in a negative feedback-loop: one strain can signal another to decrease aspect ratio, which leads to ejection of the signaling strain and a concomitant decrease in signal strength. In this case we see how a purely mechanical property can significantly affect population dynamics in these experiments.

In contrast to the discrete-element nature of the ABM presented in Chapter 2 (and used in Chapter 3), we presented in Chapter 4 a continuum model for cell growth that relies on a *mesoscopic* scale for cells: a scale that is larger than that of an individual cell, but small enough to capture the dynamics of cells grown in close-packing in a microfluidic trap experiment. Our continuum model gives us the advantage of reduced computational complexity while still capturing pressure and velocity fields using a Poisson's equation PDE formulation, and capturing ordering dynamics using modified dynamics equations of liquid-crystal theory.

Compared to the ABM, we do not need to track on the order of $10^3 - 10^4$ individual cells (which significantly reduces the computational load); however, within this model it is challenging to attach, for example, cellular concentrations, since each such scalar field must be advected with the cell flow. Thus, a limitation of our continuum model is that it is difficult to model the stochastic nature and variability of individual cells that are common in biological systems [164]. However, we are able to capture mesoscopic-scale effects. In particular, we demonstrated that experimentally observed cell ordering and persistent *disorder* can be predicted from our model.

In Chapter 5 we presented a model based on a conjecture that mechanical constraint can induce an unexpected *increase* in protein production rate. We formed our conjecture from observations of anomalous experimental fluorescent protein (FP) image data from an array of experiments. In each of the experiments, an increase of protein expression is observed. However, in one particular experiment, we were able to identify that protein *production rate* was being increased, rather than a decrease in the protein *dilution rate*. This is in contrast to our presentation in Chapter 2 (Figure 2.4) where we speculated on how an increase in cell division time could lead to an increase in protein expression. We argued in Chapter 5 that the protein expression anomaly should be investigated further, since it presents a potential opportunity to capture a *mechanical biosensor* as a modular element in the synthetic biology toolkit.

In conclusion, we emphasize that the vast complexity of nature stems — at least partially — from a hierarchical organization of components and layers, and from the bio-molecular interactions between them [30]. Among the interactions, mechanical effects are perhaps least understood; however, the prevalence of cell-cell contacts in nature should invite us to study them deeply, and carefully. Advances in synthetic biology, we believe, will be the result of novel strategies and combinations of techniques from the variety of disciplines of which the field is comprised. We hope to further the study of form, function, complexity, and organization of cells in nature by furthering the study of mechanical interactions of cells in synthetic biology.

Appendix A

Agent based model simulation framework

In this appendix, we state assumptions and details of the agent based model (ABM) simulation framework discussed in Chapter 2.

The material for this chapter stems from previously published content by Winkle et al., in the journal *Physical Biology* [171].

A.1 Non-inertial dynamics assumption

The non-inertial dynamics assumption is satisfied in a regime defined by the value of a fast-scale time constant ξ , which we define with respect to the *inertial* dynamics equations of motion for an isolated cell in our model. We begin with the assumption

that the expansion force on a cell is constant. In our model, this translates to a fixed compression $R - \ell$ of our expansion spring. The validity of this assumption for our simulations is validated by the scale difference between ξ and the discretization time step dt (during which we assume expansion force is constant). We will see that dt is much larger than ξ .

Referring to Eq. (2.1) in Section 2.2, we set $F^{exp} := 2(R - \ell)$ as the constant expansion force. Assuming the mass, m , is constant, the inertial equation of motion for an expanding cell in our model is then:

$$\ddot{\ell} = \frac{F^{exp}}{m} - \frac{\gamma}{m} \dot{\ell}. \quad (\text{A.1})$$

We define $\xi := \frac{m}{\gamma}$ as our fast-scale time constant. Solving this equation with initial velocity $\dot{\ell}(0)$ at time $t = 0$, we obtain the expansion velocity solution,

$$\dot{\ell}(t) = (1 - e^{-\frac{t}{\xi}}) \cdot \frac{F^{exp}}{\gamma} + e^{-\frac{t}{\xi}} \cdot \dot{\ell}(0). \quad (\text{A.2})$$

Thus, for times t under which our constant force assumption holds, the cell expansion velocity is a convex combination of its *terminal velocity* and initial condition. We can now compute an explicit equation for the acceleration of the cell by taking the time derivative of (A.2):

$$\ddot{\ell}(t) = \frac{d}{dt} \dot{\ell}(t) = e^{-\frac{t}{\xi}} \left(\frac{F^{exp}}{m} - \frac{\gamma}{m} \dot{\ell}(0) \right) \quad (\text{A.3})$$

Thus, at $t = 0$, the acceleration is *inertial* and decays exponentially. From equation (A.2), we thus see that *non-inertial dynamics* holds to the extent that F^{exp} can be assumed constant over a time interval t of interest, such that (conservatively) $t \geq 10\xi$ (the exponential decays to $< 10^{-4}$ in this time). If we take the mass of a

cell as $m_{cell} = 10^{-15}$ kg and a fluid damping parameter $\gamma = 10^{-8}$ kg/sec, we have $\xi = 10^{-7}$ sec, or 0.1μ sec. Our computer simulations use a time discretization on the order of $dt = 0.001$ min = 0.06 sec. We then have $dt/\xi > 10^5$.

Thus, during a simulation time interval dt (under which we assume spring rest length and cell mass are constant), our non-inertial dynamics assumption holds. Indeed, assuming the given cell mass and fluid damping values, non-inertial dynamics holds whenever system forces and masses can be assumed constant over time intervals of μ sec or greater.

A.2 Time discretization requirements

Under the non-inertial dynamics assumption (see Section A.1), expansion velocity is proportional to expansion force. In order to prevent overshoot of the expansion velocity for an isolated cell in our simulations, we must observe an upper bound for our discretization time step dt . To see this, we require that $\dot{\ell} < a$. That is, the achieved expansion speed of a cell (starting from rest) should be less than the cell growth rate a . In the RHS of equation (2.2), we set $t = dt$ to perform a forward Euler integration of the rest length (thus = adt). We set $\ell(0) = 0$ and conclude:

$$\dot{\ell} < a \implies \frac{2k}{\gamma}adt < a \implies dt < \frac{\gamma}{2k} = \tau \quad (\text{A.4})$$

Thus, $dt < \tau$ is a necessary condition in our discretization to prevent expansion speed overshoot from rest. Importantly, this directly links the lower range of γ (for fixed k) to computation time: increased computation time is the result of a smaller dt ,

which is required by a smaller γ . Thus, simulations that explore smaller values of τ (equivalently, smaller values of γ for fixed k) will engender higher computational cost under the model described in this paper. However, a more sophisticated, nonlinear control scheme to regulate expansion velocity could be implemented to mitigate this restriction. Here we retained a simple open-loop growth algorithm to validate agreement between theory and our simulation environment, leaving the development of more advanced control algorithms for future work.

A.3 Coupled mass-spring matrix equations

The following analytical framework governs our cell model in a “mother machine” geometry and serves as a basis for verifying our simulation implementation. We now derive the equations of motion for a 1D line of bacterial cells using our model’s mass-spring system. In this derivation, we also include the possibility of *spring damping*, which is a cell-frame dashpot damping added to the expansion spring of our model. We analyze the impact of this damping on the resulting dynamics, and note that Expansion-Overlap-Relaxation model behavior can be obtained via a certain limit.

A.3.1 3-cell mother-machine

We assume a 1D line of 3 cells in a mother machine configuration (see Section 2.3) where cells are in contact pole-to-pole and are constrained to motion in the axial direction only. Since each cell is composed of two axially-independent halves, the

mother machine configuration will identify positions of the contacting cell halves of adjacent cells. The mother cell's trap-walled half will not move in this configuration, thus the equations of motion are determined for the identified positions of each successive cell-cell contact ($i = 1, 2$) and lastly for the free-end cell half ($i = 3$), where i is the index number for the equations given below.

We assume a spring constant k , fluid damping parameter γ_f , and introduce a spring damping parameter γ_s . The matrix-vector equations for an example 3-cell mother-machine system are generated by a stiffness matrix \mathbf{K} and damping matrix $\mathbf{\Gamma}$, which are second-difference matrices that follow from force-balance analysis [151] of the 1D line of masses and springs that represent a back-to-back line of cells in a mother machine using our model. We find

$$\mathbf{K} = \begin{bmatrix} 2 & -1 & 0 \\ -1 & 2 & -1 \\ 0 & -1 & 1 \end{bmatrix}, \quad \text{and} \quad \mathbf{\Gamma} = \begin{bmatrix} 2\gamma_s + \gamma_f & -\gamma_s & 0 \\ -\gamma_s & 2\gamma_s + \gamma_f & -\gamma_s \\ 0 & -\gamma_s & \gamma_s + \gamma_f \end{bmatrix}. \quad (\text{A.5})$$

We let the vector \mathbf{x} represent the positions of the cell-ends, where x_i is the identified position of each successive cell-cell contact ($i = 1, 2$), and x_3 is the position of the free-end cell half, with $\mathbf{x} = 0$ their initial positions. The equations of motion for the coupled system from Newton's 2nd Law are:

$$m\ddot{\mathbf{x}} = -k\mathbf{K}\mathbf{x} - \mathbf{\Gamma}\dot{\mathbf{x}} + k \begin{bmatrix} 0 \\ 0 \\ 1 \end{bmatrix} \text{ at } \quad (\text{A.6})$$

where a is the cell growth rate. Cell 1 is the mother cell and cell 3 the open-end cell in the mother machine. Internal force cancellation of adjacent cell halves results

in the RHS of the above equation having a forcing term only for the outermost cell half of the open-end cell. Expansion forces are then realized through coupling in the stiffness matrix \mathbf{K} . Assuming non-inertial dynamics (see Section A.1) and that $\mathbf{\Gamma}$ is invertible, (A.6) becomes:

$$\dot{\mathbf{x}} = -k\mathbf{\Gamma}^{-1}\mathbf{K}\mathbf{x} + k\mathbf{\Gamma}^{-1} \begin{bmatrix} 0 \\ 0 \\ 1 \end{bmatrix} at \quad (\text{A.7})$$

Now, assuming the matrix product $\mathbf{\Gamma}^{-1}\mathbf{K}$ is diagonalizable with eigenvector matrix \mathbf{Q} , we have the equivalent system of equations in the eigen-basis (using the vector variable \mathbf{y} in this basis):

$$\dot{\mathbf{y}} = -k\mathbf{Q}^{-1}(\mathbf{\Gamma}^{-1}\mathbf{K})\mathbf{Q}\mathbf{y} + k\mathbf{Q}^{-1}\mathbf{\Gamma}^{-1} \begin{bmatrix} 0 \\ 0 \\ 1 \end{bmatrix} at \quad (\text{A.8})$$

If we set $\mathbf{b} := k\mathbf{Q}^{-1}\mathbf{\Gamma}^{-1} \begin{bmatrix} 0 \\ 0 \\ 1 \end{bmatrix}$, with diagonal eigenvalue matrix \mathbf{D} , the diagonalized matrix-vector equation becomes:

$$\dot{\mathbf{y}} = -k\mathbf{D}\mathbf{y} + \mathbf{b}at \quad (\text{A.9})$$

The solution to the diagonalized system now follows as for the single-cell case given by Eq.(2.4) in Section (2.2). For $i \in \{1, 2, 3\}$, we set $\tau_i := \frac{1}{k\mathbf{D}_{ii}}$, and have:

$$\partial_t(e^{\frac{t}{\tau_i}} y_i) = e^{\frac{t}{\tau_i}} b_i at \quad (\text{A.10})$$

Assuming each $y_i(0) = 0$, we then have the diagonalized solutions:

$$y_i = \tau_i b_i a(t - \tau_i + \tau_i e^{-\frac{t}{\tau_i}}) \quad (\text{A.11})$$

$$\dot{y}_i = \tau_i b_i a(1 - e^{-\frac{t}{\tau_i}}) \quad (\text{A.12})$$

We then convert the solution back to the standard basis using $\mathbf{x} = \mathbf{Q}\mathbf{y}$ and $\dot{\mathbf{x}} = \mathbf{Q}\dot{\mathbf{y}}$. We thus have that the motion of each cell in the mother machine is a linear combination of eigen-modes of the matrix product $\Gamma^{-1}\mathbf{K}$. We now explore the effects of the spring damping on the equations of motion.

A.3.2 No spring damping

With no spring damping, the $\mathbf{\Gamma}$ matrix is diagonal and we can replace it with a scalar parameter γ . \mathbf{Q}, \mathbf{D} are then the eigenvector, eigenvalue matrices of \mathbf{K} , and we set:

$$\tau_i := \frac{\gamma}{kD_{ii}}, \quad b_i := \frac{k\mathbf{Q}_{i3}^{-1}}{\gamma} \quad (\text{A.13})$$

The solution is then given by (A.11 - A.12). We find that the steady-state solutions to spring compression follow a quadratic profile vs. cell position in the mother machine. This is readily derived without the matrix equations by analyzing the the force balance necessary to achieve linear growth in cell-end speeds towards the open end of the mother machine. If we assume each cell expands (in the cell's frame of reference) at a constant speed v , then each successive cell-end will move (in the laboratory frame of reference) at $i \cdot v$, where $i \in 1..N$ and N is the number of cells in the mother machine, and $i = 1$ is the mother cell. Since the end-cell half of cell N is independent and we are under non-inertial dynamics, this end-cell half must apply a force of $\gamma N v$

to achieve speed Nv in the laboratory frame. Each cell expands with symmetric force, thus cell end $(N - 1)$, which moves at $(N - 1)v$ must have (by algebraic addition of forces from adjacent cell halves): $\gamma C_{N-1}v - \gamma Nv = \gamma(N - 1)v$, where C_{N-1} is the unknown scale factor for the penultimate cell. Clearly, $C_{N-1} = N + (N - 1)$.

Continuing in this manner towards the mother cell, we see that the successive cell force differences lead to a quadratic expression for cell compression vs. cell position. An example plot of the steady-state cell compression for $N = 10$ cells is shown in Figure(A.1), where the quadratic profile is evident.

A.3.3 Large spring damping

With spring damping much larger than fluid damping, we then have for the damping matrix:

$$\mathbf{\Gamma} = \gamma_s \begin{bmatrix} 2 & -1 & 0 \\ -1 & 2 & -1 \\ 0 & -1 & 1 \end{bmatrix}, \quad (\text{A.14})$$

We note in this case that $\mathbf{\Gamma} = \gamma_s \mathbf{K}$. Importantly, increasing spring damping relative to fluid damping leads to *uniform dynamics* of all cells in the mother machine. However, to maintain responsiveness, the spring constant k must scale with spring damping. For example, in the isolated cell case, spring damping and fluid damping reference frames are the same, and the damping parameters add such that $\gamma = \gamma_f + \gamma_s$ to define τ in Eq. (2.4). Thus, to maintain the same first-order dynamics, k must scale with the resulting additive γ such that $\tau = \frac{\gamma}{k}$ remains constant. We find that, in the limit of $k, \gamma_s \rightarrow \infty$, while $\frac{\gamma_s}{k} = \text{constant}$ we recover the behavior of the

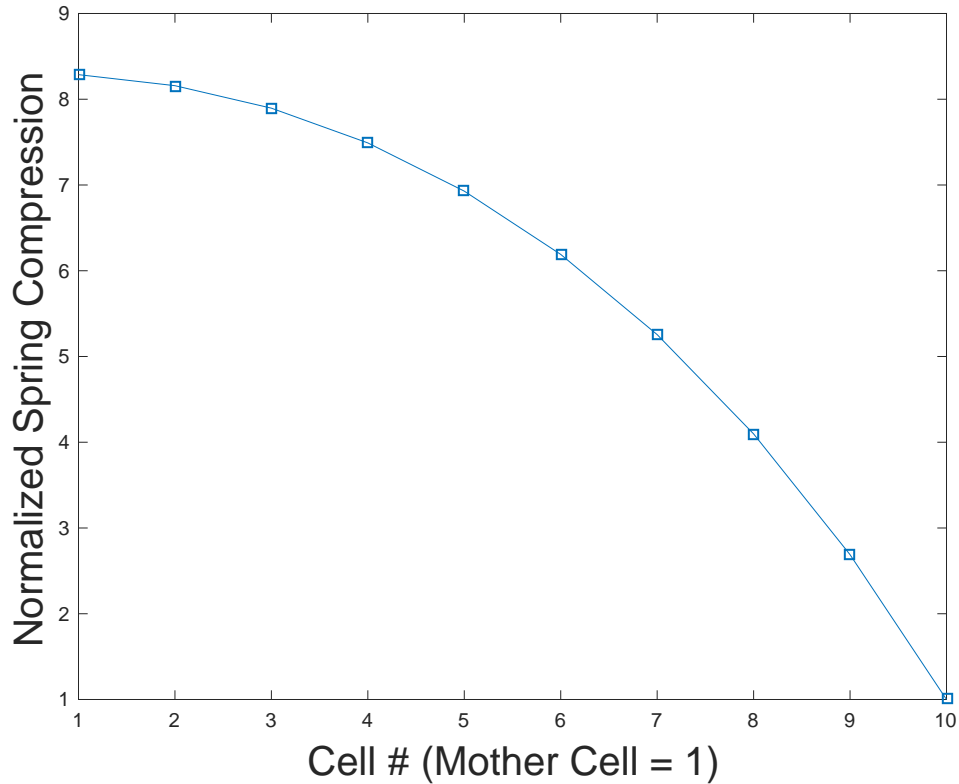


Figure A.1: Normalized steady-state cell compression for $N = 10$ cells in a mother-machine. The quadratic profile is predicted by the analytical solution.

EOR model described in Section 2.2, where cells achieve growth rates uniformly. We believe inclusion of γ_s and a higher value of k than used in our simulations (see Section A.6) would more accurately model biological cell growth (resulting in faster transient behavior and more uniform dynamics). Our model thus serves as an incomplete realization of the biology, while serving as a generalization of an EOR model that includes mechanical constraint measurement.

A.4 Simulation details

A.4.1 Chipmunk 2D simulation environment

We use the open-source physics engine `Chipmunk 2D` (see [3]) to define cell objects and traps to simulate interactions and dynamics of cell consortia. The use of this engine by `gro` (see [79]) was the original inspiration for its use in our model. We detail in this section our simulation loop algorithm and the relevant components from `Chipmunk 2D`.

A simulation step consists of the following. The 2D physics engine is assumed to have just completed a time-step. An un-ordered list structure of cell objects is then traversed to determine if a cell should divide or be removed from the simulation (sub-routines would either add a new daughter cell or remove the cell from the list, respectively; see subsection below for the cell division algorithm). Each remaining cell's physics model is then updated as follows:

1. The current cell length ℓ is computed by subtracting the positions of the cell ends, which are obtained by querying the respective components from the 2D physics engine. The current spring compression is then computed by subtracting the cell length from the spring rest length.
2. As a function of the current spring compression, a growth rate is selected for the following time step (the growth rate may also be constant, i.e., independent of compression, or in general, it may be set algorithmically by the user). The growth rate is then asserted in the discrete-time simulation by an increase of

the spring rest length, with increment $dR := a \cdot dt$, where a is the current growth rate and dt is the discrete time step. Thus, $R \leftarrow R + dR$.

3. The cell expansion force is computed as $F^{exp} = k(R - \ell)$ and this is set for each cell half independently.
4. The 2D physics engine is stepped. This consists of 3 principal parts within the **Chipmunk** 2D software:
 - (a) The current timestep velocity \mathbf{v}_i is forward-integrated to determine new positions for all objects i in the space. Namely, each cell end is extended by $\mathbf{v}_i \cdot dt$, where \mathbf{v}_i is computed at the end of the previous physics engine time step (or otherwise altered by the user in steps 1-3 above). In general, cells will *not overlap* each other as the result of a position integration. Rather, objects in contact will move together with velocities that were resolved in the previous time step (in part C below) by the physics engine via collision dynamics.
 - (b) The force programmed in item (3) above is used to determine new interaction velocities for all objects in the space. The cell halves' velocities in the non-inertial regime are computed directly by $\hat{\mathbf{v}} = \frac{\mathbf{F}^{exp}}{\gamma}$. (The previous velocity of the objects is set to zero in the non-inertial regime). In general this velocity $\hat{\mathbf{v}}$ will not actually be achieved by the cell halves. The impulse solver in part C will adjust velocities and positions based on collision dynamics of objects in the space.
 - (c) The 2D physics engine's impulse solver iterates over the space to resolve

competing object velocities when two objects are in direct contact. The impulse solver adds impulses to each object and the resulting actual velocities of cell halves are computed and will be used in the following timestep’s position integration.

We note that collision dynamics is chosen to model cell-cell interactions simply because this is how interaction dynamics are modeled in Chipmunk 2D. In Chipmunk 2D, two cells that are in contact will initiate a “collision arbitration” (which is a bit of a misnomer in our case since the objects are not ballistically colliding, but are, typically, only in boundary surface contact). Each pairwise contact, however, is resolved as an inelastic collision in the Chipmunk 2D code. Although inelastic collisions are inconsistent with non-inertial dynamics, we concluded that it is a reasonable implementation and, in fact, would be very time-consuming to modify.

A.4.2 Cell division algorithm

A cell divides when it reaches a volume of approximately $\ell = 4.5$ microns. Upon division, a ratio r is randomly chosen from a uniform distribution in $[0.4, 0.6]$, and daughter cell A is assigned initial length $r \cdot \ell$, while daughter cell B is assigned initial length $(1 - r) \cdot \ell$. Any contents of the mother cell, if explicitly modeled, are divided between the two daughter cells according to the same ratio r . To ensure continuity of expansion force across cell divisions, each daughter cell inherits the parent’s spring compression. Since cells in our model are constructed in two halves, we assert continuity of cell expansion velocity by assigning to daughter cells A and B

a center-of-mass velocity equal to the corresponding cell-half velocity of the parent (both in the lab frame). Thus each daughter cell moves apart from the other as the two halves of the parent did before division. This is necessary since, at the time cell divisions are created, cells in the model have not yet integrated positions based on their current cell halves' velocities, as resolved by the Chipmunk impulse solver (see item (4) in the previous subsection).

A.5 Ratchet algorithm for cell back-filling

The ratchet algorithm is used to mitigate on-axis *cell compression*, which we realize may not be clearly differentiated from use of the term *spring compression* in our cell model and writeup. To add clarification, by *cell compression* we refer to the actual potential shortening of cell length ℓ , which may occur if neighboring cells exert an on-axis compressive force that is larger than the cell's current growth (spring expansion) force in a time step. This would result in a compression of the cell length since the two cell-halves are axially independent in this case. The ratchet algorithm prevents excessive *cell compression*. By back-filling with a symmetric contact surface after incremental growth steps (i.e. ratchets, which are counted by the integer n , below), we limit possible compression to a small amount, which is a programmable parameter that is adjustable by the user (we set it to 0.1 micron). We found this was much simpler and more robust than implementing a nonlinear spring, although the results would be similar. The idea is that a cell should not be compressed to a length much smaller than a previously established length. We note that *spring compression*

is a key component of our cell model (specifically, it is our measure of mechanical constraint), and does not (normally) reflect a cell becoming smaller in length (i.e., *cell compression*). Our cell model’s spring compression will increase when a cell is prevented from growing via mechanical interactions as developed in Sections 2.2 and 2.3 in our manuscript. Such increase can (and normally does) occur even when the cell is continuously expanding.

Thus, to ensure that axial compression is accounted for in our model, we employ an algorithm to back-fill contact area to each cell half, such that contraction of a cell is limited to a compression gap and ratchet step, which we now detail. Each cell half is constructed as in Figure 2.1 with a rectangular center and attached “frontside pole” that defines the frontal contact area of a cell. In addition, however (and not shown in Figure 2.1), there is a “backside pole” that is attached to a ratchet-extended rectangular area, which is designed to keep the backside pole just inside the frontside pole of the other half. Usually, this backside pole contact surface is *transparent* to collision dynamics of a cell, since it lies inside the outer contact hull of the cell. However, in case a cell becomes subject to constricting axial forces (from other cells or trap walls) larger than cell expansion forces, the two halves will contract, but only until the backside poles of each half align with the frontside poles of the other, at which time the cell acts as a rigid body not subject to further compression.

As a cell expands, this backside contact area must be extended to limit the amount of compression before the poles are aligned from the two halves (thus forming the rigid body). We employ a ratchet algorithm to achieve this extension, such that the

backside pole is extended once the cell length passes a ratchet step r_s . The algorithm is summarized as follows:

Data: current cell length ℓ ; current ratchet count n ; ratchet step r_s ; ratchet gap r_g ;
Result: on next ratchet: back-filled cell contact area to $\ell - r_g$;
Initialize each cell on birth with backside pole r_g away from frontside pole of other half and set $n = 0$;
For every cell in every time step:
if ($\ell > (n + 1)r_s + r_g$) **then**
 | back-fill cell pole contact area to $\ell - r_g$ for each cell half;
 | $n \leftarrow n + 1$;
else
 | continue;
end

A.6 Table of parameter values

PARAMETER	SIMULATION VALUE	SCALE	PHYSICAL VALUE
dt	0.001 min	1	0.06 sec
m	1×10^{-10}	1×10^{-5} kg	1×10^{-15} kg
γ	60 min^{-1}	1×10^{-5} kg	1×10^{-5} kg sec $^{-1}$
k	3600 min^{-2}	1×10^{-5} kg	1×10^{-5} kg sec $^{-2}$
$\xi := m\gamma^{-1}$	1.7×10^{-12} min	1	1×10^{-10} sec
$2\tau := \gamma k^{-1}$	0.017 min	1	1 sec

Simulation values are computed by dividing the physical value by the scale for each parameter and converting units appropriately. We used mass m of a bacterial cell as given in [2], and dimensionless mass units in our simulations. The scale value for

mass is chosen to normalize k and γ to 1.0 in SI units. Our physical value for k is a computationally realizable estimate to model turgor pressure. We chose γ such that $2\tau = 1$ sec. In Figure 2.1, panels (b),(c), we also used a value of 10γ for comparison of the cell dynamics. Both k and γ simulation values use dimensionless mass units. Two time constants are shown for reference: ξ defines a scale for non-inertial dynamics as in A.1, and τ defines the first-order growth dynamics of our cell model, as derived in 2.2.3. We note that γ overestimates a physical value, but it is chosen as a convenient value for computational purposes (see A.2).

Appendix B

Diffusion Signalling Model

In this appendix, we discuss the signaling model details used in Chapter 3 to effect dynamic aspect ratio control. We describe a diffusion model for QS-HSL in an ABM simulation of bacterial cells in an open-walled micro-fluidic device.

B.1 Mathematical model

B.1.1 HSL ODE

We use as a model (see [32], supplementary material) the following ODE for H_i , the HSL concentration *inside* our bacterial cell:

$$\frac{d}{dt}H_i = \phi R - D_c(H_i - H_e) - d_c H_i, \quad (\text{B.1})$$

where ϕ is the production rate of HSL from its synthase concentration R (if an HSL diffusing into/out of the cell is not synthesized in the cell, this rate is 0), D_c is the diffusion rate across the cell membrane to/from the extracellular fluid, and d_c is the active degradation rate of HSL inside the cell. Dilution of HSL inside of the cell is implicit with growth and division in the ABM and thus is not present here (if the dilution rate \gg degradation, this term will be zero).

We discretize the diffusion of HSL across the cell membrane in time. We use the cell center and the center of each pole as the points of spatial diffusion of the cell to/from the surrounding fluid. This simplification is justified by the extremely fast diffusion of HSL in the media, as compared to the growth rate of the cell. Spatial discretization of the diffusion grid will require rounding the diffusion center locations to the nearest grid point, thus $(x, y) \rightarrow (i, j)$, where the latter is the nearest grid location by some metric (slight abuse of notation for i – as a subscript for the concentration it represents *internal*, not a spatial index). We use an implicit time discretization, notating the intra-cell HSL concentration at the previous time step $n - 1$ to be H_i^{n-1} and the to-be computed concentration at the current time step n as H_i^n . The per-cell discretized equation is then (using time-step dt):

$$H_i^n - H_i^{n-1} = dt[\phi R - D_c(H_i^n - H_e^n) - d_c H_i^n]. \quad (\text{B.2})$$

The discretized equation for the *external* HSL concentration at the grid point (i, j) is:

$$H_e^n - H_e^{n-1} = dt[D_c(H_i^n - H_e^n)]. \quad (\text{B.3})$$

This is a coupled system of equations for H_i^n, H_e^n . We rearrange:

$$\begin{aligned} [1 + dt(D_c + d_c)]H_i^n - [dtD_c]H_e^n &= H_i^{n-1} + dt\phi R, \\ [-dtD_c]H_i^n + [1 + dtD_c]H_e^n &= H_e^{n-1}. \end{aligned} \tag{B.4}$$

This 2x2 system can be solved easily, with each time-step only updating the RHS. Thus the matrix can be factored once for fast computation each time step (assuming dt, D_c, d_c constant).

B.1.2 Time-stepping algorithm

The diffusion model will be coupled into the ABM simulations, which also time-step a 2D physics engine that updates positions, angles, velocities, etc.. of cells. There will be an independent “grid layer” of HSL diffusion for each HSL molecule diffused. We assume for simplicity that the HSLs diffuse independently and do not otherwise interact. The high-level algorithm for the time-stepping of the ABM simulations is:

1. We assume the 2D physics engine and diffusion grid(s) have been stepped from the previous time iteration. We read and update the cell positions, lengths, etc..., and for each cell we extract the local external concentration of HSL at the *cell center*. This value will be linearly interpolated if the cell-center does not align on a diffusion grid point. We scale the concentration read by the updated length of the cell (normalized to volume units) to obtain the average external concentration of HSL for the entire cell.

2. Non-diffusion protein ODE's are updated according to their respective governing equations for each cell (using the previous time-step for HSL concentrations). For example, the HSL synthase concentration R is updated according to its ODE. This sets all values for the RHS of Eq. *B.4* to be solved for the current time step.
3. Eq. *B.4* is solved, and the resulting local external HSL concentration is rescaled to a diffusion grid point and written to the grid. The internal HSL concentration and all other protein concentrations are saved per cell in the ABM model (including possibly into queue data structures for delay equations).
4. The diffusion grid is time-stepped using an implicit solver. Depending on the target processor for the simulation, diffusion stepping will be performed in parallel for each HSL grid and the 2D physics engine for optimal efficiency. We then loop-back to the first step and continue.

B.1.3 Calculation for an explicit scheme

We rule out using an explicit (forward) Euler scheme for time-discretization as it would place a burden on the minimum time-step needed for our spatial resolution. We calculate the space-step resolution for an expected diffusion coefficient D and time step dt by the requirement for explicit-Euler:

$$D \frac{dt}{\Delta x^2} < 1/2. \tag{B.5}$$

We use an est. value for D (see [32], SI) as $D = 3e4\mu m^2/min$ and a usual lower-bound time step for 2D physics of $dt = 0.001$ min. This sets a spatial resolution of

$\Delta x > \sqrt{2Ddt} = 7.7\mu\text{m}$, which is too coarse. Likewise, to reach a spatial resolution of $1/2 \mu\text{m}$ would require $dt < 0.125/D = 4.2\text{e-}6$ min, which is prohibitively small (a factor of $1/200$ compared to $dt=0.001$). Thus, we use an implicit scheme.

B.2 Numerical simulations

We implement the implicit scheme for diffusion in the PDE solver software *Fenics* in order to take advantage of its integrated sparse linear-algebra solver backends and of its visualization tools (2D scalar fields are easily written to file for display in Paraview software). We use a spatial resolution of $1/2 \mu\text{m}$ (recalling the extremely fast diffusion rate compared to cell growth rate) given a bacterial cell width of $1\mu\text{m}$. An example trap size of $40\mu\text{m} \times 160\mu\text{m}$ would then lead to approx. $80 \times 320 = 25600$ nodes (easily manageable for a sparse system).

Bibliography

- [1] http://jun.ucsd.edu/mother_machine.php.
- [2] Cell biology by the numbers. <http://book.bionumbers.org>.
- [3] Chipmunk 2d game dynamics, version 7. Howling Moon Software; <http://chipmunk-physics.net/>.
- [4] Rafael D. Acemel, Fernando Govantes, and Alejandro Cuetos. Computer simulation study of early bacterial biofilm development. *Sci. Rep.*, 8(1):1–9, 2018.
- [5] R. Aditi Simha and Sriram Ramaswamy. Hydrodynamic fluctuations and instabilities in ordered suspensions of self-propelled particles. *Phys. Rev. Lett.*, 89(5):058101, 2002.
- [6] Abram Aertsen and Rob Van Houdt. An SOS response induced by high pressure in *Escherichia coli*. *J. Bacteriol.*, 186(18):6133–6141, 2004.
- [7] Christina M. Agapakis. Designing synthetic biology. *ACS Synth. Biol.*, 3(3):121–128, 2014.
- [8] Martin S. Alnæs. *UFL: a Finite Element Form Language*, chapter 17. Springer, 2012.
- [9] Hal Alper and Gregory Stephanopoulos. Engineering for biofuels: Exploiting innate microbial capacity or importing biosynthetic potential? *Nat. Rev. Microbiol.*, 7(10):715–723, 2009.
- [10] Ariel Amir. Cell Size Regulation in Bacteria. *Phys. Rev. Lett.*, 112(20):208102, 2014.
- [11] Martyn Amos. Population-based microbial computing: A third wave of synthetic biology? *Int. J. Gen. Syst.*, 43(7):770–782, 2014.

- [12] Steve Ashby, Pete Beckman, Jackie Chen, Phil Colella, Bill Collins, Dona Crawford, Jack Dongarra, Doug Kothe, Rusty Lusk, Paul Messina, and Others. The opportunities and challenges of exascale computing. *Summ. Rep. Adv. Sci. Comput. Advis. Comm. Subcomm.*, pages 1–77, 2010.
- [13] William Bacchus and Martin Fussenegger. Engineering of synthetic intercellular communication systems. *Metab. Eng.*, 16(1):33–41, 2013.
- [14] Rajesh Balagam and Oleg A. Igoshin. Mechanism for Collective Cell Alignment in Myxococcus xanthus Bacteria. *PLoS Comput. Biol.*, 11(8):1–21, 2015.
- [15] Geoff Baldwin. *Synthetic Biology - A Primer (Revised Edition)*, volume Revised ed. 2016.
- [16] Diego Barcena Menendez, Vivek Raj Senthivel, and Mark Isalan. Sender-receiver systems and applying information theory for quantitative synthetic biology. *Curr. Opin. Biotechnol.*, 31:101–107, 2015.
- [17] Bonnie L. Bassler and Richard Losick. Bacterially Speaking. *Cell*, 125(2):237–246, 2006.
- [18] Jacob Beal, Robert Sidney Cox, Raik Grünberg, James McLaughlin, Tramy Nguyen, Bryan Bartley, Michael Bissell, Kiri Choi, Kevin Clancy, Chris Macklin, Curtis Madsen, Goksel Misirli, Ernst Oberortner, Matthew Pocock, Nicholas Roehner, Meher Samineni, Michael Zhang, Zhen Zhang, Zach Zundel, John H. Gennari, Chris Myers, Herbert Sauro, and Anil Wipat. Synthetic Biology Open Language (SBOL) Version 2.1.0. *J. Integr. Bioinform.*, 13(3):30–132, 2016.
- [19] Robert Belas. Biofilms, flagella, and mechanosensing of surfaces by bacteria. *Trends Microbiol.*, 22(9):517–527, 2014.
- [20] Matthew R. Bennett and Jeff Hasty. Microfluidic devices for measuring gene network dynamics in single cells. *Nat Rev Genet*, 10(9):628–638, 2009.
- [21] János Bérdy. Thoughts and facts about antibiotics: Where we are now and where we are heading. *J. Antibiot. (Tokyo)*, 65(8):385–395, 2012.
- [22] Philip Bittihn, M. Omar Din, Lev S. Tsimring, and Jeff Hasty. Rational engineering of synthetic microbial systems: from single cells to consortia. *Curr. Opin. Microbiol.*, 45:92–99, 2018.

- [23] Denis Boyer, William Mather, Octavio Mondragón-Palomino, Sirio Orozco-Fuentes, Tal Danino, Jeff Hasty, and Lev S Tsimring. Buckling instability in ordered bacterial colonies. *Phys. Biol.*, 8(2):026008, 2011.
- [24] Robert W. Bradley, Martin Buck, and Baojun Wang. Recognizing and engineering digital-like logic gates and switches in gene regulatory networks. *Curr. Opin. Microbiol.*, 33:74–82, 2016.
- [25] Rainer Breitling and Eriko Takano. Synthetic biology advances for pharmaceutical production. *Curr. Opin. Biotechnol.*, 35:46–51, 2015.
- [26] Mette Burmølle, Dawei Ren, Thomas Bjarnsholt, and Søren J. Sørensen. Interactions in multispecies biofilms: Do they actually matter? *Trends Microbiol.*, 22(2):84–91, 2014.
- [27] Antonio Carvajal-Rodriguez. Simulation of Genes and Genomes Forward in Time. *Curr. Genomics*, 11(1):58–61, 2010.
- [28] P. M. Chaikin and T. C. Lubensky. *Principles of Condensed Matter Physics*. Cambridge University Press, 1995.
- [29] Fred Chang and Kerwyn Casey Huang. How and why cells grow as rods. *BMC Biol.*, 12:54, 2014.
- [30] Kevin Channon, Elizabeth HC Bromley, and Derek N. Woolfson. Synthetic biology through biomolecular design and engineering. *Curr. Opin. Struct. Biol.*, 18(4):491–498, 2008.
- [31] Akhilesh Kumar Chaurasia, Tapan Kumar Adhya, and Shree Kumar Apte. Engineering bacteria for bioremediation of persistent organochlorine pesticide lindane (γ -hexachlorocyclohexane). *Bioresour. Technol.*, 149:439–445, 2013.
- [32] Ye Chen, Jae Kyoung Kim, Andrew J Hirning, Krešimir Josić, and Matthew R Bennett. Emergent genetic oscillations in a synthetic microbial consortium. *Science (80-.)*, 349(6251):986–989, 2015.
- [33] Yu Yu Cheng, Andrew J. Hirning, Krešimir Josić, and Matthew R. Bennett. The Timing of Transcriptional Regulation in Synthetic Gene Circuits. *ACS Synth. Biol.*, 6(11):1996–2002, 2017.
- [34] HoJung Cho, Henrik Jönsson, Kyle Campbell, Pontus Melke, Joshua W. Williams, Bruno Jedynek, Ann M. Stevens, Alex Groisman, and Andre Levchenko. Self-organization in high-density bacterial colonies: Efficient crowd control. *PLoS Biol.*, 5(11):2614–2623, 2007.

- [35] Koon Jiew Chua, Wee Chiew Kwok, Nikhil Aggarwal, Tao Sun, and Matthew Wook Chang. Designer probiotics for the prevention and treatment of human diseases. *Curr. Opin. Chem. Biol.*, 40:8–16, 2017.
- [36] Brady F. Cress, Emmanouil A. Trantas, Filippos Ververidis, Robert J. Linhardt, and Mattheos A.G. Koffas. Sensitive cells: Enabling tools for static and dynamic control of microbial metabolic pathways. *Curr. Opin. Biotechnol.*, 36:205–214, 2015.
- [37] Peter Dabrock. Playing god? synthetic biology as a theological and ethical challenge. *Syst. Synth. Biol.*, 3(1):47–54, 2009.
- [38] Lance A. Davidson. The Physical Mechanical Processes that Shape Tissues in the Early Embryo. *Cell. Biomol. Mech. Mechanobiol.*, 4:71–97, 2011.
- [39] P. G. de Gennes and J. Prost. *The Physics of Liquid Crystals*. International Series of Monogr. Clarendon Press, 1995.
- [40] Morgan Delarue, Jörn Hartung, Carl Schreck, Pawel Gniewek, Lucy Hu, Stephan Herminghaus, and Oskar Hallatschek. Self-driven jamming in growing microbial populations. *Nat. Phys.*, 12:762, 2016.
- [41] Benjamin J. Des Soye, Jaymin R. Patel, Farren J. Isaacs, and Michael C. Jewett. Repurposing the translation apparatus for synthetic biology. *Curr. Opin. Chem. Biol.*, 28:83–90, 2015.
- [42] M. Doi and S.F. Edwards. *The Theory of Polymer Dynamics*. International series of monographs on physics. Clarendon Press, 1988.
- [43] Carine Douarche, Jean Marc Allain, and Eric Raspaud. Bacillus subtilis Bacteria Generate an Internal Mechanical Force within a Biofilm. *Biophys. J.*, 109(10):2195–2202, 2015.
- [44] Dirk Drasdo, Stefan Hoehme, and Michael Block. On the role of physics in the growth and pattern formation of multi-cellular systems: What can we learn from individual-cell based models? *J. Stat. Phys.*, 128(1-2):287–345, 2007.
- [45] M B Elowitz, A J Levine, E D Siggia, and P S Swain. Stochastic gene expression in a single cell. *Science*, 297(5584):1183–1186, 2002.
- [46] Michael B. Elowitz and Stanislas Leibler. A synthetic oscillatory network of transcriptional regulators. *Nature*, 403(6767):335–338, 2000.

- [47] Daniel S. Esser, Johan H. J. Leveau, and Katrin M. Meyer. Modeling microbial growth and dynamics. *Appl. Microbiol. Biotechnol.*, 99(21):8831–8846, 2015.
- [48] F. D C Farrell, O. Hallatschek, D. Marenduzzo, and B. Waclaw. Mechanically driven growth of quasi-two-dimensional microbial colonies. *Phys. Rev. Lett.*, 111(16):1–5, 2013.
- [49] Fred D. Farrell, Matti Gralka, Oskar Hallatschek, and Bartłomiej Waclaw. Mechanical interactions in bacterial colonies and the surfing probability of beneficial mutations. *J. R. Soc. Interface*, 14(131):20170073, 2017.
- [50] Nariman Farsad, H. Birkan Yilmaz, Andrew Eckford, Chan-Byoung Chae, and Weisi Guo. A Comprehensive Survey of Recent Advancements in Molecular Communication. *IEEE Commun. Surv. Tutorials*, 18(3):1887–1919, 2016.
- [51] Fahim Farzadfard and Timothy K Lu. Genomically encoded analog memory with precise in vivo DNA writing in living cell populations. *Science (80-.)*, 346(6211), 2014.
- [52] María Elena Fernández-Sánchez, Sandrine Barbier, Joanne Whitehead, Gaëlle Béalle, Aude Michel, Heldmuth Latorre-Ossa, Colette Rey, Laura Fouassier, Audrey Claperon, Laura Brullé, Elodie Girard, Nicolas Servant, Thomas Rio-Frio, Hélène Marie, Sylviane Lesieur, Chantal Housset, Jean-Luc Gennisson, Mickaël Tanter, Christine Ménager, Silvia Fre, Sylvie Robine, and Emmanuel Farge. Mechanical induction of the tumorigenic β -catenin pathway by tumour growth pressure. *Nature*, 523(7558):92–95, 2015.
- [53] Michael A. Fischbach and Julia A. Segre. Signaling in Host-Associated Microbial Communities. *Cell*, 164(6):1288–1300, 2016.
- [54] Hans-Curt Flemming, Jost Wingender, Ulrich Szewzyk, Peter Steinberg, Scott A Rice, and Staffan Kjelleberg. Biofilms an emergent form of bacterial life. *Nat. Rev. Microbiol.*, 14:563, 2016.
- [55] Tyler J. Ford and Pamela A. Silver. Synthetic biology expands chemical control of microorganisms. *Curr. Opin. Chem. Biol.*, 28:20–28, 2015.
- [56] Patricia L. Foster. Stress-induced mutagenesis in bacteria. *Crit. Rev. Biochem. Mol. Biol.*, 42(5):373–397, 2007.
- [57] Leon Furchtgott, Ned S. Wingreen, and Kerwyn Casey Huang. Mechanisms for maintaining cell shape in rod-shaped gram-negative bacteria. *Mol. Microbiol.*, 81(2):340–353, 2011.

- [58] Timothy S. Gardner, Charles R. Cantor, and James J. Collins. Construction of a genetic toggle switch in *Escherichia coli*. *Nature*, 403(6767):339–342, 2000.
- [59] L. Goers, P. Freemont, and K. M. Polizzi. Co-culture systems and technologies: taking synthetic biology to the next level. *J. R. Soc. Interface*, 11(96):20140065–20140065, 2014.
- [60] Mariana Gómez-Schiavon and Hana El-Samad. Complexity-aware simple modeling. *Curr. Opin. Microbiol.*, 45:47–52, 2018.
- [61] Thomas E. Gorochowski. Agent-based modelling in synthetic biology. *Essays Biochem.*, 60(4):325–336, 2016.
- [62] M. A. A. Grant, B. Wac aw, R. J. Allen, and P. Cicuta. The role of mechanical forces in the planar-to-bulk transition in growing *Escherichia coli* microcolonies. *J. R. Soc. Interface*, 11(97):20140400–20140400, 2014.
- [63] Chris Grilly, Jesse Stricker, Wyming Lee Pang, Matthew R. Bennett, and Jeff Hasty. A synthetic gene network for tuning protein degradation in *Saccharomyces cerevisiae*. *Mol. Syst. Biol.*, 3(127):1–6, 2007.
- [64] Volker Grimm, Eloy Revilla, Uta Berger, Florian Jeltsch, Wolf M. Mooij, Steven F. Railsback, Hans-Hermann Thulke, Jacob Weiner, Thorsten Wiegand, and Donald L. DeAngelis. Pattern-Oriented Modeling of Agent Based Complex Systems: Lessons from Ecology. *Science (80-.)*, 310(5750):987–991, 2005.
- [65] Colleen M. Grogan. Public engagement and the importance of content, purpose, and timing. *Hastings Cent. Rep.*, 44(6):S40–S42, 2014.
- [66] Jeremy Gunawardena. Models in biology accurate descriptions of our pathetic thinking. *BMC Biol.*, 12(1):29, 2014.
- [67] Martín Gutiérrez, Paula Gregorio-Godoy, Guillermo Pérez Del Pulgar, Luis E. Munoz, Sandra Sáez, and Alfonso Rodríguez-Patón. A New Improved and Extended Version of the Multicell Bacterial Simulator gro. *ACS Synth. Biol.*, 6(8):1496–1508, 2017.
- [68] Viktor Haellman and Martin Fussenegger. Synthetic biology – Engineering cell-based biomedical devices. *Curr. Opin. Biomed. Eng.*, 4:50–56, 2017.
- [69] Stephen J. Hagen. Exponential growth of bacteria: Constant multiplication through division. *Am. J. Phys.*, 78(12):1290–1296, 2010.

- [70] Luanne Hall-Stoodley, J. William Costerton, and Paul Stoodley. Bacterial biofilms: From the natural environment to infectious diseases. *Nat. Rev. Microbiol.*, 2(2):95–108, 2004.
- [71] Jeff Hasty, David McMillen, and J. J. Collins. Engineered gene circuits. *Nature*, 420(6912):224–230, 2002.
- [72] Hamed Hatami-Marbini and Mohammad R. K. Mofrad. *Cytoskeletal Mechanics and Cellular Mechanotransduction: A Molecular Perspective*, pages 3–27. Springer Berlin Heidelberg, Berlin, Heidelberg, 2011.
- [73] Stephanie G. Hays, William G. Patrick, Marika Ziesack, Neri Oxman, and Pamela A. Silver. Better together: Engineering and application of microbial symbioses. *Curr. Opin. Biotechnol.*, 36:40–49, 2015.
- [74] Stefan Hoehme and Dirk Drasdo. A cell-based simulation software for multicellular systems. *Bioinformatics*, 26(20):2641–2642, 2010.
- [75] J V Holtje. Growth of the stress-bearing and shape-maintaining murein sacculus of *Escherichia coli*. *Microbiol. Mol. Biol. Rev.*, 62(1):181–203, 1998.
- [76] Allison Hoynes-O’Connor and Tae Seok Moon. Programmable genetic circuits for pathway engineering. *Curr. Opin. Biotechnol.*, 36(Figure 1):115–121, 2015.
- [77] Kerwyn Casey Huang, Ranjan Mukhopadhyay, Bingni Wen, Zemer Gitai, and Ned S Wingreen. Cell shape and cell-wall organization in Gram-negative bacteria. *Proceedings of the National Academy of Sciences of the United States of America*, 105(49):19282–7, 2008.
- [78] N. Jain, K. V. Iyer, A. Kumar, and G. V. Shivashankar. Cell geometric constraints induce modular gene-expression patterns via redistribution of HDAC3 regulated by actomyosin contractility. *Proc. Natl. Acad. Sci.*, 110(28):11349–11354, 2013.
- [79] Seunghee S. Jang, Kevin T. Oishi, Robert G. Egbert, and Eric Klavins. Specification and simulation of synthetic multicelled behaviors. *ACS Synth. Biol.*, 1(8):365–374, 2012.
- [80] Michael C. Jewett and Tom Ellis. Editorial overview: Synthetic biology: Frontiers in synthetic biology. *Curr. Opin. Chem. Biol.*, 40:A1–A3, 2017.
- [81] Hongyuan Jiang, Fangwei Si, William Margolin, and Sean X. Sun. Mechanical control of bacterial cell shape. *Biophys. J.*, 101(2):327–335, 2011.

- [82] Hongyuan Jiang and Sean X. Sun. Morphology, growth, and size limit of bacterial cells. *Phys. Rev. Lett.*, 105(2), 2010.
- [83] Nathan I. Johns, Tomasz Blazejewski, Antonio L.C. Gomes, and Harris H. Wang. Principles for designing synthetic microbial communities. *Curr. Opin. Microbiol.*, 31:146–153, 2016.
- [84] Marion B Johnson, Alexander R March, and Leonardo Morsut. Engineering multicellular systems: Using synthetic biology to control tissue self-organization. *Curr. Opin. Biomed. Eng.*, 4:163–173, 2017.
- [85] J. Andrew Jones and Xin Wang. Use of bacterial co-cultures for the efficient production of chemicals. *Curr. Opin. Biotechnol.*, 53:33–38, 2018.
- [86] Yossef Kabessa, Ori Eyal, Ofer Bar-On, Victor Korouma, Sharon Yagur-Kroll, Shimshon Belkin, and Aharon J. Agranat. Standoff detection of explosives and buried landmines using fluorescent bacterial sensor cells. *Biosens. Bioelectron.*, 79:784–788, 2016.
- [87] Yossef Kabessa, Victor Korouma, Har’el Ilan, Sharon Yagur-Kroll, Shimshon Belkin, and Aharon J. Agranat. Simultaneous quantification of the fluorescent responses of an ensemble of bacterial sensors. *Biosens. Bioelectron.*, 49:394–398, 2013.
- [88] Chang Ho Kang, Yoon Jung Kwon, and Jae Seong So. Bioremediation of heavy metals by using bacterial mixtures. *Ecol. Eng.*, 89:64–69, 2016.
- [89] George G. Khachatourians. Agricultural use of antibiotics and the evolution and transfer of antibiotic-resistant bacteria. *Cmaj*, 159(9):1129–1136, 1998.
- [90] Harald König, Daniel Frank, Reinhard Heil, and Christopher Coenen. Synthetic biology’s multiple dimensions of benefits and risks: implications for governance and policies. In *Synth. Biol. Metaphor. Worldviews, Ethics, Law*, pages 217–232. Springer Fachmedien Wiesbaden, Wiesbaden, 2016.
- [91] Songzi Kou, Danhui Cheng, Fei Sun, and I-Ming Hsing. Microfluidics and microbial engineering. *Lab Chip*, 16(3):432–446, 2016.
- [92] Anastasia Krivoruchko and Jens Nielsen. Production of natural products through metabolic engineering of *Saccharomyces cerevisiae*. *Curr. Opin. Biotechnol.*, 35:7–15, 2015.

- [93] Laurent A. Lardon, Brian V. Merkey, Sónia Martins, Andreas Dötsch, Cristian Picioreanu, Jan Ulrich Kreft, and Barth F. Smets. iDynoMiCS: Next-generation individual-based modelling of biofilms. *Environ. Microbiol.*, 13(9):2416–2434, 2011.
- [94] Laurie J. Heyer and Jeffrey L. Poet. Synthetic Biology: A New Frontier. *Am. Math. Mon.*, 121(9):857, 2014.
- [95] Seth Lawson and Leonidas Bleris. Techniques and strategies employing engineered transcription factors. *Curr. Opin. Biomed. Eng.*, 4:152–162, 2017.
- [96] S E Lindow, N J Panopoulos, and B. L. Mcfarland. Genetic engineering of bacteria from managed and natural habitats. *Science (80-.)*, 244(4910):1300–1307, 1989.
- [97] Anders Logg, Kent-Andre Mardal, Garth N. Wells, et al. *Automated Solution of Differential Equations by the Finite Element Method*. Springer, 2012.
- [98] Anders Logg and Garth N. Wells. Dofin: Automated finite element computing. *ACM Transactions on Mathematical Software*, 37(2), 2010.
- [99] Anders Logg, Garth N. Wells, and Johan Hake. *DOLFIN: a C++/Python Finite Element Library*, chapter 10. Springer, 2012.
- [100] Kevin C. Ma, Samuel D. Perli, and Timothy K. Lu. Foundations and Emerging Paradigms for Computing in Living Cells. *J. Mol. Biol.*, 428(5):893–915, 2016.
- [101] Joseph S. Markson and Michael B. Elowitz. Synthetic biology of multicellular systems: New platforms and applications for animal cells and organisms. *ACS Synth. Biol.*, 3(12):875–876, 2014.
- [102] Ricardo Martínez-García, Carey D Nadell, Raimo Hartmann, Knut Drescher, and Juan A Bonachela. Cell adhesion and fluid flow jointly initiate genotype spatial distribution in biofilms. *PLOS Comput. Biol.*, 14(4):1–19, 2018.
- [103] Silvio Matassa, Nico Boon, Ilje Pikaar, and Willy Verstraete. Microbial protein: future sustainable food supply route with low environmental footprint. *Microb. Biotechnol.*, 9(5):568–575, 2016.
- [104] William Mather, Octavio Mondragon-Palomino, Tal Danino, Jeff Hasty, and Lev S. Tsimring. Streaming instability in growing cell populations. *Phys. Rev. Lett.*, 104(20), 2010.

- [105] Marco G. Mazza. The physics of biofilms - An introduction. *J. Phys. D. Appl. Phys.*, 49(20), 2016.
- [106] Adam L. Meadows, Kristy M. Hawkins, Yoseph Tsegaye, Eugene Antipov, Youngnyun Kim, Lauren Raetz, Robert H. Dahl, Anna Tai, Tina Mahatdejkul-Meadows, Lan Xu, Lishan Zhao, Madhukar S. Dasika, Abhishek Murarka, Jacob Lenihan, Diana Eng, Joshua S. Leng, Chi Li Liu, Jared W. Wenger, Hanxiao Jiang, Lily Chao, Patrick Westfall, Jefferson Lai, Savita Ganesan, Peter Jackson, Robert Mans, Darren Platt, Christopher D. Reeves, Poonam R. Saija, Gale Wichmann, Victor F. Holmes, Kirsten Benjamin, Paul W. Hill, Timothy S. Gardner, and Annie E. Tsong. Rewriting yeast central carbon metabolism for industrial isoprenoid production. *Nature*, 537(7622):694–697, 2016.
- [107] Amor A Menezes, John Cumbers, John A Hogan, and Adam P Arkin. Towards synthetic biological approaches to resource utilization on space missions. *J. R. Soc. Interface*, 12(102), 2015.
- [108] Mark Mimee, Phillip Nadeau, Alison Hayward, Sean Carim, Sarah Flanagan, Logan Jerger, Joy Collins, Shane McDonnell, Richard Swartwout, Robert J Citorik, Vladimir Bulović, Robert Langer, Giovanni Traverso, Anantha P Chandrakasan, and Timothy K Lu. An ingestible bacterial-electronic system to monitor gastrointestinal health. *Science (80-.)*, 360(6391):915–918, 2018.
- [109] Jean-Marie Mirebeau, Jérôme Fehrenbach, Laurent Risser, and Shaza Tobji. Anisotropic Diffusion in ITK. pages 1–9, 2015.
- [110] Charlie Y. Mo, Sara A. Manning, Manuela Roggiani, Matthew J. Culyba, Amanda N. Samuels, Paul D. Sniegowski, Mark Goulian, and Rahul M. Kohli. Systematically Altering Bacterial SOS Activity under Stress Reveals Therapeutic Strategies for Potentiating Antibiotics. *mSphere*, 1(4):e00163–16, 2016.
- [111] A. Mogilner, J. Allard, and R. Wollman. Cell Polarity: Quantitative Modeling as a Tool in Cell Biology. *Science (80-.)*, 336(6078):175–179, 2012.
- [112] Tae Seok Moon, Chunbo Lou, Alvin Tamsir, Brynne C. Stanton, and Christopher A. Voigt. Genetic programs constructed from layered logic gates in single cells. *Nature*, 491(7423):249–253, 2012.
- [113] Shankar Mukherji and Alexander Van Oudenaarden. Synthetic biology: Understanding biological design from synthetic circuits. *Nat. Rev. Genet.*, 10(12):859–871, 2009.

- [114] Carey D Nadell, Knut Drescher, and Kevin R Foster. Spatial structure, cooperation and competition in biofilms. *Nat. Rev. Microbiol.*, 14:589, 2016.
- [115] David R. Nielsen and Tae Seok Moon. From promise to practice. *EMBO Rep.*, 14(12):1034–1038, 2013.
- [116] Paolo G. P. Nucifora, Ragini Verma, Seung-Koo Lee, and Elias R. Melhem. Diffusion-Tensor MR Imaging and Tractography: Exploring Brain Microstructure and Connectivity. *Radiology*, 245(2):367–384, 2007.
- [117] Peter D. Olmsted and Paul M. Goldbart. Isotropic-nematic transition in shear flow: State selection, coexistence, phase transitions, and critical behavior. *Phys. Rev. A*, 46(8):4966–4993, 1992.
- [118] George A. O’Toole and Gerard C.L. Wong. Sensational biofilms: Surface sensing in bacteria. *Curr. Opin. Microbiol.*, 30(1999):139–146, 2016.
- [119] C. J. Paddon, P. J. Westfall, D. J. Pitera, K. Benjamin, K. Fisher, D. McPhee, M. D. Leavell, A. Tai, A. Main, D. Eng, D. R. Polichuk, K. H. Teoh, D. W. Reed, T. Treynor, J. Lenihan, H. Jiang, M. Fleck, S. Bajad, G. Dang, D. Dengrove, D. Diola, G. Dorin, K. W. Ellens, S. Fickes, J. Galazzo, S. P. Gaucher, T. Geistlinger, R. Henry, M. Hepp, T. Horning, T. Iqbal, L. Kizer, B. Lieu, D. Melis, N. Moss, R. Regentin, S. Secrest, H. Tsuruta, R. Vazquez, L. F. Westblade, L. Xu, M. Yu, Y. Zhang, L. Zhao, J. Lievens, P. S. Covelio, J. D. Keasling, K. K. Reiling, N. S. Renninger, and J. D. Newman. High-level semi-synthetic production of the potent antimalarial artemisinin. *Nature*, 496(7446):528–532, 2013.
- [120] Pamela P. Peralta-Yahya, Fuzhong Zhang, Stephen B. Del Cardayre, and Jay D. Keasling. Microbial engineering for the production of advanced bio-fuels. *Nature*, 488(7411):320–328, 2012.
- [121] Gert Peters, Pieter Coussement, Jo Maertens, Jeroen Lammertyn, and Marjan De Mey. Putting RNA to work: Translating RNA fundamentals into biotechnological engineering practice. *Biotechnol. Adv.*, 33(8):1829–1844, 2015.
- [122] Simone Pigolotti, Roberto Benzi, Mogens H. Jensen, Prasad Perlekar, and Federico Toschi. *Stochastic competition between two populations in space*, pages 105–117. Springer Vienna, Vienna, 2014.
- [123] Laurent Potvin-Trottier, Scott Luro, and Johan Paulsson. Microfluidics and single-cell microscopy to study stochastic processes in bacteria. *Curr. Opin. Microbiol.*, 43:186–192, 2018.

- [124] Oliver Purcell and Timothy K. Lu. Synthetic analog and digital circuits for cellular computation and memory. *Curr. Opin. Biotechnol.*, 29(1):146–155, 2014.
- [125] Sara Reardon. Visions of synthetic biology. *Science (80-.)*, 333(6047):1242–1243, 2011.
- [126] Sergi Regot, Javier MacIa, Nària Conde, Kentaro Furukawa, Jimmy Kjellén, Tom Peeters, Stefan Hohmann, Eulàlia De Nadal, Francesc Posas, and Ricard Solé. Distributed biological computation with multicellular engineered networks. *Nature*, 469(7329):207–211, 2011.
- [127] Margaret A Riley and John E Wertz. Bacteriocins: Evolution, Ecology, and Application. *Annu. Rev. Microbiol.*, 56(1):117–137, 2002.
- [128] Nicholas Roehner, Jacob Beal, Kevin Clancy, Bryan Bartley, Goksel Misirli, Raik Grünberg, Ernst Oberortner, Matthew Pocock, Michael Bissell, Curtis Madsen, Tramy Nguyen, Michael Zhang, Zhen Zhang, Zach Zundel, Douglas Densmore, John H. Gennari, Anil Wipat, Herbert M. Sauro, and Chris J. Myers. Sharing Structure and Function in Biological Design with SBOL 2.0. *ACS Synth. Biol.*, 5(6):498–506, 2016.
- [129] Sascha Rollié, Michael Mangold, and Kai Sundmacher. Designing biological systems: Systems Engineering meets Synthetic Biology. *Chem. Eng. Sci.*, 69(1):1–29, 2012.
- [130] Rachapun Rotrattanadumrong and Robert G. Endres. Emergence of cooperativity in a model biofilm. *J. Phys. D. Appl. Phys.*, 50(23), 2017.
- [131] Timothy J. Rudge, Fernán Federici, Paul J. Steiner, Anton Kan, and Jim Haseloff. Cell polarity-driven instability generates self-organized, fractal patterning of cell layers. *ACS Synth. Biol.*, 2(12):705–714, 2013.
- [132] Timothy J. Rudge, Paul J. Steiner, Andrew Phillips, and Jim Haseloff. Computational modeling of synthetic microbial biofilms. *ACS Synth. Biol.*, 1(8):345–352, 2012.
- [133] Zachary C. Ruhe, David A. Low, and Christopher S. Hayes. Bacterial contact-dependent growth inhibition. *Trends Microbiol.*, 21(5):230–237, 2013.
- [134] Luca Ruiu. Insect pathogenic bacteria in integrated pest management. *Insects*, 6(2):352–367, 2015.

- [135] Monirosadat Sadati, Nader Taheri Qazvini, Ramaswamy Krishnan, Chan Young Park, and Jeffrey J. Fredberg. Collective migration and cell jamming. *Differentiation*, 86(3):121–125, 2013.
- [136] Mehdi Sadeghpour, Alan Veliz-Cuba, Gábor Orosz, Krešimir Josić, and Matthew R. Bennett. Bistability and oscillations in co-repressive synthetic microbial consortia. *Quant. Biol.*, 5(1):55–66, 2017.
- [137] M Santillan. On the Use of the Hill Functions in Mathematical Models of Gene Regulatory Networks. *Math. Model. Nat. Phenom.*, 3(2):85–97, 2008.
- [138] David F. Savage, Jeffrey Way, and Pamela A. Silver. Defossilizing fuel: How synthetic biology can transform biofuel production. *ACS Chem. Biol.*, 3(1):13–16, 2008.
- [139] Markus Schmidt and Víctor De Lorenzo. Synthetic constructs in/for the environment: Managing the interplay between natural and engineered Biology. *FEBS Lett.*, 586(15):2199–2206, 2012.
- [140] Kara M. Schoenemann and William Margolin. Bacterial Division: FtsZ Treadmills to Build a Beautiful Wall. *Curr. Biol.*, 27(8):R301–R303, 2017.
- [141] Howard M. Shapiro. *Practical Flow Cytometry*. Wiley-Liss, 2003.
- [142] Boris I Shraiman. Mechanical feedback as a possible regulator of tissue growth. *Proc. Natl. Acad. Sci. U. S. A.*, 102(9):3318–3323, 2005.
- [143] Fangwei Si, Bo Li, William Margolin, and Sean X Sun. Bacterial growth and form under mechanical compression. *Sci. Rep.*, 5:11367, 2015.
- [144] Vijai Singh. Recent advancements in synthetic biology: Current status and challenges. *Gene*, 535(1):1–11, 2014.
- [145] A E Smith, Z Zhang, C R Thomas, K E Moxham, and a P Middelberg. The mechanical properties of *Saccharomyces cerevisiae*. *Proc. Natl. Acad. Sci. U. S. A.*, 97(18):9871–4, 2000.
- [146] William P J Smith, Yohan Davit, James M Osborne, Wook Kim, Kevin R Foster, and Joe M Pitt-Francis. Cell morphology drives spatial patterning in microbial communities. *Proc. Natl. Acad. Sci. U. S. A.*, 114(3):E280–E286, 2017.

- [147] Hao Song, Ming-Zhu Ding, Xiao-Qiang Jia, Qian Ma, and Ying-Jin Yuan. Synthetic microbial consortia: from systematic analysis to construction and applications. *Chem. Soc. Rev.*, 43(20):6954–6981, 2014.
- [148] Steven William Sowa, Grant Gelderman, and Lydia Maria Contreras. Advances in synthetic dynamic circuits design: Using novel synthetic parts to engineer new generations of gene oscillations. *Curr. Opin. Biotechnol.*, 36:161–167, 2015.
- [149] Eric J. Steen, Yisheng Kang, Gregory Bokinsky, Zhihao Hu, Andreas Schirmer, Amy McClure, Stephen B. Del Cardayre, and Jay D. Keasling. Microbial production of fatty-acid-derived fuels and chemicals from plant biomass. *Nature*, 463(7280):559–562, 2010.
- [150] Finn Stirling, Lisa Bitzan, Samuel O’Keefe, Elizabeth Redfield, John W.K. Oliver, Jeffrey Way, and Pamela A. Silver. Rational Design of Evolutionarily Stable Microbial Kill Switches. *Mol. Cell*, 68(4):686–696, 2017.
- [151] G. Strang. *Computational Science and Engineering*. Wellesley-Cambridge Press, 2007.
- [152] Sean X Sun and Hongyuan Jiang. Physics of bacterial morphogenesis. *Microbiol. Mol. Biol. Rev.*, 75(4):543–65, 2011.
- [153] B. Szabo. Phase transition in the collective migration of tissue cells: Experiment and model. *Phys. Rev. E - Stat. Nonlinear, Soft Matter Phys.*, 74(6):1–5, 2006.
- [154] Weixin Tang and David R. Liu. Rewritable multi-event analog recording in bacterial and mammalian cells. *Science (80-.)*, 360(6385), 2018.
- [155] Brian P. Teague, Patrick Guye, and Ron Weiss. Synthetic morphogenesis. *Cold Spring Harb. Perspect. Biol.*, 8(9):1–16, 2016.
- [156] Volker Ter Meulen. Time to settle the synthetic controversy. *Nature*, 509(7499):135, 2014.
- [157] Clara Torres-Barceló, Mila Kojadinovic, Richard Moxon, and R. Craig Maclean. The SOS response increases bacterial fitness, but not evolvability, under a sublethal dose of antibiotic. *Proc. R. Soc. B Biol. Sci.*, 282(1816):0–7, 2015.
- [158] Melanie Tramontano, Sergej Andrejev, Mihaela Pruteanu, Martina Klünemann, Michael Kuhn, Marco Galardini, Paula Jouhten, Aleksej Zelezniak, Georg Zeller, Peer Bork, Athanasios Typas, and Kiran Raosaheb Patil.

- Nutritional preferences of human gut bacteria reveal their metabolic idiosyncrasies. *Nat. Microbiol.*, 3(4):514–522, 2018.
- [159] Xavier Trepat, Michael R. Wasserman, Thomas E. Angelini, Emil Millet, David A. Weitz, James P. Butler, and Jeffrey J. Fredberg. Physical forces during collective cell migration. *Nat. Phys.*, 5(6):426–430, 2009.
- [160] Ryan Tsoi, Feilun Wu, Carolyn Zhang, Sharon Bewick, David Karig, and Lingchong You. Metabolic division of labor in microbial systems. *Proc. Natl. Acad. Sci.*, 115(10):201716888, 2018.
- [161] Hannah H. Tuson, George K. Auer, Lars D. Renner, Mariko Hasebe, Carolina Tropini, Max Salick, Wendy C. Crone, Ajay Gopinathan, Kerwyn Casey Huang, and Douglas B. Weibel. Measuring the stiffness of bacterial cells from growth rates in hydrogels of tunable elasticity. *Mol. Microbiol.*, 84(5):874–891, 2012.
- [162] Arturo Urrios, Javier Macia, Romilde Manzoni, Núria Conde, Adriano Bonforti, Eulàlia De Nadal, Francesc Posas, and Ricard Solé. A Synthetic Multicellular Memory Device. *ACS Synth. Biol.*, 5(8):862–873, 2016.
- [163] Erick J. Vandamme. Production of vitamins, coenzymes and related biochemicals by biotechnological processes. *J. Chem. Technol. Biotechnol.*, 53(4):313–327, 1992.
- [164] Alan Veliz-Cuba, Andrew J. Hirning, Adam A. Atanas, Faiza Hussain, Flavia Vancia, Krešimir Josić, and Matthew R. Bennett. Sources of Variability in a Synthetic Gene Oscillator. *PLoS Comput. Biol.*, 11(12):1–24, 2015.
- [165] Dmitri Volfson, Scott Cookson, Jeff Hasty, and Lev S Tsimring. Biomechanical ordering of dense cell populations. *Proc. Natl. Acad. Sci. U. S. A.*, 105(40):15346–15351, 2008.
- [166] Baojun Wang and Martin Buck. Customizing cell signaling using engineered genetic logic circuits. *Trends Microbiol.*, 20(8):376–384, 2012.
- [167] Ping Wang, Lydia Robert, James Pelletier, Wei Lien Dang, Francois Taddei, Andrew Wright, and Suckjoon Jun. Robust growth of escherichia coli. *Curr. Biol.*, 20(12):1099–1103, 2010.
- [168] Zhaoshou Wang, Xin Wu, Jianghai Peng, Yidan Hu, Baishan Fang, and Shiyang Huang. Artificially constructed quorum-sensing circuits are used for subtle control of bacterial population density. *PLoS One*, 9(8):1–7, 2014.

- [169] Wilfried Weber and Martin Fussenegger. The impact of synthetic biology on drug discovery. *Drug Discov. Today*, 14(19-20):956–963, 2009.
- [170] Sandra Wegner, Tamás Börzsönyi, Tomasz Bien, Georg Rose, and Ralf Stanarijus. Alignment and dynamics of elongated cylinders under shear. *Soft Matter*, 8(42):10950, 2012.
- [171] James J. Winkle, Oleg A. Igoshin, Matthew R. Bennett, Krešimir Josić, and William Ott. Modeling mechanical interactions in growing populations of rod-shaped bacteria. *Phys. Biol.*, 14(5), 2017.
- [172] EH Edwin H Wintermute and Pamela A Silver. Dynamics in the mixed microbial concourse. *Genes & Dev.*, 24(23):2603–2614, 2010.
- [173] S. Woloszynek, S. Pastor, J. C. Mell, N. Nandi, B. Sokhansanj, and G. L. Rosen. *Engineering Human Microbiota: Influencing Cellular and Community Dynamics for Therapeutic Applications*, volume 324. Elsevier Inc., 2016.
- [174] Fuqing Wu and Xiao Wang. Applications of synthetic gene networks. *Sci. Prog.*, 98(3):244–252, 2015.
- [175] Marco Zaccaria, Sandra Dedrick, and Babak Momeni. Modeling Microbial Communities: A Call for Collaboration between Experimentalists and Theorists. *Processes*, 5(4):53, 2017.
- [176] Amin Zargar, Gregory F. Payne, and William E. Bentley. A 'bioproduction breadboard': Programming, assembling, and actuating cellular networks. *Curr. Opin. Biotechnol.*, 36:154–160, 2015.
- [177] Yuting Zheng and Ganesh Sriram. Mathematical modeling: Bridging the gap between concept and realization in synthetic biology. *J. Biomed. Biotechnol.*, (Article ID 541609, 16 pages, 2010. <https://doi.org/10.1155/2010/541609>).